*Dedicated to my Beloved Family*

# CERTIFICATE

It is certified that the work contained in the thesis titled ***"STRUCTURE, MAGNETIC, OPTICAL AND ELECTRICAL PROPERTIES OF MULTIFUNCTIONAL NANOSTRUCTURED Dy AND/OR Sm DOPED $HfO_2$"*** by ***"SANDEEP KUMAR"*** has been carried out under my supervision and that this work has not been submitted elsewhere for a degree.

It is further certified that the student has fulfilled all the requirements of Comprehensive, Candidacy and SOTA for the award of Ph.D. degree.

Date:

Place: Varanasi

**Dr. (Mrs.) Chandana Rath**
**(Supervisor)**

# DECLARATION BY THE CANDIDATE

I, ***SANDEEP KUMAR***, certify that the work embodied in this Ph.D. thesis is my own bonafide work carried out by me under the supervision of **Dr. (Mrs.) CHANDANA RATH** for a period from **July 2014** to **June 2019** at the **SCHOOL OF MATERIALS SCIENCE AND TECHNOLOGY**, Indian Institute of Technology (Banaras Hindu University), Varanasi, India. The matter embodied in this Ph.D. thesis has not been submitted for the award of any other degree/diploma. I declare that I have faithfully acknowledged and given credits to the research workers wherever their works have been cited in my work in this thesis. I further declare that I have not willfully copied any other's work, paragraphs, text, data, results, *etc*., reported in journals, books, magazines, reports dissertations, thesis, *etc*., or available at websites and have not included them in this thesis and have not cited as my own work.

Date……

Place: Varanasi (Sandeep Kumar)

---

# CERTIFICATE BY THE SUPERVISOR

This is to certify that the above statement made by the candidate is correct to the best of my knowledge.

**Dr. (Mrs.) Chandana Rath**
**Supervisor** **Coordinator**

# COPYRIGHT TRANSFER CERTIFICATE

**Title of the Thesis: "Structure, Magnetic, Optical and Electrical Properties of Multifunctional Nanostructured Dy and/or Sm Doped $HfO_2$"**

**Candidate's Name:** Mr. Sandeep Kumar

## Copyright Transfer

The undersigned hereby assigns to the Indian Institute of Technology (Banaras Hindu University), Varanasi all rights under copyright that may exist in and for the above thesis submitted for the award of the *Doctor of Philosophy*.

Date:

Place: Varanasi (Sandeep Kumar)

**Note: However, the author may reproduce or authorize others to reproduce materials extracted verbatim from the thesis or derivative of the thesis for author's personal use provided that the source and the Institute's copyright notice is indicated.**

# *Acknowledgements*

*At this moment of retrospection, it gives me immense pleasure to acknowledge the persons who have directly or indirectly helped me during the course of my work and stay at IIT (BHU). To express my heartfelt gratitude is not only my moral duty but I consider it an act of pleasure and humility as well.*

*First and Foremost, I wish to express my sincere gratitude to my supervisor,* ***Dr. (Mrs.) Chandana Rath,*** *for her trust, nice guidance, faithful support and valuable suggestions throughout my Ph.D. work. Her constant monitoring and interest in my work will always remain as a happy memory. Her patient and enthusiastic approach for my training cannot be expressed in words and I will always remain thankful to her.*

*I would also like to express my sincere thanks to RPEC members Dr. Akhilesh Kumar Singh, School of Materials Science & Technology, IIT (BHU) and Dr. Shail Upadhyay, Department of Physics, IIT (BHU), for their stimulating help and criticism which incented me to widen my research from various perspectives. I would like to thank coordinator of School of Materials Science and Technology, IIT (BHU) for providing different instrumental facility. I would like to convey my gratitude to Dr. A. K. Mishra (DPGC convener) for his valuable inputs, suggestions and affectionate attitude.*

*I wish to express deep regards to all the teachers of the School Prof. D. Pandey, Prof. R. Prakash, Prof. P. Maiti, Dr. B. N. Pal, Dr. C. Upadhyay, Dr. Sanjay Singh, Dr. S. K. Mishra, Dr. S. R. Singh, Prof. Jitendra Kumar, Dr. Ashish Singh and others for their kind support at all moment during the progress of my research.*

*With a deep sense of gratitude, I convey my sincere thanks to CIFC, IIT (BHU), Varanasi for help in carrying out characterizations of the synthesized samples. I am also grateful to all office staff of the School and authorities of IIT (BHU), for their kind help during the period of my stay to complete the thesis work.*

*With a special thanks to my labmates Dr. Himanshu Tripathy, Mr. Gaurav Chandra Pandey, Ms. Deepti Gangwar, Mr. Manish Yadav, Mr. Abhay Narayan Singh and Mr. Tarang Dehury, I am grateful to my seniors Dr. Vinay Pratap Singh, Dr. Pankaj Mohanty, Dr. Durgesh Kumar, Dr. Jagdish Kumar G, Mr. Pramod Kumar Yadav, Dr. Arpan Biswas, Mr. Chandrabhal Singh and Mr. Dinesh Kumar for their valuable advice. I am extremely thankful to my dear friends as well as colleagues Mr. Anand Sharma, Mr. Satya Veer Singh, Ms. Aparna Shukla, Ms. Priyanka Tiwari, Mrs. B Bharati and juniors Mr. Nitesh K. Chourasia and Mr. Viswas Acharya for their unconditional cooperation and sincere help in every possible way as well as for making my stay here enjoyable and their time to time encouragement during my bad situations.*

*It fills me with a deep sense of reverence when I think of my family. Their constant encouragement, moral support and cooperation at every step of my life cannot be expressed in words. I am extremely thankful for their love and blessings.*

*Finally, I bow with reverence and gratitude to thank the Almighty Lord KASHI VISHWANATH and Goddess DURGA who have enriched me with such an excellent opportunity and infused the power in my mind to fulfill the work assigned to me.*

Date:

Place: Varanasi (Sandeep Kumar)

# *Contents*

# *List of Figures*

# *List of Tables*

# *Abbreviations*

| | |
|---|---|
| TMO | Transition metal oxides |
| *k* | Dielectric constant |
| MIM | Metal-insulator-metal |
| XRD | X-ray diffraction |
| GIXRD | Grazing incidence X-ray diffraction |
| AFM | Atomic force microscope |
| SEM | Scanning electron microscope |
| PL | Photoluminescence |
| RRAM | Resistive random access memory |
| I-V | Current voltage |
| $p^{++}$-Si | Heavily doped p-type silicon |
| EG | Ethylene glycol |
| *d* | Interplanar spacing |
| B. E. | Binding energy |
| CIFC | Central instrument facility center |
| EBE | Electron beam evaporation |
| kHz | Kilo Hertz |
| H | Magnetic field |
| K | Kelvin |
| K. E. | Kinetic energy |
| kV | Kilo volt |
| keV | Kilo electron volt |
| M | Magnetization/Mol |

| | |
|---|---|
| mA | Milli ampere |
| MPMS | Magnetic property measurement systems |
| MT | Magnetization versus temperature |
| MH | Magnetization versus field |
| $M_s$ | Saturation magnetization |
| PMT | Photomultiplier tube |
| RE | Rare earth |
| RT | Room temperature |
| RTFM | Room temperature ferromagnetism |
| SAED | Selected area electron diffraction |
| SEM | Scanning electron microscopy |
| HRSEM | High resolution scanning electron microscopy |
| T | Temperature |
| TEM | Transmission electron microscopy |
| HRTEM | High resolution transmission electron microscopy |
| XPS | X-ray photo electron spectroscopy |
| ZFC | Zero field cooling |
| eV | Electron volt |
| kOe | Kilo Oersted |
| at % | Atomic percentage |
| nm | Nanometer |
| mg | Milligram |
| λ | Wavelength |

| | |
|---|---|
| CMOS | Complementary metal oxide semiconductor |
| Å | Angstrom |
| P | Pressure |
| GPa | Giga Pascal |
| $^{o}C$ | Degree Centigrade |
| $V_o$ | Oxygen vacancy |
| $V_o^+$ | Singly charged oxygen vacancy |
| $V_o^{++}$ | Doubly charged oxygen vacancy |
| $V_M$ | Metal cation vacancy |
| O*i* | Oxygen interstitial |
| UV | Ultra violet |
| ET | Energy transfer |
| CTB | Charge transfer band |
| LFPs | Latent fingerprints |
| CFs | Conducting filaments |
| HRS | High resistance state |
| LRS | Low resistance state |
| PL | Photoluminescence |
| ms | Millisecond |
| θ | Bragg angle |
| $M_{max}$ | Maximum magnetization |
| χ | Susceptibility |
| CIE | Commission Internationale de I'Eclairage |

# *PREFACE*

Hafnium oxide ($HfO_2$) has been consistently researched as a prospective material mainly as an alternate to silicon for semiconductor industry. Because of its appropriate high-*k* value and the high thermal stability against silicon, $HfO_2$ is proven as a potential candidate for gate dielectric material in metal oxide field effect transistors (MOSFETs). In the year 2007, $HfO_2$ is being used as the gate dielectric in Intel's 45 nm quad core processor replacing $SiO_2$. Additionally, $HfO_2$ finds promising applications in anti-reflection coatings, X-ray phosphors, cellular imaging, ferroelectric and resistive random access memories (FeRAM and RRAM) and so on. Bulk $HfO_2$ crystallizes in monoclinic phase at room temperature which transforms to the tetragonal and cubic phase at 1700 and 2600 $^oC$, respectively. According to the reported literatures, the technologically relevant high temperature tetragonal and cubic phase of $HfO_2$ exhibit the high dielectric constant, *k*, ~70 and 25, respectively. First principle calculation suggests that the high temperature tetragonal and cubic phase of $HfO_2$ can be stabilized at room temperature by an appropriate dopant of lower valency. In this context, a few authors discuss the diverse effect of trivalent element doping having different ionic radii than Hf on the stability of tetragonal and cubic phase of $HfO_2$. It has been established that while the undersized dopants such as Si, Ge, Sn, P, Al or Ti stabilize the tetragonal phase, the dopants with oversize ionic radii like Y, Gd or Sc than Hf favour the stabilization of the cubic phase at room temperature.

Besides, the stabilization of the high temperature cubic phase of $HfO_2$, it is shown to possess rich magnetic and optical properties when size is reduced to nanometer range. Being $HfO_2$ a non-magnetic transition metal oxide with $d^0$ cations, the recent discovery of unusual room temperature ferromagnetism (RTFM) in $HfO_2$ thin film is fascinating and

compelling for materials research communities. A wide group of researchers believes that required defects such as oxygen vacancies ($V_o$) can be held responsible for such type of ferromagnetic ordering present in diamagnetic oxides at room temperature. In this regard, Coey *et al.* report observation of RTFM in the monoclinic $HfO_2$ thin films originating due to unpaired electrons in extended molecular orbital of the defects. N. H. Hong reports RTFM with a large magnetic moment in $HfO_2$ thin films. Apart from RTFM observed in thin films, ferromagnetic behavior has also been observed in $HfO_2$ nanoparticles, nanoclusters and nanorods synthesized via various chemical routes at room temperature. Liu *et al.* have shown this behavior in nanorods and Dohčević-Mitrović *et al.* report the same in nanopowders. Besides, RTFM has also been demonstrated in yttrium (Y) and nickel (Ni) doped $HfO_2$ nanoparticles. Further, $HfO_2$ has been emerged as an outstanding host showing excellent photoluminescence properties. As a host, $HfO_2$ shows remarkable photoluminescence properties originating due to defect centers created within the band gap of $HfO_2$. It is known that Hf and O vacancies are most likely to be produced during the synthesis of $HfO_2$ and heat treatments. The different uncharged and charged oxygen vacancies by electron trap such as $V_o$, $V_o^+$ and $V_o^{++}$ etc exist in $HfO_2$ lattice which act as the luminescence centers. In this regard, most recently, Villa *et al.* show that the luminescence in $HfO_2$ nanocrystals is modified tremendously by annealing at different temperatures. Upon incorporation of a rare earth ion in the host $HfO_2$, the host can also sensitize the luminescence of activator ion and improves the optical performance. Due to wide band gap, ~5.9 eV of $HfO_2$, it provides a better compliance for the most of RE ions including Eu, Nb and Tb etc producing excellent emissions in visible region. Wiatrowska *et al*. demonstrate modeling of photoluminescence behavior of Eu doped $HfO_2$ by codoping

Li, Ta, Nb and V used as charge compensating ions for $Eu^{3+}$ substituted at $Hf^{4+}$ in lattice. Only $HfO_2$:Eu,Nb powders reveal an enhanced and intense photoluminescence properties. Lauria *et al.* have established that the photoluminescence properties of $HfO_2$:Eu/Tb nanoparticles are drastically modified depending on the monoclinic and cubic phase stabilized by a nonradiative $Lu^{3+}$ ion. Such potential luminescent materials are also actively used in latent fingerprint imaging in forensic sciences. The development of latent fingerprints (LFPs) detected at the site of crime is considered as an imperative physical evidence in forensic investigations. In this regard, Wang *et al*. have shown that luminescent $YVO_4$:Eu red-emitting nanocrystals of ~40 nm and $LaPO_4$:Ce,Tb green-emitting nanobelts with an average diameter of ~19 nm and length ~340 nm develop LFPs with exceptional contrast and selectivity having very less background intervention under 254 nm UV irradiation. However, use of deep UV radiations for LFPs development ultimately increase the overall processing cost. Therefore, one needs to develop luminescent nanosized powders excitable at higher wavelengths which is certainly advantageous for developing LFPs at relatively cheaper processing cost.

Along with the rich physical properties, $HfO_2$ has also been attracted significant attention for RRAM application in next generation data storage devices. RRAM nonvolatile memory devices store and read information by switching between a low and high resistive states under an applied bias voltage. In this regard, the stable, uniform and reproducible bipolar resistive switching in $HfO_2$ based RRAM device has been reported by Jančovič *et al*. and Hua *et al*. Looking at the rich evolution of structure with temperature in $HfO_2$, our objective is to stabilize the high temperature tetragonal or cubic phase at room temperature by either reducing dimension and/or incorporating rare earth (RE) dopants.

Not only structure, rare earth dopants in $HfO_2$ nanoparticles demonstrate excellent optical properties which can be potentially explored for latent fingerprint imaging useful in forensic investigations. The robustness of luminescent RE doped $HfO_2$ can also be perceived for various optoelectronic device applications. Further, we also intend to stabilize the cubic phase in rare earth doped $HfO_2$ thin films along with systematic investigation on the electrical properties important for RRAM memory applications. The effect of different synthesis conditions such as temperature, oxygen partial pressure, film thickness, top electrode material and dopant on the resistive switching behavior of $HfO_2$ is to be studied. Our thorough investigations on multifunctional nanostructured rare earth doped $HfO_2$ reveal several key findings which have not been reported earlier.

In this context, we unveil that high temperature cubic phase which is observed at 2600 $^{o}$C, can be stabilized at room temperature after doping optimum concentration of Dy or Sm. In contrast to diamagnetic behavior in bulk, $HfO_2$ nanoparticles show unusual ferromagnetism at room temperature. Further, 1 at% of Dy or Sm doped $HfO_2$ demonstrates excellent emissions in visible region producing cool white light.

Further, we introduce the concept of stabilizing the cubic phase of $HfO_2$ even after codoping Dy and Sm with an optimum concentration. Dy and Sm codoped $HfO_2$ shows prominent emission peaks in blue, yellow and near red spectral regions producing purplish colored light. Owing to outstanding luminescence properties of RE doped $HfO_2$ nanophosphors, for the first time, we examine their perspective as dusting powder for LFPs imaging. LFPs developed onto several surfaces exhibit third-level details, good background contrast, selectivity and acceptable resolution.

Not only in RE doped $HfO_2$ nanoparticles, but also we demonstrate that the cubic phase is even stabilized at room temperature in thin films after doping with half of the Sm or Dy concentration. These films exhibit the bipolar switching behavior which is of forming-free nature distinctive to RRAM device.

***List of journals and books used to bind up the thesis has been given at the end as references.***

# Chapter 1

Nanostructured binary transition metal oxides (TMOs) are technologically important class of smart materials that possess high interest because of their great chemical stability, simple structure and low cost production. These functional materials are considered as the building block of next generation advance electronic devices. There exists a widespread attraction for TMOs within industries due to their several technological applications primarily useful for resolving issues related to cutting edge research. It is well-known that in TMOs, electrons occupy the *s*-shells of metal cations whereas *d*-shells are partially filled containing unpaired electrons which essentially evoke intriguing physical and chemical properties. In contrast to bulk, nanostructured TMOs are capable of offering superior structural, optical, magnetic, electronic and electrical properties.[1-4] Different TMOs like $TiO_2$, $VO_2$, $MnO_2$, $Fe_2O_3$, NiO, ZnO,$WO_3$, $ZrO_2$ and $HfO_2$ having diverse morphology and dimension are now being explored for their implementation in a range of industrial fields. A consistent research and development of TMOs has laid down promising applications in water desalination/purification, transparent semiconductor devices, spintronics, gas sensing, scintillation, UV detectors, photocatalysis, optoelectronics, energy storage, memory devices, fuel cells, optical coatings, insulation and abrasive materials etc. Apart from aforementioned potential applications, non-hazardous lead-free TMOs have also been investigated for biological applications as antibacterial agents including for biosensing, biotransportation, radiosensitisation, drug discovery and delivery etc. [2, 5-10]

In general, nanostructured materials are classified as the structures with variable dimensions between 1-100 nm. Depending on the shape and size, nanostructures are categorized into following:

- 0D (Zero dimensional) e.g. nanoparticles and nanodots
- 1D (One dimensional) e.g. nanotube and nanowires
- 2D (Two dimensional) e.g. nanosheets
- 3D (Three dimensional) e.g. nanocubes

When the size is reduced to nanometer range, most of the physical and chemical properties are modified constructively.[11, 12] A direct consequence of size reduction is evidenced in case of $Fe_2O_3$ nanoparticles. It is well-known that $Fe_2O_3$ shows antiferromagnetic ordering which transforms to superparamagnetic behavior if the nanoparticles attain a certain size of ~3 nm.[6, 13-15] In particular, the reduced particle size having very large surface to volume ratio results into unusual properties of TMOs. A variety of TMOs nanostructures including specific exposed facet and hierarchical structures such as nanotubes, nanoplates, nanobelts, nanoforests, nanorod arrays, nanobrush and tube-in-tube nanostructures can be achieved by employing different synthesis techniques like hydrothermal, solvothermal, sol-gel, liquid phase, vapor phase methods, thermal decomposition and so on. Interestingly, the different morphology of these nanostructured TMOs is easily obtained by controlling and tuning various synthesis parameters e.g. temperature, pressure, reactive and inert gas flow environment, solvent and surfactant etc.[16-26]

Another example of TMOs nanostructuring includes the size effect in modifying the structural properties of $TiO_2$ nanoparticles. $TiO_2$ exhibits three different crystal structures such as the anatase, rutile and brookite phase. Many researchers have systematically

studied the phase transformation in nanocrystalline $TiO_2$ and establish that the anatase phase becomes relatively more stable than that of rutile one once the particle size is reduced below ~14 nm. Above this critical particle size, the rutile phase of $TiO_2$ can be reversibly stabilized under ambient conditions.[27-30] Thus, the direct nanoarchitecturing of TMOs can facilitate better control of structure, optical, magnetic, electrical and other physical along with chemical properties.

Among all TMOs, Hafnium oxide ($HfO_2$) is of special scientific interest due to its excellent thermodynamic stability and ability to cope with existing hurdles within silicon based industry.[31] $HfO_2$ is an electrical insulator having a wide bandgap of ~5.7 eV and appropriate dielectric constant (*k*) value which has been successfully utilized to serve effectual solutions of the major issues in present complementary metal oxide semiconductor (CMOS) technology.[3, 32] In CMOS, the prominent concern of higher leakage current due to direct tunneling of electrons arises with down scaling of gate dielectric thickness below ~3 nm. In order to resolve this issue, a new type of material so called "high-*k* material" like $HfO_2$ is sought after to achieve CMOS devices with high performance.[33, 34] Recently, in the year 2007, $HfO_2$ is being used into Intel's 45 nm technology replacing conventional $SiO_2$ which reduced the leakage current density by an order of magnitude. This mitigated the heat dissipation issue in 45 nm technology node to a great extent.[35] Apart from its high-*k* value, $HfO_2$ possesses intriguing physical properties e.g. high density of ~9.8 g/cm$^3$, very high melting point of 2600 $^oC$ and refractive index of ~2 rendering promising applications in optical coating, anti-reflective coating, refractory, X-ray phosphors, spintronics and non-volatile memory including resistance random access memory (RRAM) and ferroelectric, FeRAM devices etc (**figure 1.1**).[36-41]

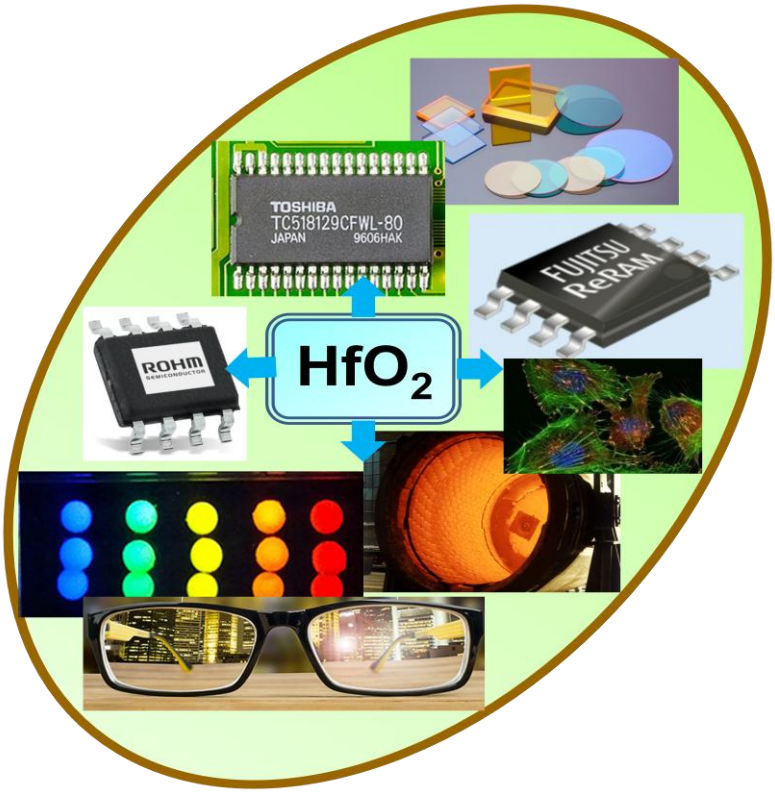


***Figure 1.1*** *Examples of potential applications of $HfO_2$ in various industries.*

## 1.1 Structure of $HfO_2$

$HfO_2$ is commonly referred as hafnia. Prior to the deployment of $HfO_2$ as a prospective electronic material in CMOS industry, its conventional use was primarily focused as a refractory ceramic material in reactors and thermocouple devices owing to its high melting temperature. It is known that $HfO_2$ is very much similar to $ZrO_2$ with almost identical physical and chemical properties. Since the discovery of transformation toughening in crystalline $ZrO_2$, a wide group of researchers has devoted systematic and consistent research to understand the crystallographic properties of crystalline $HfO_2$. The crystallography of $HfO_2$ shows significant impact on its different physical properties such as structural, electronic, magnetic, optical and so on.

### 1.1.1 Phases of $HfO_2$ at Ambient Pressure

In bulk, $HfO_2$ possesses polymorphism such as monoclinic (*m*), $P2_1/c$, tetragonal (*t*), $P4_2/nmc$ and cubic (*c*), $Fm\bar{3}m$ phases. These three different structures of $HfO_2$ can exist at various temperature under normal pressure shown in **figure 1.2**. In contrast to chemically similar system, $ZrO_2$, the phase transformation among three phases of $HfO_2$ usually occurs at relatively higher temperature. According to thermodynamic studies of $ZrO_2$ and $HfO_2$, the phase transformation from monoclinic to tetragonal and eventually to cubic one is highly dependent on internal energy and entropy.[42] Therefore, the Gibbs free energy ($\Delta G = \Delta U + p\Delta V - T\Delta S$) related to such phase transformation in $HfO_2$ is very crucial for a clear understanding of its different crystalline phases. $\Delta G$, $\Delta U$, $\Delta V$, $\Delta S$ is change in Gibbs free energy, internal energy, volume and entropy, respectively whereas $p$ is pressure and $T$ is the phase transformation temperature. The high temperature tetragonal and cubic phases of $HfO_2$ exhibit high symmetry which are more stable as per the entropy is concerned. Under minimum energy condition, $\Delta G$ must be zero at phase transition point i.e. $\Delta G = \Delta U + p\Delta V - T\Delta S = 0$. The first order phase transitions are referred to discontinuity in first derivatives of $G$ which are entropy and volume. However, second order transitions have continuous first derivatives indicating no change in $S$ or $V$.

Discontinuous first derivatives of $G\ (T, p)$: $(\delta G/\delta T)p = S,\ (\delta G/\delta p)T = V$

In bulk $HfO_2$, the monoclinic phase remains stable at room temperature and transforms to tetragonal phase at ~2052 K which ultimately undergoes phase transition to cubic one at 2803 K.[43] The temperature of phase transformation in $HfO_2$ depends on several factors such as particle size, impurities, stress and so on. In monoclinic phase of $HfO_2$, the coordination number of $Hf^{4+}$ is 7, whereas it increases to 8 in the high

temperature tetragonal or cubic phase.[44] According to the thermodynamic equations discussed above, the monoclinic ↔ tetragonal phase transformation is of first order due to substantial modification of the local bonding within structural configuration. Such phase transformation also reduces the lattice volume notably producing large strain in the crystal. On the other hand, a second order phase transition governs the tetragonal to cubic phase transformation since no significant change in volume is evidenced.[45]

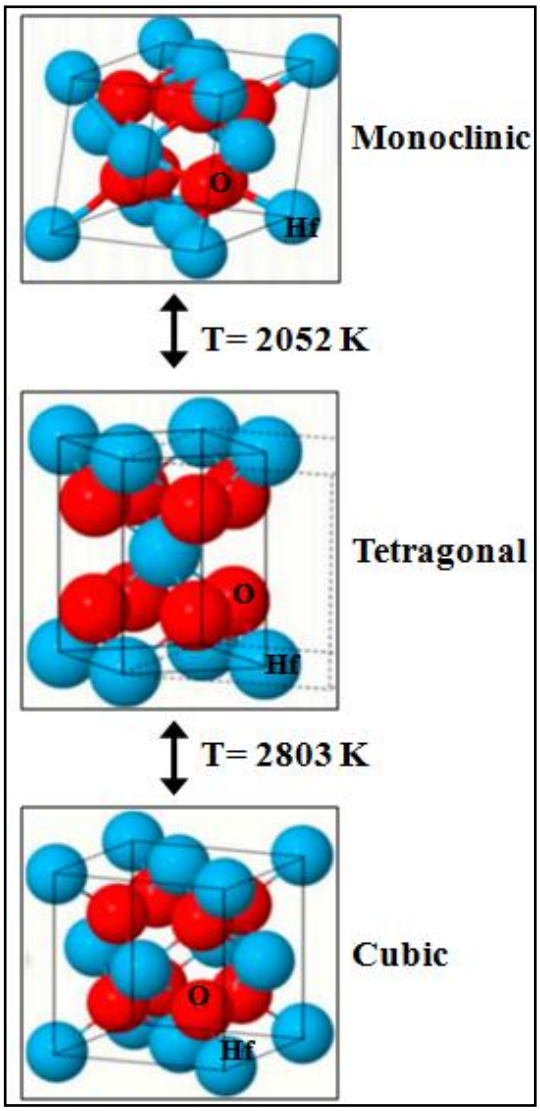


***Figure 1.2*** *Different phases of $HfO_2$ as a function of temperature under normal pressure condition.*

### 1.1.2 High Pressure Driven Phases of $HfO_2$

Apart from the phase transformation with increasing temperature, the crystalline monoclinic phase of $HfO_2$ becomes relatively unstable under an applied external pressure. Following the temperature-pressure (*T-P*) phase diagram depicted in **figure 1.3**, $HfO_2$ supposes to adopt an orthorhombic symmetry revealing two distinct polymorphs known as OrthoI (OI) and OrthoII (OII). High pressure induced OI and OII phases in $HfO_2$ are stable from 4 to 25 GPa and almost independent of temperature up to 1400 $^{o}$C.[46] Based on the neutron diffraction study, it is established that OI stabilizes with space group, *Pbca* whereas OII acquires an orthorhombic cotunnite ($PbCl_2$)-type structure having space group, *Pmnb*.

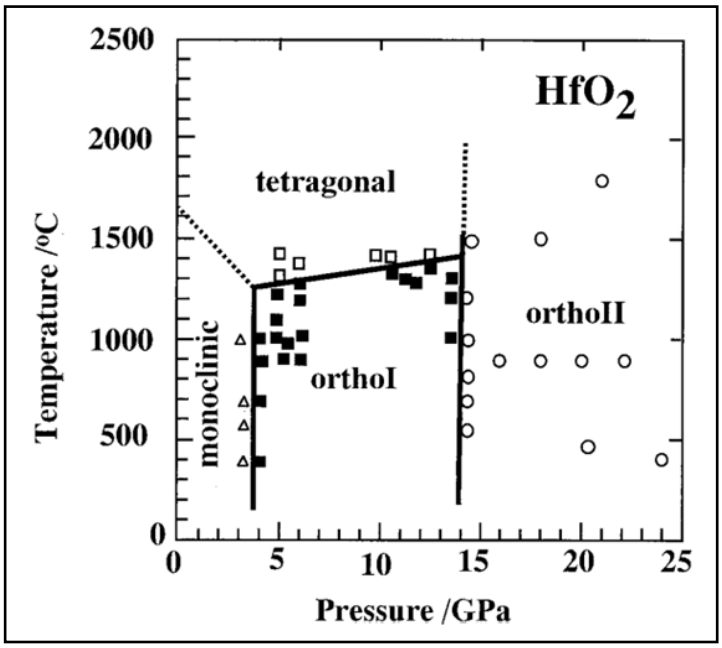


***Figure 1.3*** *Temperature-Pressure (T-P) phase diagram of $HfO_2$. (adapted from [46])*

$Hf^{4+}$ ions form 7 and 9-fold coordination with oxygen in OI and OII phase, respectively.[47, 48] A reduction in volume is observed when the monoclinic phase of

$HfO_2$ transforms to OI phase. The pressure at which OI-to-OII phase transition occurs is not related to the thermodynamic equilibrium conditions due to reconstructive nature of this transition. According to first principle calculation and appropriate experiments, the high pressure OII phase of $HfO_2$ is considered for ultrahard materials because of its excellent bulk modulus property.

### 1.1.3 Stabilization of the High Temperature Tetragonal/Cubic Phase of $HfO_2$ at Room Temperature

In general, the phase stabilization in TMOs is understood in terms of the stability of a specific crystalline phase at ambient conditions which is usually observed at high temperature and pressure. Under normal temperature and pressure, the stability of specific phase in TMOs is achieved by alloying appropriate dopant or optimizing synthesis parameters such as temperature, grain size, solvent and oxygen partial pressure etc. There is an utmost requirement of a suitable method to achieve the high temperature tetragonal or cubic phase of $HfO_2$ at RT or moderate temperature that possesses distinct physical properties which are not exclusively realized in the monoclinic one. As far as the CMOS device applications are concerned, an amorphous phase of $HfO_2$ is used up to the growth temperature of ~300 $^{o}$C which does not exhibit any superior physical properties compared to the crystalline, monoclinic phase. First principle calculation predicts that the high temperature tetragonal or cubic phase of $HfO_2$ are technologically more important than that of the monoclinic one. While the monoclinic phase possesses a low *k* value of ~15, $HfO_2$, in its tetragonal or cubic phase shows the higher *k* value above ~30.[49] It is therefore more advantageous to employ $HfO_2$ crystallized in the high symmetrical phases of tetragonal or cubic for developing future CMOS with improved device performance and reliability.

### 1.1.3.1 Effect of Synthesis Conditions

The technologically relevant cubic phase of $HfO_2$ has been shown to be stabilized at room temperature without any dopant. The metastable cubic phase can be obtained in $HfO_2$ films annealed at 500 $^oC$ in vacuum. The allotropic modification from amorphous to cubic phase is varied between 30-1500 $^oC$. The cubic phase remains stable upto 600 $^oC$ and partially transforms to the monoclinic one with increasing temperature upto 1400 $^oC$. Such phase transformation becomes more prominent when $HfO_2$ films are annealed in air.[44] Sharath *et al*. demonstrate that the other high temperature tetragonal phase can be achieved in $HfO_2$ film deposited onto $TiN/SiO_2/Si(001)$ at substrate temperature of 320 $^oC$ depicted in **figure 1.4**.

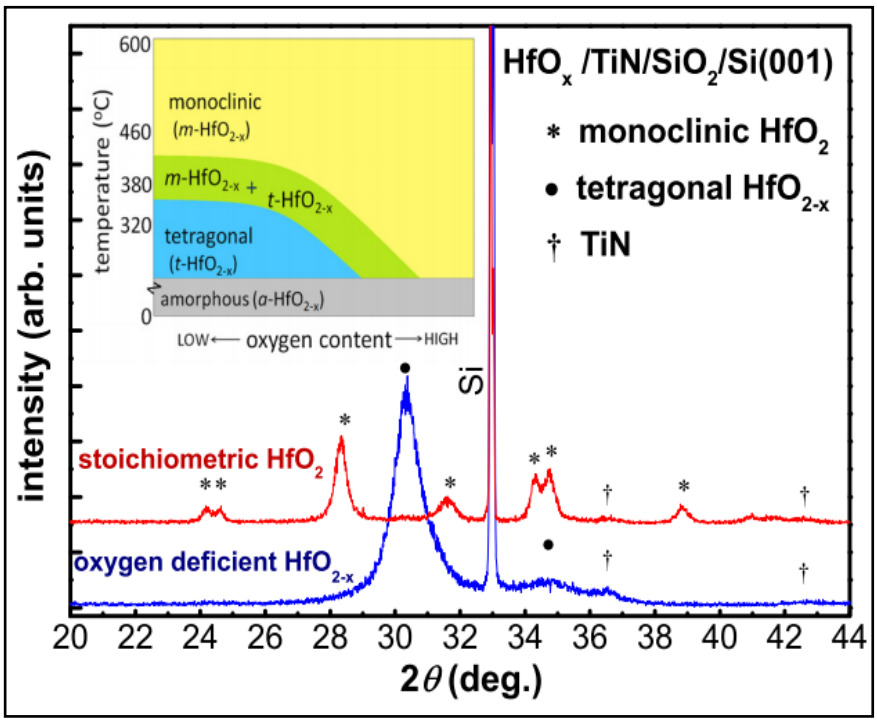


***Figure 1.4*** *XRD patterns demonstrating stabilization of the monoclinic and tetragonal phase in stoichiometric and oxygen deficient $HfO_2$ films. (adapted from [50])*

It is evident that while the stoichiometric $HfO_2$ crystallizes in monoclinic phase, oxygen deficient $HfO_2$ exhibits the tetragonal phase.[50] The stabilization of high temperature tetragonal or cubic phases in $HfO_2$ films are essentially governed by relative concentration of oxygen atoms and vacancies along with postdeposition annealing temperature and environment conditions. These phases become relatively more stable after engineering and optimizing the oxygen content present in film. The other crucial parameters like grain size and grain boundary energy also play a key role in such phase transformation processes.[44]

Besides the stabilization of tetragonal or cubic phase at room temperature in $HfO_2$ films, a similar cubic phase can also be stabilized in nanoparticles of $HfO_2$. **Figure 1.5** shows a direct precipitation of the monoclinic and cubic phase of $HfO_2$ obtained by utilizing an appropriate solvent without adding any surfactant and performing other post-synthesis treatments such as heating process. It has been suggested that the cubic phase of $HfO_2$ is achieved using a relatively more reductive solvent. After optimizing various synthesis parameters, the suitable preparation techniques have been proposed to produce

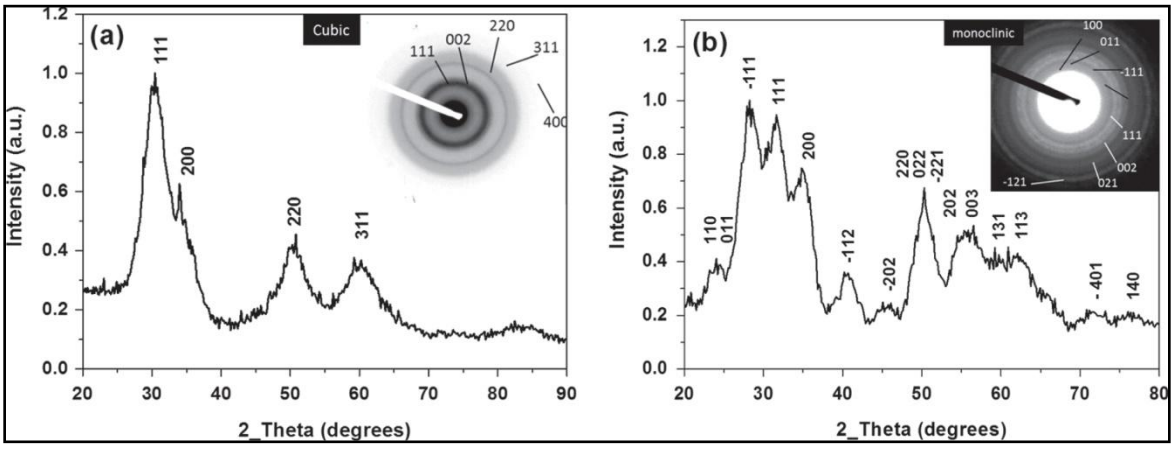


***Figure 1.5*** *XRD patterns of* ***(a)*** *cubic and* ***(b)*** *monoclinic $HfO_2$ nanoparticles. The insets show respective selected area electron diffraction (SAED) patterns. (adapted from [51])*

high-quality cubic $HfO_2$ nanoparticles which remain stable under ambient conditions.[51] Therefore, without any dopant, one can stabilize the high temperature cubic or tetragonal phase at room temperature by controlling and tuning of the stoichiometry of nanostructured $HfO_2$. However, the cubic or tetragonal $HfO_2$ stabilized in such a way is easily transformed to the undesirable low symmetry monoclinic phase after a slight modification of temperature in particular.

#### 1.1.3.2 Effect of Dopants

***i) Trivalent Ion***

The phase control in $HfO_2$ by incorporating dopant is one of the peculiar method to stabilize the high temperature and pressure $HfO_2$ phases at ambient conditions. The notion of doping trivalent ion into $HfO_2$ lattice is very much effective for phase transformation due to difference in the oxidation states of dopant and Hf cation. In $HfO_2$ lattice, when a trivalent ion replaces $Hf^{4+}$, an electron is produced which disturbs the charge equilibrium. In order to compensate these electrons, oxygen vacancies are generated in the lattice.[52] The mechanism for the stabilization of tetragonal or cubic $HfO_2$ depends predominantly upon the difference between ionic radii of dopant and Hf cations. If the trivalent ion having lower ionic radius than that of Hf substitutes in the lattice, relative energy of tetragonal phase with respect to monoclinic one decreases significantly which prefer to stabilize the tetragonal $HfO_2$. In this case, the nearest oxygen atoms move in direction of the dopant sites displacing other oxygen atoms outwards due to structural relaxation. On the other side, the replacement of Hf atoms with oversized dopants stretch the bond length between dopant and oxygen atoms. Here, the lattice strain originating because of dissimilar ionic

radii is relatively lower compared to tetragonal $HfO_2$ thereby stabilizing the cubic phase of $HfO_2$ at room temperature.[53]

It is known that while the monoclinic phase of $HfO_2$ contains two different kinds of oxygen atom configurations namely three fold and four fold coordinated with Hf, for high temperature tetragonal and cubic phase, the local surrounding of all oxygen atoms is identical in the lattice. The generated oxygen vacancies prefer to reside at four fold coordinated Hf site. In tetragonal or cubic $HfO_2$, the presence of oxygen vacancies reduces coordination number of Hf to 7 and also decreases the concentration of nearby oxygen atoms. The shifting of oxygen atom in such a way is strongly directed nearing to dopants rather than Hf atoms. This rearrangement of oxygen atoms necessarily forms eight fold coordination with dopant inducing more and more 7 fold coordinated Hf atoms in the lattice. In this regard, first principle calculation predicts the stability of tetragonal and cubic phases of $HfO_2$ by incorporating undersized dopants e.g. Al, P and oversized dopants e.g. Y, Gd and Sc, respectively.[53] This theoretical assumption has been supported by a few experimental reports showing the stabilization of cubic phase at room temperature utilizing trivalent rare earth (RE) Lu and Eu ions having higher ionic radius than Hf.[54] However, these reports do not present a thorough discussion on the stabilization of high temperature phase of $HfO_2$.

***ii) Tetravalent Ion***

On the basis of ionic radius of tetravalent ion, a similar stabilization of tetragonal and cubic phase can be perceived in nanostructured $HfO_2$. This is experimentally evidenced in case of Ce doped $HfO_2$. Since the ionic radius of Ce is more than that of Hf, it is capable of stabilizing the cubic phase of $HfO_2$ at room temperature.[55] The tetragonal phase

stability of $HfO_2$ after incorporating tetravalent dopants of smaller ionic radius is not very reliable and captivating. In this context, recently, after doping undersized tetravalent Si, an unusual orthorhombic (*O*) phase is discovered in $HfO_2$ films. It is noteworthy that this orthorhombic phase is of non-centrosymmetric nature instead of centrosymmetric orthorhombic one observed under high pressure condition discussed earlier in section 1.1.2. The existence of polar *O* phase in $HfO_2$ films essentially evokes promising ferroelectric properties.[56] Previously, the formation of such a polar *O* phase is also reported for chemically analogous $ZrO_2$ after doping Mg.[57] The non-centrosymmetric orthorhombic phase in $HfO_2$ films has been extensively researched by doping various divalent, RE trivalent and tetravalent ions having different ionic radii including Mg, Ba, Sr, Y, La, Nd, Sm, Er, Al, Ga, In, Co, Ni, Ge and Zr etc.[58] Specifically, the stabilization of polar orthorhombic phase in $HfO_2$ by Zr doping is more appealing and advantageous inducing excellent ferroelectric properties since it can be formed at lower crystallization temperature compared to Si doped $HfO_2$ films. In addition, there exists relatively a wide composition range for Zr doped $HfO_2$ in contrast to any other dopant. Different deposition techniques like atomic layer deposition (ALD), sputtering and pulse laser deposition etc can be utilized to achieve this orthorhombic phase in doped $HfO_2$.

In view of the emergence of non-polar orthorhombic phase in bulk $HfO_2$ with increasing pressure, the explanation for existence of polar orthorhombic phase in nanostructured $HfO_2$ appears quite different than the bulk. Following the comprehensive first principle calculation, it is believed that the substantial reduction in grain size inducing prominent surface energy effects could control the stability of this orthorhombic phase. The estimated surface energy corresponding to *O* phase is found to be in between the tetragonal

and monoclinic $HfO_2$.[59] However, the surface free energy calculated using such computational model considers only a definite size of grain in the film. It is well known that the polycrystalline oxides exhibit a specific grain size distribution. Now, the origin and phase evolution of the polar *O* phase in Zr doped $HfO_2$ is understood after taking into account such grain size distributions. The presence of this *O* phase is also influenced by other factors like film thickness, asymmetric stress, top capping electrode, dopant and annealing temperature etc.[41] More importantly, such *O* phase can be obtained in film thickness of ~10 nm or even less onto Si substrates. Owing to outstanding compatibility and stability of $HfO_2$ with Si, a new class of non-volatile memory termed as FeRAM is now being implemented for practical applications. A systematic retention tests of $HfO_2$ based FeRAM show promising features due to appropriate relative permittivity and coercive field compared to standard perovskite based ferroelectrics.

## 1.2 Magnetic Properties of $HfO_2$

Earlier, most of the study on crystalline $HfO_2$ primarily deals with the exploration of structural properties. Bulk $HfO_2$ shows strong diamagnetic nature since its *d*-shell is completely occupied with no unpaired electrons. When the size is reduced to nanometer range, an unconventional and intriguing magnetic properties can appear in nanostructured $HfO_2$ which are entirely different from the bulk counterpart. In $HfO_2$ films, an unusual ferromagnetism at room temperature or higher temperature was first reported in the year, *2004*.[60] This room temperature ferromagnetism (RTFM) is extremely compelling as both $Hf^{4+}$ and $O^{2-}$ are non-magnetic ions with $d^0$ cation closed shell configuration. For this completely unexpected behavior in thin films of $HfO_2$, a new term is coined called as $d^0$-magnetism. Following RTFM in $HfO_2$, a similar phenomenon is also investigated in other

TMOs like ZnO, NiO, $TiO_2$, $SnO_2$, $ZrO_2$ and so on.[61-65] Besides, RTFM is also reported for various nanostructured $HfO_2$ like nanoparticles, nanoclusters and nanorods.[66, 67] Since the discovery of RTFM in $HfO_2$ films, the origin of long range ferromagnetic ordering present in non-magnetic TMOs has been the subject of consistent and progressive research. It is widely believed that such RTFM phenomenon in TMOs is exclusively related to lattice point defects such as cation and anion vacancies. As TMOs are more prone to oxygen vacancies, the oxygen related electronic defects can be easily formed in the host lattice.

In case of nanostructured $HfO_2$, oxygen vacancies ($V_o$) are inherent in nature during synthesis and deposition process which dominate other lattice defects such as metal vacancy ($V_M$), oxygen interstitial ($O_i$), metal interstitial ($M_i$), oxygen antisite ($O_M$), and metal antisite ($M_O$) forming under different oxygen chemical potentials.[52] The high oxygen chemical potential minimizing the binding energy of oxygen molecules can facilitate the formation of Hf metal vacancy ($V_{Hf}$). On the other side, at low oxygen chemical potential, different neutral and charged oxygen vacancies are produced in the lattice.[68] The energy required to form $V_{Hf}$ is relatively higher than that of $V_o$. In addition, the formation of $V_{Hf}$ is also difficult due to its higher oxidation state. Moreover, these oxygen related vacancies can essentially tend to form a defect or impurity band below conduction band of $HfO_2$.[69] A simple model based on molecular mechanics method suggests that these oxygen vacancies usually reside onto the surface rather than the bulk due to significant difference in surface energies.[70] According to first principle calculation, in monoclinic $HfO_2$, there may exist various oxygen vacancies after charge trapping including $V_o^{- -}$, $V_o^{-}$, $V_o$, $V_o^{+}$ and $V_o^{++}$ which are further distinguished by their

respective three or four fold coordinated atomic configurations.[71] In $HfO_2$ lattice, the donor electrons which are localized by correlations and local potential fluctuations can couple with spins in defect bands forming the molecular orbitals around an oxygen vacancy in $HfO_2$. In this way, two donor electrons trapped in an oxygen vacancy can produce so called $F^o$ centers due to their specific spin arrangement which mainly induce an antiferromagnetic ordering. A singly occupied vacancies known as $F^+$ centers particularly develop the long range ferromagnetic ordering whereas an empty oxygen vacancies ($F^{++}$ centers) do not take part in establishing the ferromagnetism at room temperature in nanostructured $HfO_2$. It can be understood that the generated oxygen vacancies are capable of mediating long range RTFM in $HfO_2$ through $F^+$ centre exchange mechanism.[72, 73] Contrary to above reports on RTFM in nanostructured $HfO_2$, a few first principle investigations claim a radically different origin of such ferromagnetic ordering at room temperature. A possibility for short range ferromagnetic ordering due to isolated cation vacancy giving rise to high-spin defect state is anticipated in low symmetry monoclinic phase of $HfO_2$.[74] Some other reports even show the absence of RTFM in nanostructured $HfO_2$ and further suggest the origin of such RTFM due to external parasitic factors present in environment.[75, 76]

In general, the character of exchange between the defect states evoking RTFM is discussed in terms of impurity band formation. Explicitly, the super-exchange model does not fit in here since this can only gives rise to short-ranged antiferromagnetic ordering at concentrations of magnetic cations $x < x_p$ ($x_p$ is the cation percolation threshold). Such an existence of RTFM can also not be explained on the basis of the double-exchange mechanism dealing with ferromagnetic ordering facilitating observation of large magnetic

moments which is not the case in $HfO_2$. In addition, this mechanism can only occur within the mixed cation valence showing ferromagnetic interactions. In view of impurity band formation, the presence of defects in the lattice generates energy states within the band gap of $HfO_2$. An abundance of such defect related energy states tend to produce an impurity band near conduction band minimum. For ferromagnetic ordering, these materials have propensity to form shallow donors like charged $V_o$. Such donors can possibly form bound magnetic polarons when couple with cations in the 3*d* bands within their orbits. The interaction between donor electrons and the cations in the vicinity of molecular orbital induce the ferromagnetic ordering.[72] Such defect induced formation of the impurity bands effectively propagate ferromagnetic exchange if distance between the defects is higher than that of localization length. It is known that the spontaneous spin splitting of impurity band occurs when 3*d* density of states is larger satisfying the Stoner criterion. The spin split impurity band can also arise in the presence of magnetic defects. At appropriate defect concentration, such impurity bands tend to extend and mix with empty 3*d* states at the Fermi level. This can exchange electron from the impurity band to unoccupied 3*d* states resulting in spin-polarization of the impurity band. It further promotes and favors the long range ferromagnetic ordering at room temperature or even high Curie temperatures.[77]

RTFM observed in nanostructured $HfO_2$ is weak in nature since it is defect induced ferromagnetic ordering. This weak ferromagnetism can be significantly enhanced by oxygen engineering or incorporating a low concentration of transition metal ions/impurities. The ferromagnetic properties of $HfO_2$ has been shown to be affected in the presence of Y, Ni, Co, Fe and Al. Especially, the large magnetization is observed in $HfO_2$ nanoparticles after doping Ni which is mostly mediated by oxygen vacancies.

Consequently, different methods have been used to incorporate Ni metal ion into $HfO_2$ lattice to improve the ferromagnetism behavior.[78] On the other hand, Chang *et al.* demonstrate that the magnetization decreases with increasing concentration of cluster-free Co.[79] In Fe doped $HfO_2$, no obvious effect of Fe doping on RTFM is observed as the ferromagnetism arises because of oxygen related defects only.[80] For Y doped $HfO_2$ nanoparaticles, the ferromagnetic ordering improves upto a certain concentration of Y which further weakens at larger Y concentrations.[66] RTFM in nanostructured $HfO_2$ is controlled by oxygen vacancies content existing in the lattice whereas metal ion doping in most of the cases suppresses the ferromagnetic ordering by forming clusters or unwanted defect complexes highly unfavorable for RTFM. Wang et al. report the magnetic properties of RE (Gd) ion doped $HfO_2$ films. The study indicates very weak ferromagnetism in pure $HfO_2$ and no significant improvement of the ferromagnetic ordering is observed.[81] Surprisingly, the literature lacks of a systematic and thorough research study on the effect of rare earth dopants in modifying RTFM of nanostructured $HfO_2$.

## 1.3 Optical Properties of $HfO_2$

Owing to wide optical band gap and high refractive index of $HfO_2$, it is known to be completely transparent over a broad range of the electromagnetic spectrum encompassing visible region, in particular. The luminescence behavior of nanostructured TMOs reflects the characteristic of structural modifications and can be used as an efficient probe for investigating the local surrounding of host cation. A systematic analysis of the luminescence properties of $HfO_2$ can lead to exploration of various defect states in the host lattice, if present. Similar to parameters such as temperature and pressure including material composition changing the crystal structure of $HfO_2$, the resulting luminescence

properties can also evolve accordingly with structural modifications. The nanostructured $HfO_2$ exhibits intriguing intrinsic luminescence features in visible region useful for potential optoelectronic applications. As discussed, the nanostructured $HfO_2$ contains different lattice defects related to oxygen vacancies originating during synthesis and heat treatment processes. Such oxygen vacancy induced defects are likely to form intermediate energy levels within the bandgap of $HfO_2$. These defect states acting as electron traps are optically active in nature called as 'luminescent centers'.[82] Under UV light irradiation, $HfO_2$ predominantly shows a broadband emission spectrum producing blue light. The primary emission peaks in monoclinic $HfO_2$ are observed at ~2.1, 2.5, 2.9 and 3.6 eV distinctive to the defects states lying in bandgap.[83] Among the defect levels revealed from luminescence spectroscopy of $HfO_2$, the correct origin and nature of atomic defects providing the most intense emission peak at ~2.5 eV has been extensively studied by various research workers. Following the literature, on one side, it can be expected that the strong emission centered at ~2.5 eV in nanostructued $HfO_2$ arises due to oxygen vacancies.[51] On the other side, in chemically similar $ZrO_2$ system, an almost similar emission band is attributed to extrinsic metal impurities e.g. Hf, Fe and Ti present in the precursor having extremely low concentrations.[84] It is known that the optically active $Ti^{3+}$ ($3d^1$) ion is capable of producing 2.5 eV emission band via $3d^1(e_g \rightarrow t_{2g})$ electronic transition which is of radiative nature.[85] Later, a careful and closer inspection using other appropriate spectroscopic measurements and theoretical calculations establish the origin of 2.5 eV blue emission band in $HfO_2$ to be only defect related mainly comprised of charged oxygen vacancies formed after trapping of electrons.

The luminescence properties are greatly influenced by the crystal symmetry of the host. In particular, the hosts like $HfO_2$ having low symmetry monoclinic phase is investigated for its strong blue luminescence behavior. **Figure 1.6** shows the luminescence behavior of monoclinic phase $HfO_2$ revealing prominent emission peaks at ~2.2, 2.5 and 2.8 eV distinctly dominated by 2.5 eV emission band. However, in case of the high symmetry cubic $HfO_2$, along with these emission peaks, a characteristic peak is found to be located at ~3.1 eV.[86] The emission band at ~2.5 eV dominates the PL emission behavior of nanostructured $HfO_2$ irrespective of crystalline phase present in the host lattice. Also, the luminescence yield for the monoclinic $HfO_2$ is relatively much higher than that of the cubic $HfO_2$ nanoparticles.

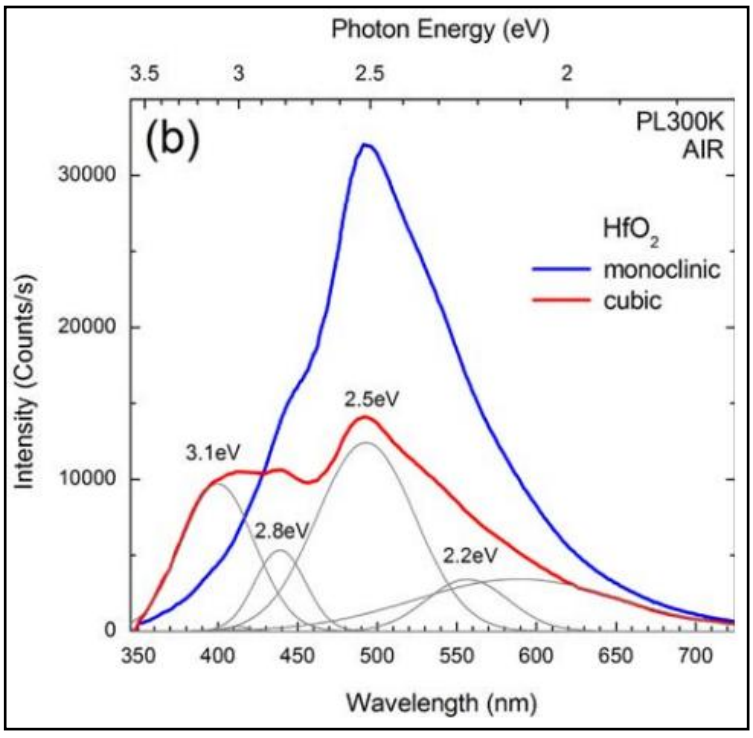


***Figure 1.6*** *The emission spectra of $HfO_2$ nanoparticles crystallized in the monoclinic (blue line) and cubic (red line) phase under ambient conditions. The deconvoluted peaks are grey in color (adapted from [86]).*

Apparently, the luminescence of monoclinic $HfO_2$ is associated only with different oxygen defects which lie deep in the impurity band. It is suggested that the characteristic emission peak at ~3.1 eV for cubic $HfO_2$ in no way can occur from the organic residues due to their large absorption threshold, usually greater than 4 eV. The other origin of same may be connected to $Hf^{3+}$ defect states and/or some extrinsic radiative recombination taking place near defect centers which appear to be of significantly different nature in case of cubic $HfO_2$.[51]

The luminescence response of $HfO_2$ can be varied considerably by changing temperature, defect concentration, size and shape of particles etc.[83] If the particle size is reduced to few nanometers, the luminescence behavior is drastically modified due to very large surface-to volume ratio leading to wide discrepancy in concentration of defects. The difference in particle shape can produce dissimilar efficiency for adsorption of impurities rendering various kinds of optically active defects.[86] In fact, a highly tunable luminescence features are obtained after varying only the annealing temperature and consequently the particle size. Under optimized synthesis conditions, even white light emission can be perceived in nanostructured $HfO_2$ for potential application in ultra-violet white light emitting diodes (UV-WLEDs).

The monoclinic $HfO_2$ is proven to be a promising host for most of the RE elements due to better compliance with optoelectronic applications. When a tiny amount of RE ion is incorporated into $HfO_2$ lattice, it can induce remarkable characteristic emissions related to RE ion due to the presence of high crystal field energy. As a host, $HfO_2$ is capable of enhancing the luminescence behavior of RE activator ions. Such notable improvement in RE emission properties of $HfO_2$ is achieved by energy transfer (ET) process taking place

between specific energy levels of the host and RE activator ion. In the presence of RE ions like Eu, Er, Tb and Ce etc, $HfO_2$ can produce a range of colors in the visible region.[54, 87-89] Different emissions in RE activator ions occur primarily because of the distinct intra-configurational *f-f* band transitions which can be dominated by electric or magnetic dipole transitions. In most of the RE ions, the electric dipole transition governs the emission behavior.[90] In contrast to singly RE ion doped $HfO_2$, incorporating double RE ions simultaneously in the host constructively modifies the luminescence properties leading to excellent control of RE ion emission behavior. In case of Eu doped $HfO_2$, after codoping Li, Ta, Nb, and V, only Nb provides an enhanced and strong luminescence properties. These codopants, however, serve as the charge compensating ions when $Hf^{4+}$ is replaced by $Eu^{3+}$ in the host lattice.[91] Similarly, the emission behavior of Eu and Tb codoped $HfO_2$ can dramatically evolve with varying dopant concentrations.[92] The existence of two different RE activator ions may produce the whole gamut of colors manifested by the significant exchange of energetic electrons within various *f-f* transition levels. For such RE codoped $HfO_2$, one of the two activator ions acts as the donor and can effectively sensitize the luminescence behavior of the other ion called as the acceptor. In this context, the transfer of energetic electrons from the donor to acceptor ion is understood on the basis of Förster and Dexter energy transfer mechanisms also termed as multipolar and exchange type interaction process, respectively. Either of the energy transfer mechanisms can be dominated depending upon the distance between donor and acceptor active ion. The exchange type interaction mechanism prevails when the critical distant between two active ions is less than that of ~6 Å. Above this critical distance, the multipolar interaction process controls the energy transfer between donor-acceptor ions.[93, 94] This energy

transfer of electrons within different levels of RE ions is essentially of nonradiative nature. The luminescence yield, thus can be improved considerably in RE codoped $HfO_2$

Looking at promising luminescent features and non-hazardous nature of RE doped $HfO_2$, it is being implemented in various biological imaging applications. The other luminescent materials such as quantum dots, dye-doped silica particles and metallic clusters have not been much revolutionized due to their poor photostability. On the other side, RE doped inorganic and biocompatible materials like $HfO_2$ are peculiarly used for cellular imaging, multiplexed histology, flow-cytometry, drug delivery, photodynamic therapy, *in vivo* whole animal and clinical imaging (e.g., angiography), tissue mapping and demarcation, real-time detection of intracellular events, signaling and bio-sensing, tracking cell migration, sensitive point-of-care detection including environment and bio-defense control.[95, 96] The inorganic based nanophosphors offer relatively much better photostability under severe conditions and do not degrade rapidly at the same time.

## 1.4 Resistive Random Access Memory Application of $HfO_2$

Since the first experimental report in year, *1967* on resistive switching in $Al/SiO_x/Au$ stratified structure, a number of metal oxide insulators have been substantially explored for resistive random access memory (RRAM) application. Among other emerging non-volatile memories like magneto resistive random access memory (MRAM), phase-change random access memory (PCRAM) and also FeRAM, RRAM can be integrated more easily due to its simple structure and great compatibility with current processing and scalability.[97] Basically, RRAM consists of a metal oxide insulator layer sandwiched between top and bottom metal electrodes. Such nonvolatile memory devices store and read information (i.e. 0 and 1) by rapidly switching between a low and high resistance states

(LRS/ON and HRS/OFF) under an applied bias voltage. In order to trigger the resistive switching, usually a certain initial bias voltage is required known as forming voltage ($V_F$) which is understood as the soft dielectric breakdown. In case of RRAM, the voltage at which the current in HRS increases abruptly to LRS is termed as SET voltage ($V_{SET}$). The voltage needed to switch from LRS to HRS state referring to RESET voltage ($V_{RESET}$) may occur in either positive or negative bias region.[98] Based on this observation, **figure 1.7** depicts two types of resistive switching modes possible in RRAM such as (i) unipolar and (ii) bipolar. For unipolar switching mode, both $V_{SET}$ and $V_{RESET}$ appear in either positive or negative bias region i.e. irrespective of electrical polarity. In the latter mode, $V_{SET}$ and $V_{RESET}$ are observed in positive and negative bias region, respectively or *vice-versa*.[97] In contrast to bipolar mode, the unipolar operation requires higher current to complete reset process which is due to the fact that the thermal effects govern the reset process corresponding to unipolar mode.[97]

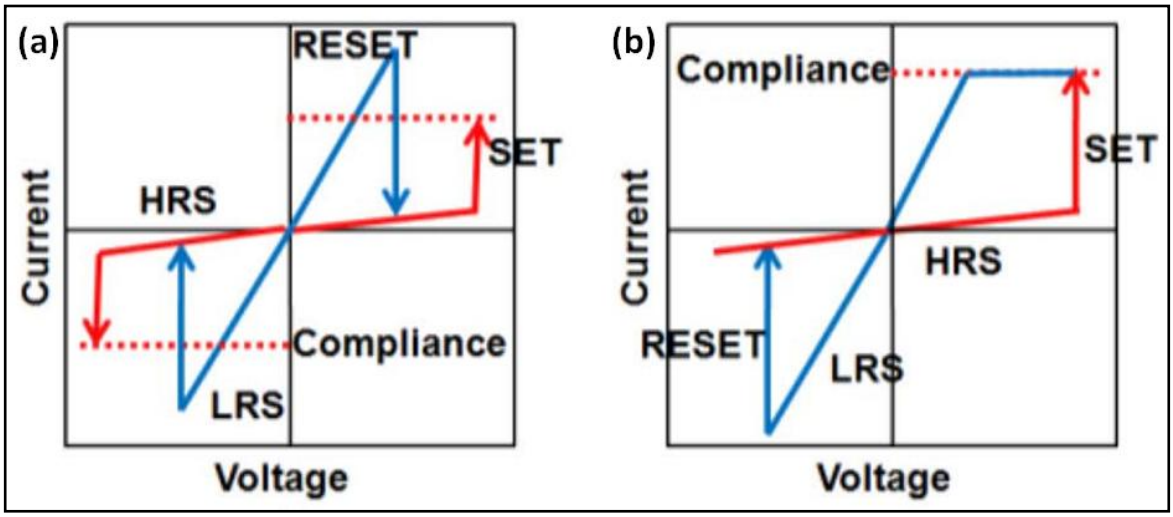


***Figure 1.7*** *Typical current-voltage (I-V) curves of RRAM in* ***(a)*** *unipolar and* ***(b)*** *bipolar resistive switching modes.*

The dominant current conduction mechanisms in SET and RESET processes are realized using different conduction models such as Schottky emission, Poole-Frenkel emission, Ohmic conduction and Fowler-Nordheim tunneling and space charge limited current in LRS and HRS states. In most of the cases, LRS state is governed by linear current-voltage behavior i.e. the Ohmic model whereas the current conduction in HRS is explained through non-linear current-voltage behaviors like Schottky emission ($\log(I) \alpha \sqrt{V}$), Poole-Frenkel (P-F) emission ($\log(I/V) \alpha \sqrt{V}$) and Fowler-Nordheim (F-N) tunneling ($I/V^2 \alpha V^{-1}$) and space charge limited current (SCLC) ($I \alpha V^2$).[97, 98] The resistive switching behavior in RRAMs is discussed in terms of the formation of conductive filaments (CFs), migration of oxygen vacancies/ions, Schottky barrier, cation migration and trapped charged carriers present at the interface or distributed randomly within metal oxide insulator film.[99] Different binary inorganic transition metal oxides like $TiO_2$, CuO, ZnO, NiO, CoO, $ZrO_2$, $HfO_2$, $Ta_2O_5$ and $Gd_2O_3$ etc have been systematically investigated for potential RRAM device applications.[98, 100] Among the binary metal oxides, $HfO_2$ is widely studied and preferred exhibiting enhanced resistive switching properties owing to its superior compatibility and thermal stability with CMOS processing and integration. $HfO_2$ based RRAM exhibits the stable, uniform and reproducible bipolar resistive switching behavior. It is broadly believed that the resistive switching characteristic in $HfO_2$ based RRAM is caused by the formation of several tiny localized conductive filaments (CFs) containing mobile metallic ions or charged oxygen vacancies generating conduction electrons. The switching between the HRS and LRS is described in terms of destruction and formation of such CFs, respectively occurring within the metal oxide layer. The rupture of CFs occurs due to local Joule heating effect. Under no bias condition, these

localized nanosize CFs show random motion within the metal oxide film. When a certain bias voltage is applied, these tiny CFs rearrange themselves and segregate to form the stronger and more conductive CFs.[98]

The oxygen vacancies driven resistive switching in $HfO_2$ based RRAM is necessarily controlled by modulating the concentration of oxygen content in the film. In some cases, even forming free resistive switching phenomenon is observed by precise tuning of the oxygen vacancies. Apart from the key role of oxygen content in switching behavior, other factors such as temperature, thickness of the film, top electrode material and dopant can significantly affect the performance of $HfO_2$ based RRAM. Thickness dependent switching behavior in oxygen deficient $HfO_2$ films reveals that the forming voltage can be suppressed considerably by optimizing thickness of the film.[50] In general, the bipolar resistive switching behavior is obtained using top electrode materials like TiN/Ti, Ti, Ta, Al and Pt.[98] However, if one utilizes top electrode material of Cu or Ni, the resistive switching behavior in $HfO_2$ is found to be of nonpolar nature.[101] The controlled resistive switching properties have been demonstrated in Al doped $HfO_2$ which occur because of the guided growth process of CFs.[102] After doping Ni into $HfO_2$ lattice, a large concentration of oxygen vacancies suggests the forming free resistive switching properties.[103] Moreover, RE ion, Gd doped $HfO_2$ shows much encouraging enhancement in RRAM device performance with better uniformity of different switching parameters. The promising RRAM feature is accomplished by minimizing the random motion of oxygen vacancy filaments formation which suppresses the oxygen ion migration barrier.[104] In fact, Gd doping can easily produce oxygen vacancies by reducing the $V_o$ formation energy attained due dipole formation between $V_o$ and Gd dopants. $Gd^{3+}$ ions

substituting $Hf^{4+}$ sites in the lattice drift the oxygen vacancies near Hf cation sites which eventually facilitate the controlled switching behavior in $HfO_2$.[105] Surprisingly, there exists meager reports dealing with RE ion doped $HfO_2$ based RRAM devices.

## 1.5 Objectives

The continuous downscaling of conventional gate dielectric i.e. $SiO_2$ has stimulated a progressive research to find a novel high-*k* dielectric material enabling us to overcome the major issues like high leakage current density, usually encountered in the current CMOS industry. For this reason, particularly, $HfO_2$ has been consistently studied for its deployment as an alternate to $SiO_2$ in CMOS technology due to its appropriate wide bandgap along with high-*k* value and outstanding thermal stability with silicon. $HfO_2$ possessing the monoclinic phase shows *k* value of ~15 which is four times higher than that of $SiO_2$ (~3.9). Based on above literature, the high temperature tetragonal and cubic phase of $HfO_2$ are technologically more important since they exhibit relatively larger *k* value such as ~70 and 30, respectively. Surprisingly, a few reports discuss the methodology to develop $HfO_2$ having high-*k* phases of either tetragonal or cubic by suitable dopants or controlling synthesis conditions. In this context, the optimization, comprehension and stabilization of the tetragonal or cubic phase of $HfO_2$ at room temperature is of utmost importance for its practical applications. Herein, the present work primarily aims to stabilize the high temperature cubic phase at room temperature after incorporating RE elements into nanostructured $HfO_2$ with optimized concentration along with processing temperature. Although the main objective of the thesis is inspired from a specific state-of-the-art problem, the outcomes of present work on nanostructured RE doped $HfO_2$ are of broader context and can be successfully implemented in various potential applications such as

imaging and memory devices etc. In addition to the systematic and concise literature review given in this chapter, the thesis offers a comprehensive discussion on the structure, magnetic, optical and electrical properties of nanostructured RE doped $HfO_2$ incorporated as following chapters:

Chapter 2 outlines the synthesis technique for preparation of pure and Dy and/or Sm doped $HfO_2$. The deposition of pristine and Sm or Dy doped $HfO_2$ thin films through electron beam evaporation technique is discussed briefly. A concise overview of the different instruments utilized in the thesis is provided. For example, the structural and microstructural characterizations of nanostructured $HfO_2$ have been carried out through X-ray diffraction (XRD), grazing incidence XRD, X-ray reflectivity, transmission electron microscopy and high resolution scanning electron microscopy. While X-ray photoelectron spectroscopy and electron probe micro analysis are used for elemental analysis, the optical properties have been explored by means of photoluminescence (PL) spectroscopy. Magnetic properties have been studied using magnetic property measurement system (MPMS), whereas the electrical properties are systematically investigated using semiconductor parameter analyzer for RRAM characterization.

Chapter 3 demonstrates structural transformation from monoclinic phase to high temperature cubic phase at room temperature after incorporating 11 at% of Dy. In contrast to diamagnetic behavior in bulk, $HfO_2$ nanoparticles show hysteresis loop indicating unusual ferromagnetism at room temperature. Surprisingly, RTFM in $HfO_2$ nanoparticles quenches after incorporating even 1 at% of Dy. On the other hand, 1 at% of Dy doped $HfO_2$ nanoparticles reveal excellent blue and yellow emissions producing cool white light. We propose an energy band diagram showing different transitions occurring in $Hf_{1-x}Dy_xO_2$.

In chapter 4, we show the stabilization of high temperature cubic phase of $HfO_2$ at room temperature by doping 12 at% of Sm. The phase transformation from the monoclinic to cubic phase is accompanied with a dramatic enhancement of lattice strain and reduction in particle size. Interestingly, $HfO_2$ nanoparticles reveal cool white emission without doping Sm. After incorporating 1 at% of Sm, $HfO_2$ produces strong emissions in near green and red regions. At higher Sm concentration, the PL behavior of $HfO_2$ diminishes significantly. Combining different excitation and emission processes, a schematic energy band diagram has been proposed.

Chapter 5 introduces a new concept of stabilizing the cubic phase of $HfO_2$ after codoping Dy and Sm. It has been established that after codoping Dy and Sm upto the total concentration of 13 at%, the stabilization of high temperature cubic phase of $HfO_2$ at room temperature is achieved. Dy and Sm codoped $HfO_2$ shows prominent emission peaks in blue, yellow and near red spectral regions producing purplish color light. We reveal the existence of an energy transfer from $Dy^{3+}$ to $Sm^{3+}$ ions inducing strong characteristic emissions. The rich PL emission behavior of the robust luminescent Dy and Sm codoped $HfO_2$ nanoparticles are considered as a prospective dusting powder for latent fingerprints (LFPs) imaging for promising application in forensic science. LFPs developed on several surfaces including aluminum foil, float glass, black colored glass, wine and red colored plastic sheets and stainless steel exhibit third-level details, good background contrast, selectivity and acceptable resolution.

Chapter 6 has been dedicated to exploration of pure and Dy or Sm doped $HfO_2$ films. The most important observation in this chapter is the stabilization of cubic phase at room temperature by doping at most half of Sm or Dy concentration compared to the

nanoparticles. These films exhibit the bipolar switching behavior which is of forming-free nature distinctive to RRAM device. After analyzing the switching behavior, it has been recognized that an abundance of oxygen vacancies forming 8-fold oxygen coordination to dopant ion play a crucial role in the stabilization of cubic phase at RT and also governs the forming-free switching behavior in $HfO_2$ based RRAM devices.

Chapter 7 outlines the main findings of the present work. We present the scopes of this work to be done in near future.

# Chapter 2

## 2.1 Introduction

Nanostructures of TMOs are synthesized using several established routes such as precipitation, co-precipitation, high energy ball milling, inert gas condensation, plasma deposition, reverse micelle technique, citrate precursor technique, micro-emulsion, hydrothermal reaction, sol–gel technique, polymer pyrolysis, liquid mix technique, etc. Every synthesis technique possesses a few advantages and disadvantages from technological and industrial point of view. The selection of an appropriate method to prepare versatile TMOs with different shape and size should be done cautiously. A synthesis route that is facile, rapid, inexpensive and capable of mass-production is sought for preparation of specific nanostructured metal oxides showing relevant and desired physical as well as chemical properties. In this chapter, we briefly summarize the synthesis method and deposition technique employed for the preparation of pure and rare earth doped $HfO_2$ powders and thin films, respectively. Afterwards, a concise overview of different characterization techniques utilized for studying the samples are discussed.

## 2.2 Powder Synthesis Method

In this work, $HfO_2$ powders were prepared through a simple Pechini type sol-gel technique. The flow chart of synthesis is shown in **figure 2.1**. For pure $HfO_2$ powders, the stoichiometric amount of hafnium chloride ($HfCl_4$, 99.9%, Alfa Aesar) was mixed with 2M citric acid ($C_6H_8O_7$) solution under constant stirring using a Teflon coated magnetic bead. Dy and/or Sm doped $HfO_2$ powders with varying concentration were produced by addition

of appropriate amounts of dysprosium nitrate ($Dy(NO_3)_3$, 99.9%, Sigma Aldrich) and samarium nitrate ($Sm(NO_3)_3$, 99.9%, Alfa Aesar) to previous solution mixture. Thereafter,

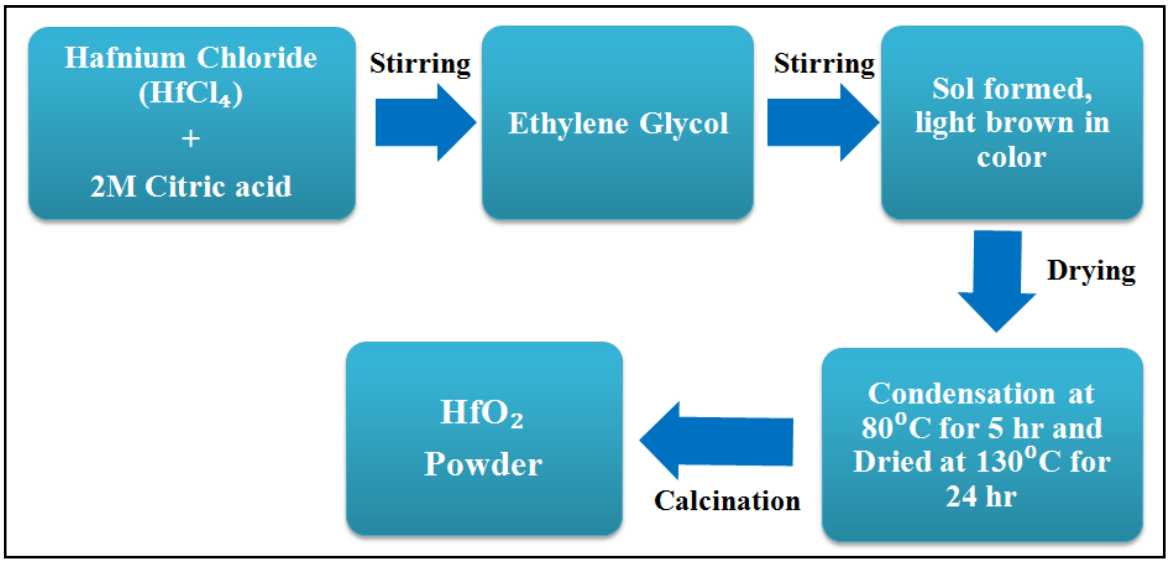


***Figure 2.1*** *Process flow of Sol-gel method for the synthesis of pure $HfO_2$ and rare earth doped $HfO_2$ powders.*

we obtained a clear solution ensuring complete dissolution of different precursors. A clear sol was formed after mixing the ethylene glycol (EG) ($C_2H_6O_2$) into the prepared solution leading to polymerization of sol. After heating the sol at 80 $^oC$ for 5 h to complete the condensation process, the sol was dried at 130 $^oC$ for 24 h in order to obtain the precursor resin. The dried out product was then pulverized in an agate mortar and pestle to obtain fine powder. Due to the presence of organic impurities, the prepared fine powder was slightly brown in color. Finally, the synthesized powders were calcined at different temperatures in air for 5 h to obtain pure $HfO_2$ and Dy and/or Sm doped $HfO_2$ which were white in color.

## 2.3 Thin Film Deposition

In the present thesis work, we have utilized the electron beam evaporation (EBE) technique to prepare $HfO_2$ thin films. EBE technique is a high vacuum based method peculiarly employed for thin film deposition of several metal oxides. The EBE deposition system requires the base pressure of ~$10^{-6}$ mbar in deposition chamber, facilitating the route for generated electrons from the electron gun to target material for evaporation. The pure target materials are available as pellet, ingot or rod. The upgraded EBE deposition systems working on an arc suppression system can also work at even ultrahigh vacuum levels ($10^{-9}$ mbar). There exists the possibility of deployment of different kinds and number of the evaporation materials as well as electron guns simultaneously in a single system. The power of electron guns may vary from a few tens to hundreds of kW.

**Figure 2.2** depicts the schematic diagram of a standard EBE deposition system. The strong beam of energetic electrons can be produced by different techniques like thermionic emission and field emission including anodic arc method. Under the presence of appropriate magnetic field, the electron beam is accelerated to a high kinetic energy which is then bend towards the target material for deposition. When this electron beam strikes the material, the electron quickly loses its kinetic energy transferring into other forms of energy after interacting with target material. A sufficient thermal energy produced in such a way that it heats and consequently melts or sublimates the target material. After attaining attaining the suitable temperature at desired vacuum level, a vapor plume appears from the melted or sublimated target material. This vapor plume of target material is coated onto the substrates. The accelerating voltage can be used from 3 – 40 kV. After optimizing this voltage (20 – 25 kV) with suitable beam current, most of the kinetic energy of electrons is

transformed into equivalent thermal energy. The incident energy of electron is partially lost for generating X-rays and other secondary electron emissions.

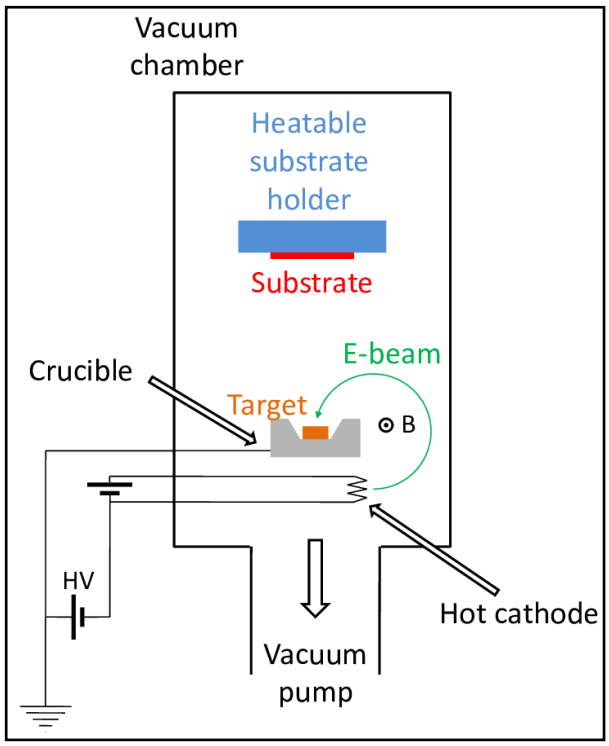


***Figure 2.2*** *A schematic representation of electron beam evaporation (EBE) deposition system. (the direction of magnetic field (B) is out of the page).*

In particular, EBE deposition system can be built using following configurations:

1. Electromagnetic alignment

2. Electromagnetic focusing

3. Pendant drop configuration

While the target material in its ingot form is usually used for electromagnetic alignment and electromagnetic focusing, a rod shaped target evaporation material is

employed in the pendant drop configuration. The crucible or hearth made of copper metal is used for mounting the ingot shaped target material. However, the target in rod shape is placed at one end in the socket. Due to production of excess heat after incidence of electron beam, the holders of target material like crucible and socket is cooled continuously. In general, continuous circulation of cool water is utilized for same. EBE deposition system can provide relatively large rate of evaporation in the order of $10^{-2}$ g.cm$^{-2}$.s.

EBE deposition system is capable of evaporating materials with high melting point such as refractories e.g. titanium carbide and borides, including zirconium boride without showing decomposition of the material. The evaporated target material is directly deposited onto different substrates. There are some refractory metal oxides and carbides which fragment in the process of evaporation leading to a off-stoichiometry of the target material. This is generally observed in case of alumina. When the electron beam strikes alumina, it can possibly dissociates and form aluminum, $AlO_3$ and $Al_2O$. Such decomposition can also occur in silicon carbide and tungsten carbide materials producing elements with dissimilar volatilities. However, most of the target materials like $HfO_2$ having very high melting point (>2500 $^oC$) are easily deposited using EBE system without undergoing any decomposition. In addition, EBE deposition technique is also very useful for depositing different metals such as silver, copper, aluminum, and tungsten etc. This deposition technique offers substantially wide range for rate of deposition from 1 nm per minute to very high rates of a few μm per minute. The structural and morphological properties of deposited films can be controlled during deposition with great utilization efficiency of the material.

$HfO_2$, Sm and Dy doped $HfO_2$ films were deposited onto cleaned $p^{++}$-Si substrates through EBE deposition technique using individual pure pellet targets of $HfO_2$, Sm and Dy

doped $HfO_2$. During the film deposition, the substrate temperature was kept at room temperature and the vacuum chamber base pressure was maintained at ~6 X $10^{-6}$ mbar. After deposition, the films were annealed at 550 $^{o}$C for 60 min in air followed by subsequent characterizations.

## 2.4 Device Fabrication for RRAM

### 2.4.1 Cleaning of $p^{++}$-Si

Prior to deposition, first, highly doped p-type silicon substrate ($p^{++}$-Si) of size 1 X 1 $cm^2$ is dipped into strong Piranha solution ($H_2SO_4$ : $H_2O_2$ = 7 : 1) for 3 min to etch the silicon surface for removal of unwanted native oxide and subsequently washed several times with DI water. After this treatment, the silicon substrates are successively cleaned using acetone and isopropanol for 5 min each with the help of ultrasonic bath followed by drying process via passing dry air. The thoroughly cleaned $p^{++}$-Si substrates are then used for deposition of thin films.

### 2.4.2 Fabrication of Metal-Insulator-Metal (MIM) Test Structures

$HfO_2$, Sm and Dy doped $HfO_2$ films are deposited onto the thoroughly cleaned $p^{++}$-Si substrates. In order to perform electrical characterization, MIM test structures consisting of Al/$HfO_2$/ $p^{++}$-Si are fabricated. $p^{++}$-Si acts as the bottom electrode and aluminum is used for the top electrode material. Using metal shadow mask, the circular Al top electrode with diameter of 500 μm is deposited on the top of $HfO_2$/ $p^{++}$-Si through thermal evaporator under the chamber pressure of ~$10^{-6}$ mbar. The schematic of MIM test structure is shown in **figure 2.3**.

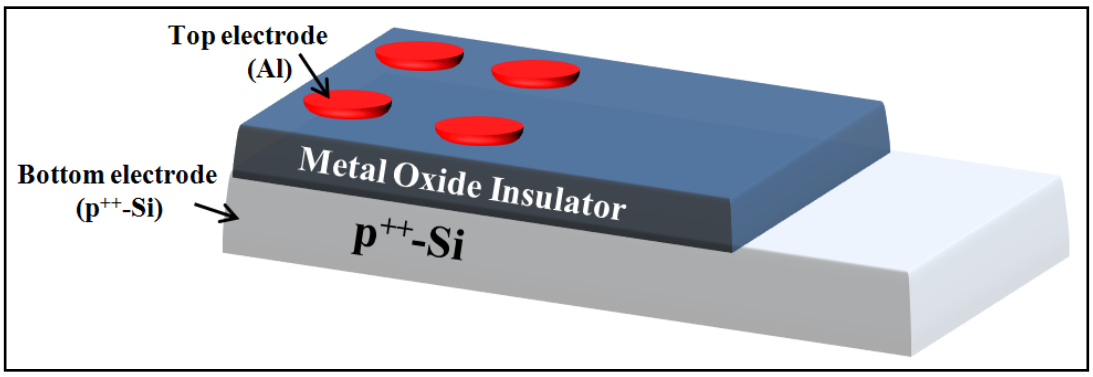


***Figure 2.3*** *The schematic diagram of metal-insulator-metal (MIM) test structure.*

## 2.5 Characterization Techniques

Pure, Dy and/or Sm doped $HfO_2$ nanostructured samples have been systematically characterized by employing appropriate techniques to analyze structure, magnetic, optical and electrical properties. The different characterization techniques utilized in the present thesis work are briefly discussed below.

### 2.5.1 X-ray Diffraction (XRD) for Powder Samples

XRD is the most widely used technique primarily employed to determine the crystal structure of a particular material. A non-destructive technique like XRD is peculiarly utilized as the preliminary characterization tool for extracting structure related information such as phase formation, crystallite size and lattice strain etc. In this technique, an electromagnetic wave having the wavelength of ~1 Å is diffracted from the crystal lattice planes oriented in different direction in crystal. This is achieved due to comparable order of magnitude of the X-ray wavelength and crystal lattice. XRD essentially facilitates the identification of different crystalline structure present in the material. The basic principle of XRD is based on the Bragg's law which states that the incident X-rays are diffracted from a

set of equally spaced lattice planes in the crystal that interfere constructively. These diffracted X-rays interfere constructively if the path difference between them is an integral multiple of the X-ray wavelength. This is given by Bragg and known as Bragg's law which is expressed as, $2d_{hkl}\,Sin\theta = n\lambda$ where, $d_{hkl}$ is called as the interplanar distance (*hkl* are Miller indices), $\theta$ is the Bragg's angle, $n$ is an integer indicating order of diffraction ($n$ = 1 for XRD) and $\lambda$ is X-ray wavelength. An illustration of the Bragg's law is demonstrated in **figure 2.4**.

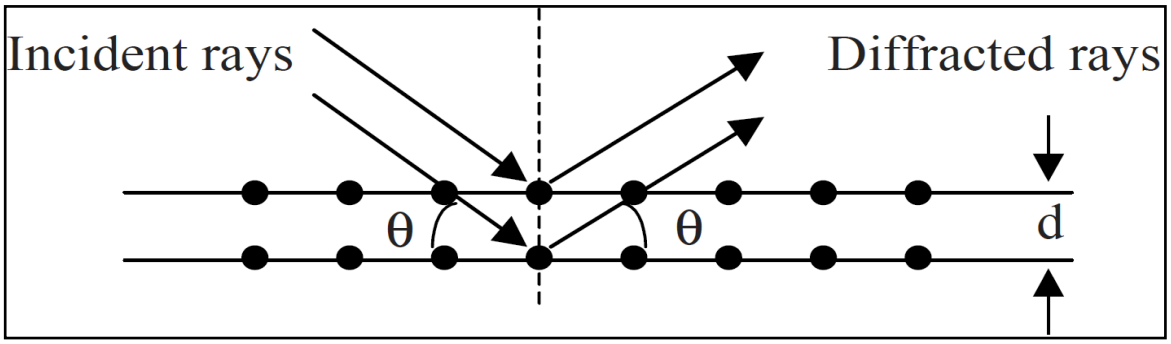


***Figure 2.4*** *A representation of the incident X-rays and their diffraction from equidistant lattice planes.*

Due to the constructive interference satisfying the Bragg's law, the diffraction pattern exhibits high intense peaks at certain scattering angles. In general, while the crystals possessing low symmetry structure e.g. monoclinic reveal several diffraction peaks because of numerous lattice planes, a few number of diffraction peaks are observed in case of high symmetry structures such as cubic and tetragonal containing certain lattice planes. The nature of diffraction peaks and their intensities is also dependent upon the size and shape of particles in the crystal.

In practice, an accelerated electron beam of required energy is directed towards the copper metal target which eventually produces X-rays. The collimated characteristic X-rays ($K_\alpha$) having wavelength of 1.54 Å are utilized to characterize the material. Most of the diffractometer works on the para-focusing (or Bragg-Brentano) configuration. This geometry is the most common and well suited for different materials. The samples with flat surfaces are easily diffracted for collection of data using the detector. The detector essentially converts diffracted beam into a count rate. The detector and sample can rotate by an angle $2\theta$ and $\theta$, respectively. Finally, the plot consisting of a series of diffraction peaks as a function of diffraction angle is realized that can be used for analysis of the crystal structure. Usually, the XRD patterns are recorded in the range of $2\theta = 10 – 120^o$.

In this work, XRD patterns were obtained on a Rigaku Miniflex X-ray diffractometer using Cu K$\alpha$ ($\lambda$ = 1.54 Å) operating in Bragg-Brentano geometry. The indexing of XRD patterns were identified using Joint Committee on Powder Diffraction Standards data (JCPDS). Using Le-Bail profile fitting of FULLPROF program, the different structural parameters like lattice constants and cell volume are extracted for synthesized samples. This fitting technique is based on matching the suitable generated intensities with experimental data to determine the particular crystal structure of a specific space group.

### 2.5.2 Grazing Incidence X-ray diffraction (GIXRD) for Thin Films

GIXRD works on the same principle of Bragg's law. While performing measurements of thin films, the XRD instrument used particularly for powder samples produces the high intensity diffraction peaks from the substrates resulting into weak signal from the thin film. Consequently, in such cases, the signal-to-noise ratio is very low

rendering poor information related to structure of the film. In contrast to Bragg-Brentano geometry, GIXRD uses the low incident angle near critical angle and the detector performs a $2\theta$ scan. At a low and constant angle of incidence angle, X-ray beam does not penetrate into the thin film which increases the diffraction coming from films rather than the substrate. Here, we have used GIXRD from Rigaku SmartLab equipped with PhotonMax high-flux 9 kW X-ray source of rotating Cu anode producing Cu K$\alpha$ ($\lambda$ = 1.54 Å). It uses the high-energy-resolution 2D multidimensional semiconductor detector for 0D, 1D and 2D measurement modes. This instrument comes with a high-resolution $\theta/\theta$ closed loop goniometer drive system with an available in-plane diffraction arm. The embedded Cross-Beam-Optics (CBO) allows automated switchable reflection and transmission optics. For all prepared thin film samples, GIXRD patterns are collected from $2\theta$ = 20-80 $^{o}$ at a scan rate of $3^{o}$/min.

### 2.5.3 X-ray reflectivity (XRR)

XRR is one of the versatile and potential surface sensitive technique used for the measurement of thickness of thin films including multilayers, surface along with interface roughness, surface density gradients and layer density etc. In this work, we have used Bruker D8 Advance diffractometer with X-ray source of wavelength 1.54 Å to estimate the thickness and film density using X-ray reflectivity (XRR) measurements. The experimental XRR patterns were then fitted with suitable stack models using Parratt software.

### 2.5.4 Electron Probe Micro Analysis (EPMA)

EMPA, a non-destructive technique is extensively used for elemental determination of samples in the form of a solid. In this technique, a highly collimated beam of energetic electrons having the typical energy of 5 – 30 keV excites the X-rays of specific element.

The obtained X-ray spectrum exhibits distinct features related to different elements constituting the sample. Both qualitative and quantitative analysis can be perceived utilizing the X-ray spectrum. revealing a specific wavelength or photon of definite energy. A comparison of relative intensities of different characteristic lines provide quantitative information of element concentration in the sample. In practice, EPMA includes other spectroscopic instrumentation like wavelength dispersive spectroscopy (WDS), energy dispersive spectroscopy (EDS), scanning electron microscopy (SEM) and back scattered electron (BSE) imaging. Therefore, it is capable of offering a facile detection of elemental composition. Due to the combination with WDS spectrometers which work on Bragg's law, this instrument is highly sensitive even to extremely low element concentration up to a few tens of ppm (parts per million) without compromising the accuracy of detection. With limited spatial resolution of ~1 mm, the spatial distributions are collected as line spectrum or 2D (two-dimensional) map.

Here, EPMA, CAMECA, SX Five has been employed as an efficient tool for facile detection and analysis related to distribution of constituting elements for investigating the composition of the synthesized samples. WDS spectra were recorded for elemental analysis. A focused electron beam obtained with 15 kV accelerating voltage having a beam current of 4 nA was used for analysis. TAP (thallium acid phthalate), PET (pentae´rythriol) and LLIF (long lithium fluoride) crystals were further used to record the spectra.

### 2.5.5 Transmission Electron Microscopy (TEM)

TEM is primarily used to examine the microstructure of the material. It also offers vital information related to morphology such as shape and size of the particles including their specific size distribution histograms (i.e. particle size with frequency of particles). A

variety of TEM instruments e.g. high resolution TEM (HRTEM), scanning TEM (STEM) and analytical TEM (ATEM) are employed for different investigations. The instrumentation of standard TEM includes: (i) an electron gun, (ii) the vacuum system, (iii) focusing electromagnetic lenses, (iv) the high voltage generator and (v) imaging electronic devices. The collimation of electron beam is achieved using the electromagnetic condenser lenses. This beam exhibits relatively lower wavelength rendering excellent resolution under 0.2 nm. The well focused beam of very high energy typically more than ~200 keV is incident onto the sample which scatter and partially transmitted towards the objective lens that is imaged upon the charge coupled device (CCD) camera. Apart from common imaging mode, TEM can produce a specific diffraction patterns.

This work utilizes an FEI make Tecnai $G^2$ 20 Twin instrument for imaging, selected area electron diffraction (SAED) pattern and high resolution TEM. The size and shape of particles including particle size distribution histogram could be realized from micrographs and analyzed using ImageJ software. SAED patterns exhibit distinct and continuous concentric rings which are examined after estimating inverse of their radii and matching with interplanar spacing (*d*) calculated from XRD data. HRTEM imaging mode revealed lattice information at atomic scale. The distinct lattice planes in HRTEM are realized for estimation of *d* value corresponding to a specific crystal plane.

### 2.5.6 Scanning Electron Microscopy (SEM)

SEM finds substantial use in analyzing topography of the sample. It primarily images the texture of different surfaces. The incident electron beam onto the sample surface ionizes the atoms which can consequently emit the loosely bound electrons called as the secondary electrons. These secondary electrons exhibit relatively low energy in the

range of ~3 to 5 eV. Such electrons are capable of marking the position of the beam very precisely which contained information related to topography of the surface. The secondary electrons can be easily detected due to their low energy. A high contrast image is formed after scanning the beam onto a screen or computer monitor. With proper detection mode, remarkable contrast against topography can be achieved. SEM shows good spatial resolution of the order of 10 nm or better, thereby resolves most of the surface structures. Using different kinds of detectors, SEM can be used for extended implementation in cathodoluminescence (CL). We have utilized field emission, FE-SEM, Nova Nano-SEM of FEI make for recording images and energy dispersive spectra (EDS) of the specimen.

### 2.5.7 X-ray Photoelectron Spectroscopy (XPS)

XPS known as electron spectroscopy for chemical analysis (ESCA) examines the elements, oxidation state of the constituent element and valence band structure by probing the surface of specimen. Since, this is a surface sensitive technique, it provides essentially the relative composition on the surface only. XPS is based on the photoelectric effect i.e. the emission of electron following excitation of core level electrons by energetic X-ray photons of energy, $hv$. The kinetic energy (K.E.) of electrons emitted in such is expressed as follows:

$$\text{K.E.} = hv - \text{B.E.} - \phi \qquad (2.1)$$

where B.E. is the binding energy of an individual electron and $\phi$ is the work function. Explicitly, when the energy of X-ray photon is larger than the binding energy, the photoelectrons are emitted from the core levels. [Stickle et al. (1992)]. These photoelectrons can be identified by their respective kinetic energy. The XPS spectra are drawn between the frequency of emitted electrons as a function of their K.E. The B.E. of

different electronic state is calculated with respect to the Fermi energy level. For a certain photon energy, the K.E. distribution of the photoelectrons implies the energy distribution of electronic states. These photoelectrons are usually scattered from nearby electrons, plasmons and/or phonons which slow down energetic electron after partially losing their energy. Due to significant loss in energy, the photoexcited electrons do not pass through the specimen. This undesirable scattering of photoelectron results into unwanted secondary inelastic background intensity. Such scattering is more prominent within the low range of kinetic energy occurring because of strong electron-electron interaction. Although X-ray can penetrate upto large depths into specimen, only the photoelectrons originating from a depth of a few tens of angstrom can be detected due to high degree of scattering. After the collision or scattering, photoelectrons with sufficient kinetic energy surpass the work function barrier and reaches the detector.

In general, the scattering and collisions between emitted electrons is reduced when the chamber is evacuated to ultra high vacuum. This enhances the mean free path of the emitting electrons which easily reaches to the detector. The monoenergetic soft X-rays are more appropriate energy source for exciting the photoelectrons. A compatible electrostatic analyzer is used to analyze the excited photoelectrons. In this study, XPS measurements are performed on VSW and AMICUS make X-ray photoelectron spectrometer utilizing radiations of Al-K$\alpha$ (1486.6 eV) and Mg-K$\alpha$ (1253.6 eV), respectively. The sample preparation chamber is evacuated to ~$10^{-8}$ Torr whereas the vacuum level of sample analysis chamber is maintained at ~$10^{-9}$ Torr. The scanning is first carried out to collect the complete range of energy i.e. survey scan. Afterwards, for the precise elemental analysis and sample composition in our study, O 1*s*, Hf 4*f*, Sm 3*d* and Dy 4*d* core level spectra are

selectively recorded. All the recorded core level spectra were calibrated with respect to C 1*s* peak centered at ~284.8 eV. XPS spectra were deconvoluted using XPS 4.1 software.

### 2.5.8 Magnetic Measurements

Magnetic properties of the synthesized samples are investigated by means of field and temperature dependent magnetization measurements employing magnetic properties measurements system (MPMS3 of Quantum Design, USA). This instrument uses vibrating sample magnetometer (VSM) and the superconducting quantum interference device (SQUID) for the measurement of magnetic moment. This facility is avaiable at Central Instrument Facility (CIF), IIT (BHU), India. A concise overview of including the working principle of both VSM and SQUID is provided below.

**i) Vibrating Sample Magnetometer (VSM)**

VSM is capable of measuring the magnetic moment of the specimen maintaining excellent accuracy. DC magnetization measurements of samples are performed with VSM operating between temperature range of 2 - 400 K and magnetic field of ± 7 Tesla. In this magnetometer, the measurement of magnetic moment with high precision is achieved with induction method. This method essentially involves the measurement of voltage which induces in a set of detection coils when the magnetic moment changes slightly in the sample. In practice, the measurement of induced voltage at the detection coil can be performed by vibrating speciemen with constant frequency under a uniform magnetic field.

In a specimen, there exists numerous magnetic dipole. in the beginning, the specimen is fixed at the center of the detection coil. When it is displaced to a certain distance in time, *t*, the change in flux ($\phi$) inducing a voltage given by $v = d\phi/dt$ which is measured in the detection coils. Usually, these detection coils are placed inside a solenoid

producing the magnetic field. The resulting moment in specimen is then measured with respect to applied magnetic field.

**ii) SQUID Magnetometer**

In order to measure minute magnetic moment in the specimen, SQUID is known to be the most suitable and sensitive technique. This device measures very small magnetic field utilizing the superconducting loops prenset in Josephson junction. Specifically, SQUID indirectly meausres the magnetic field of specimen. In general, when the specimen passes through superconducting detection coils connected with the SQUID via superconducting wires. This enables the flow of current from the detection coils to inductively coupled high quality sensors. The current from these coils is converted to equivalent voltage through SQUID. The whole assembly of instrumentation can be divied into following primary components: the main device i.e. SQUID, a magnetic flux transformer with appropriate detection coils, the superconducting magnetic coil, heat switches including suitable magnetic shielding configuration. Superconducting detection coils do not response to uniform and linear magnetic fields since the coils are set as second-order gradiometer having counter wound outer loops. When the local magnetic field changes, it produces a certain current in the detection coils. In practical situations, SQUID can response to every small change in the magnetic field. For this reason, the magnetic shielding is of utmost importance to prevent the sensor detecting stray fields arising from ambient or laboratory or the large magnetic fields originating from superconducting coil. The small area where magnetic field changes in detection coils, the heaters are used to remove the standing currents in the superconducting loops by raising them beyond their critical temperature. SQUID offers remarkable sensitivity of ~5 x $10^{-8}$ emu and frequency

range of 0.1 - 1 kHz. The measurement and removal of background ac phase shifts for each measurement is done through direct phase nulling technique. The rate of temperature change is 10 K/min from 300 to 10 K and then cool down very slowly from 10 to 2 K at 2 K/min.

### 2.5.9 Photoluminescence (PL) Measurements

PL spectroscopy is a nondestructive and widely used technique to study the electronic structure of different materials. Under irradiation of light, the electrons are transfterred to excited state after absorbing energy of the photon and while coming back to ground state, lose this energy in the form of emission or luminescence. The photoluminescence is the emission of certain wavlength of light when the sample is exposed to light. The emissions of light are realized in different ways i.e. spectrally, spatially and temporally. The optical excitation of electrons is termed as the transfer of energetic electron to definte allowed excited states. The relaxation of these electrons towards ground or lower energy states can either emit light through a radiative process or may not produce light which is known as the non radiative process. The emitted light exhibits energy equal to the difference between final (excited) and initial (ground state) energy levels of the participating electrons. For the PL spectroscopic measurements, laser light or xenon lamp is used as the excitation source with variable energy. The time dependent PL decay measures the respective rate of radiative recombination process. The nonradiative recombination centers are analyzed by the temperature dependent behavior of the PL intensity. PL technique is also very much useful for analyzing the purity, crystalline quality and concentration of impurity and/or defects present in the material. An excitation spectrum is obtained for a particular emission wavelength which is partly similar to an

absorption spectrum. At a certain wavelength known as the excitation wavelength, the specimen can produce the emission spectrum characteristic of the materials. For the fixed excitation and emission wavelength, the PL decay curves are recorded as a function of time.

PL spectrofluorometer measures and collects the spectra of fluorescence and phosphorence from the sample. During the fluorescence mode, the excitation and emission spectra are recorded for a range of wavelength. PL instrument can be modified with additional attachments for analyzing the emission behavior with time, temperature, concentration and polarization etc. A standard fluorescence spectrometers contains following main components shown in **figure 2.5**.

**Illuminator source:-** The illuminator is a continuous source of light obtained either by monochromatic laser or LED or broadband xenon lamp. The light originating from illuminator source is collimated through a set of elliptical mirrors along with lenses and delivered to the entrance slit of the excitation monochromator via optical fibers. The light source and excitation monochromator are separated using the window made of quartz. This is also used to release out the excess heating that may damage the light source.

**Monochromators:-** In practical PL instruments, there exists two different monochromators namely the excitation monochromator and emission monochromator. These monochromators offer high resolution for the complete wavelength range utilizing appropritate reflective optics by reducing spherical aberrations and re diffraction.

**Gratings:-** In the monochromator, the reflection grating is used to disperses the incident light occurring beacuse of the embedded vertical grooves and provides a good spectral resolution. The spectrum can be collected by a ruled blazed gratings with 1200

lines/mm(l/mm) blazed at 330 and 500 nm for excitation and emission monochromator, respectively. $MgF_2$ layer onto these gratings prevents the unwanted oxidation.

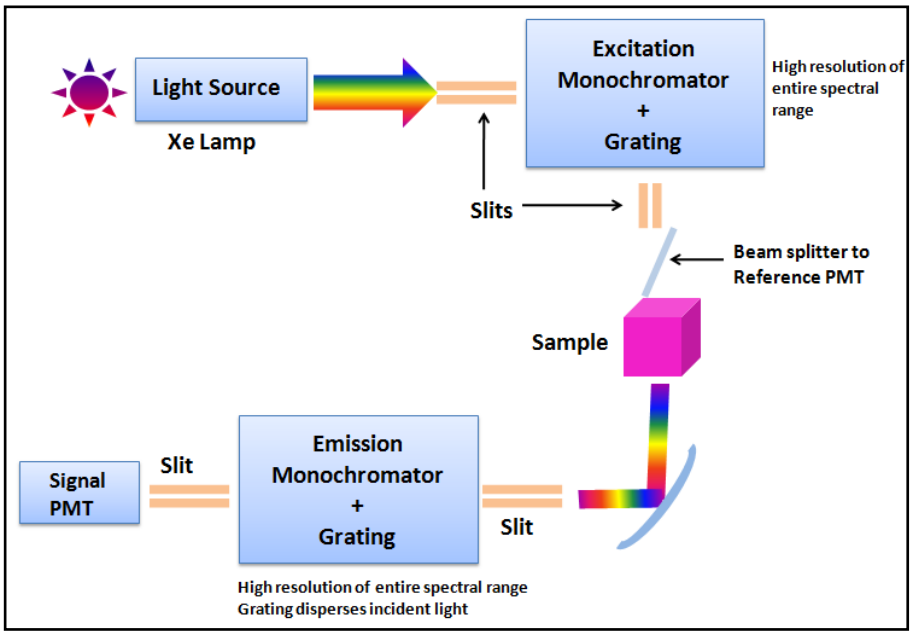


***Figure 2.5*** *A standard PL spectrofluorometer indicating different components used in the experimental setup.*

**Slits:-** Both the monochromators contain entrance and exit slits which can be controlled for required amount of light. At the excitation monochromator, slit width allows certain band of light to transfer towards the sample. The slit at emission monochromator can be adjusted for signal intensity at the detector. An appropriate slit width produces the maximum intensity maintaining a high resolution over the whole spectral range.

**Detectors:-** There are two types of detectors present in the spectrofluorometer i) reference detector and ii) signal detector. A reference detector is used for the light source in which wavelength correction and light source output with respect to time is monitored. This detector is kind of photomultiplier tube (PMT) placed infront of the sample. The fluorescence signal detector is also a PMT transferring the signal to the photon counting module. In present thesis work, the room temperature excitation, emission spectra along

with time resolved decay curves have been measured with a Horiba, Jobin Yvon, Fluorolog using the excitation source of a 450 W Xe arc lamp. The spectral resolution of the above spectrometer is 1 nm. The braod spectral range spans from 200-2000 nm for collecting excitation and emission spectra. Further, CIE (*Commission Internationale de l'Éclairage*) diagram has been used to characterize the hue and purity of different colors. In practice, CIE diagram drawn into two dimension (2D, *xy*) plot consists of chromaticity coordinates (*x, y, z*) and tristimulus values (X, Y, Z) expressed as following mathematical relations.

$$x = X/(X+Y+Z),\ y = Y/(X+Y+Z),\ z = Z/(X+Y+Z)$$

X, Y, Z represents primary colors red, green and blue which reconstruct hue and various combinations of colors with distinct wavelengths which are easily perceived by a standard observer. Within CIE 2D *xy* diagram, a horseshoe shape is formed for a wide range of wavelength spectrum (chromatic values) producing all available pure color chromaticity. For a given emission spectrum, *x,y* are calculated using dedicated software which provide a point position in CIE diagram indicating nature and purity of produced color.

### 2.5.10 Current-voltage (*I-V*) Measurements

The current-voltage (*I-V*) characteristics of MIM test structures (**figure 2.3**) are performed on the Keysight, USA make semiconductor parameter analyzer (Model No.: B1500A). *I-V* measurements are carried out after sweeping the applied DC bias voltage in a sequence of 0 V→ 4 V→ 0 V→ -5 V→ 0 V. The electrical contact of MIM was made using probe micromanipulator. During *I-V* measurements, the bottom electrode ($p^{++}$-Si) has been grounded and the bias voltage applied to the top electrode only. In order to avoid undesirable electrical breakdown of devices, the compliance current was fixed at 7 mA during the measurements.

# Chapter 3

## 3.1 Introduction

In this chapter, we have systematically studied the structural evolution of $HfO_2$ nanoparticles after doping with Dy concentration ranging from 1 to 11 at%. The monoclinic phase of $HfO_2$ transforms to the high temperature cubic phase when Dy concentration reaches 11 at%. The high temperature cubic phase remains stable at room temperature. The intermediate concentration of Dy shows a mixed phase of monoclinic and cubic. No such structural transformation from monoclinic to cubic by doping Dy in $HfO_2$ nanoparticles has been reported in the literature. Surprisingly, while the room temperature ferromagnetic behaviour observed in $HfO_2$ is quenched after doping of 1 at% of Dy, the photoluminescence studies show excellent emissions of blue and yellow light. A systematic study on structural, microstructural, magnetic and photoluminescence properties of Dy doped $HfO_2$ nanoparticles are discussed in this chapter.

## 3.2 Results and Discussion

### 3.2.1 Elemental Analysis

The composition of the pure and Dy doped $HfO_2$ samples have been examined using EPMA. In EPMA technique, the high energy electron beam is incident on a sample surface that generates X-rays of different wavelengths. These X-rays generated through atomic transitions between different shells are then captured by specific crystal monitor present in the instrument.[106, 107] Back scattered electron (BSE) imaging has been employed to investigate distribution of constituting elements having high and low atomic

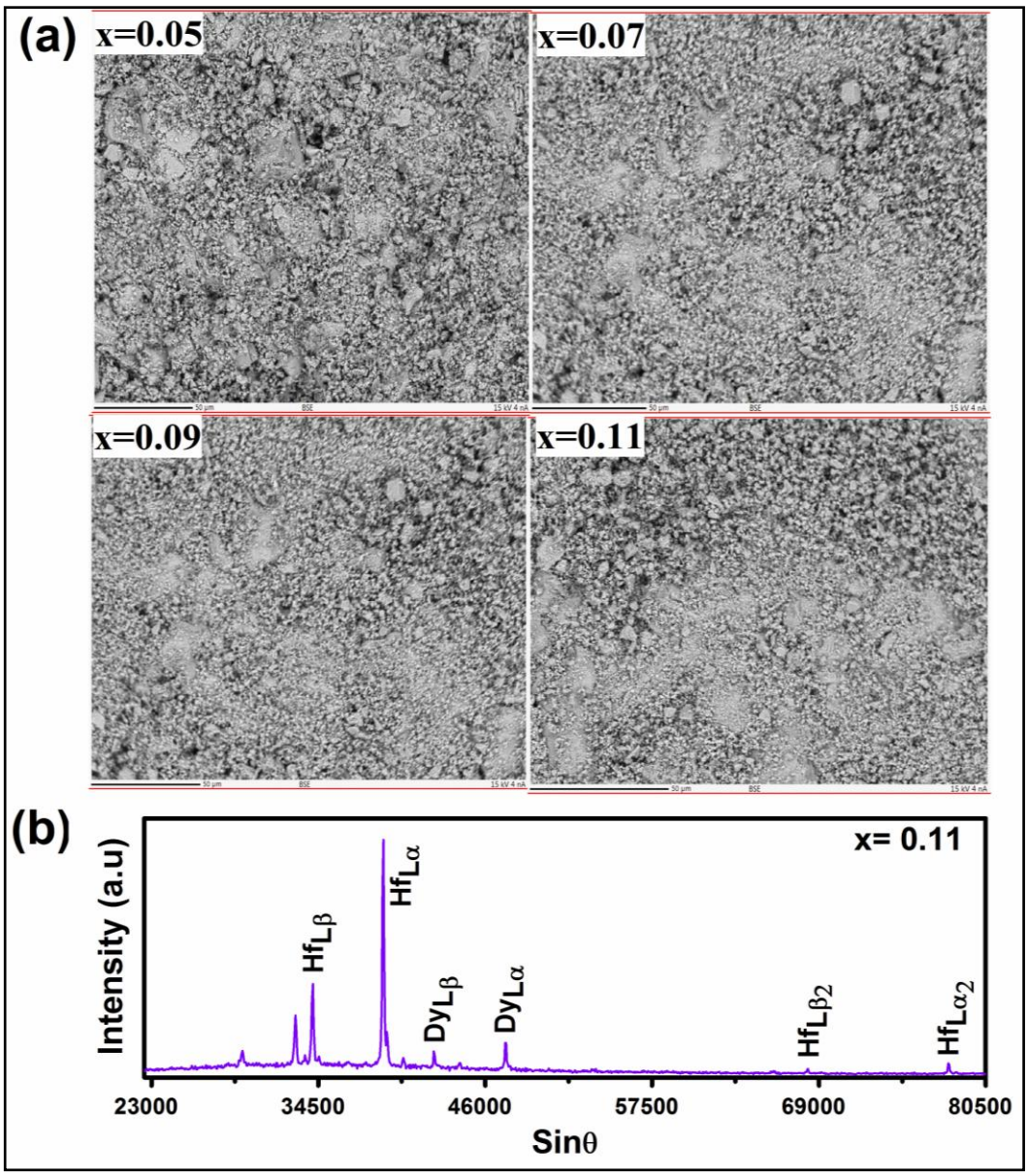


***Figure 3.1 (a)*** *Back scattered electron (BSE) images for x = 0.05, 0.07, 0.09 and 0.11, respectively and* ***(b)*** *Wavelength dispersive spectra (WDS) for x = 0.11.*

numbers as depicted in **figure 3.1 (a)** for x = 0.05, 0.07, 0.09 and 0.11, respectively. The contrast of different areas obtained in BSE image is not similar everywhere since it is dependent of the atomic number of constituting elements. Thus, BSE images contain reliable information regarding portion of higher atomic number elements are brighter, areas

having low atomic number elements show lower contrast.[107] All BSE images explicitly show a uniform distribution of constituting elements present in Dy doped $HfO_2$. Wavelength dispersive spectra (WDS) have also been taken for prepared samples shown in **figure 3.1 (b)** for x = 0.11. WDS spectra confirm the presence of majority species i.e. Hf and a trace of Dy in Dy doped $HfO_2$. The dominant peaks corresponding to Hf can be clearly seen and have been indexed as $Hf_{L\alpha}$, $Hf_{L\alpha 2}$, $Hf_{L\beta}$, and $Hf_{L\beta 2}$, respectively. The peaks associated with Dy have been labeled as $Dy_{L\alpha}$ and $Dy_{L\beta}$.

### 3.2.2 Structural Analysis and Phase Transformation

X-ray diffraction (XRD) patterns of $HfO_2$ calcined at 500, 700 and 900 $^oC$ have been measured to examine the phase and crystallinity of the particles (**figure 3.2**). While

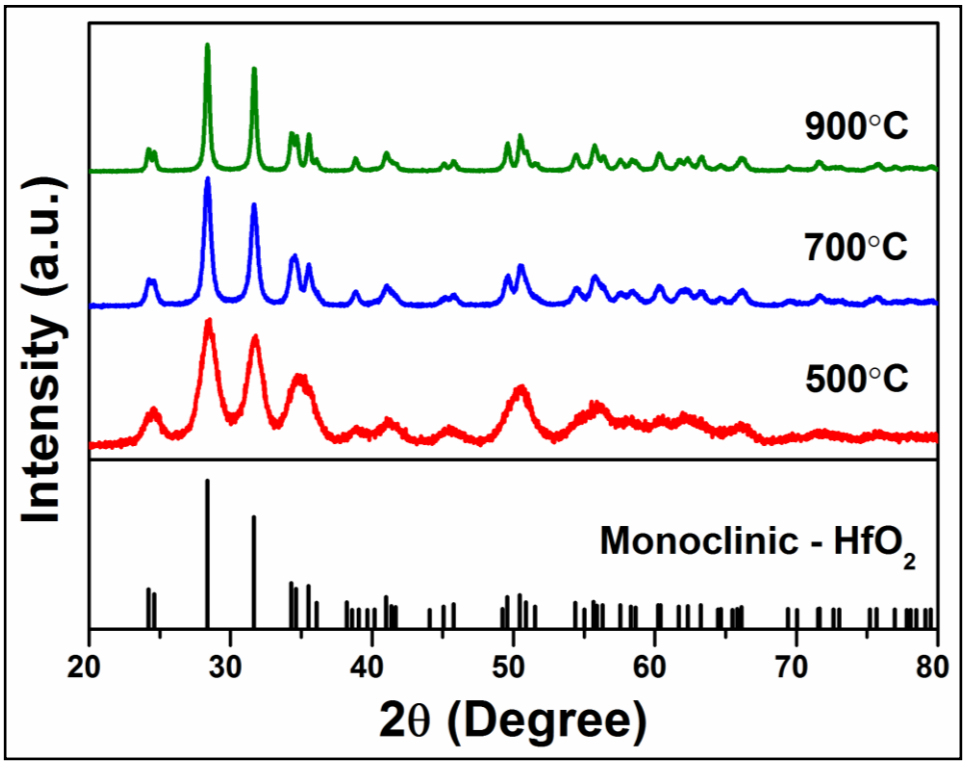


***Figure 3.2*** *X-ray diffraction patterns of $HfO_2$ calcined at 500, 700 and 900 $^oC$.*

sample calcined at 500 ºC exhibits broad diffraction peaks indicating fine particles, with an increase in calcination temperature to 900 $^{o}$C, diffraction peaks are well distinguished and become sharper indicating well crystalline nature . The observed diffraction peaks such as (011), (110), ($\bar{1}$11), (111), (020), (200), (021), ($\bar{2}$11) and (112) are well matched with the monoclinic phase (*m*-phase) of $HfO_2$ with space group, $P2_1/c$ (JCPDS card no. 78-0049). No impurity phase has been identified within the detection limit of the instrument. As the $HfO_2$ powders show well crystalline nature, we have fixed the calcination temperature at 900 $^{o}$C for $HfO_2$ doped with the various concentration of dysprosium (Dy).

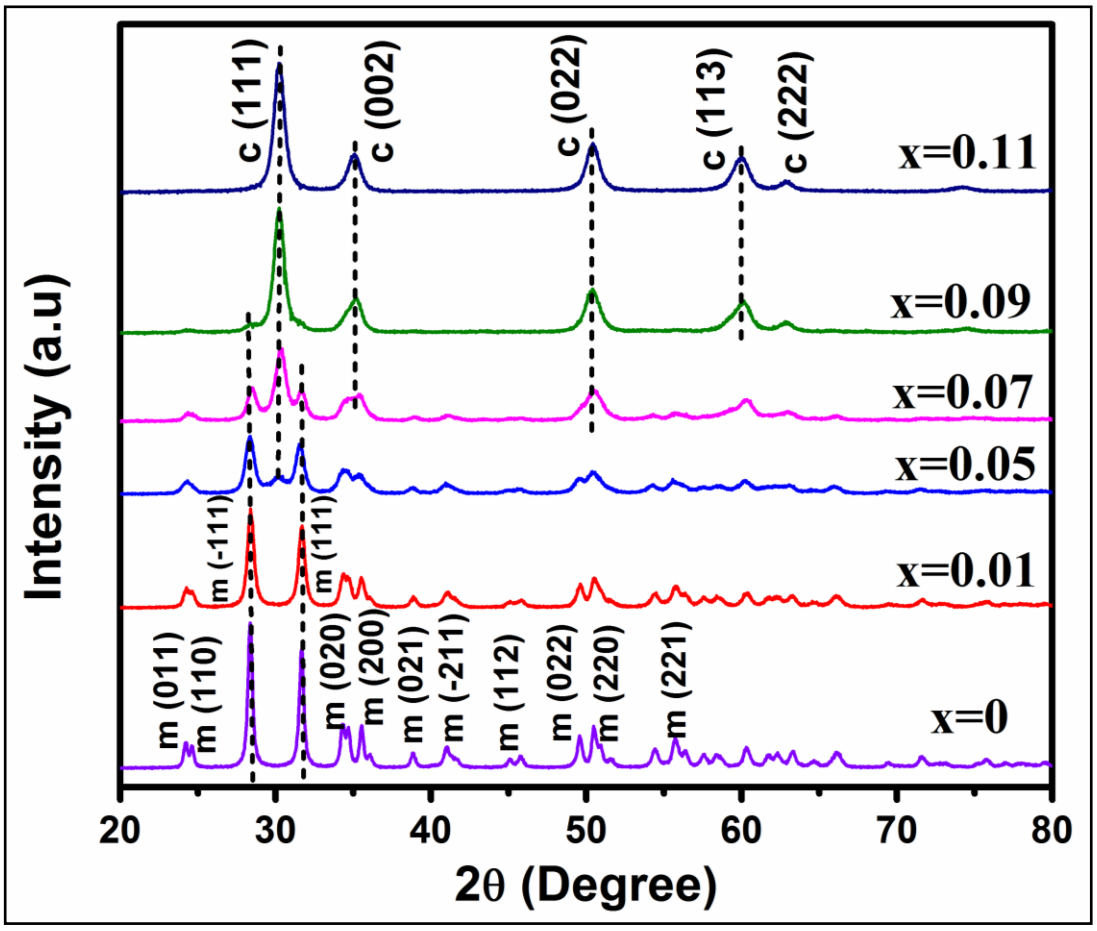


***Figure 3.3*** *XRD patterns of $Hf_{1-x}Dy_xO_2$ ($0 \leq x \leq 0.11$) samples calcined at 900 $^{o}$C.*

XRD patterns of $Hf_{1-x}Dy_xO_2$ ($0 \leq x \leq 0.11$) are shown in **figure 3.3**. At lower Dy concentration (x = 0.01), the diffraction peaks are matched with the monoclinic phase as in pure $HfO_2$ except for the decrease in peak intensity. However, in x = 0.05, in addition to the peaks corresponding to the monoclinic phase, a weak characteristic peak at $2\theta = 30.20^o$ is observed, which matches with the (111) of cubic phase (JCPDS card no. 53-0560). At x = 0.07, diffraction peaks observed in XRD pattern correspond to the mixed phase of monoclinic and cubic. At x = 0.09, cubic phase becomes more pronounced at the expense of monoclinic one. At the highest dopant concentration i.e. x = 0.11, characteristic diffraction peaks along (111), (002), (022), (113) and (222) planes correspond to pure cubic phase (*c*-phase) of $HfO_2$ with space group, $Fm\bar{3}m$ (JCPDS card no. 53-0560). No peak of $Dy_2O_3$ phase is found in any Dy doped $HfO_2$ samples. This suggests that $Dy^{3+}$ ions substitute $Hf^{4+}$ ions in both monoclinic and cubic lattice. For the first time, we show that monoclinic phase of $HfO_2$ transforms to the high temperature cubic phase by doping Dy upto 11 at%. The high temperature cubic phase of $HfO_2$ becomes stable at room temperature.

Further, we have fitted the XRD patterns for x = 0 and 0.11 using Le-Bail profile fitting of FULLPROF program with pseudo-Voigt function, shown in **figure 3.4**. Pure $HfO_2$ is fitted with $P2_1/c$, monoclinic phase and x = 0.11 is fitted with $Fm\bar{3}m$ corresponding to the cubic phase. **Table 3.1** summarizes the extracted cell volume and cell parameters from Le-Bail refinement. It is worth to mention that incorporation of Dy in $HfO_2$ lattice increases the lattice parameter of the pure cubic phase of $HfO_2$ 5.095 to 5.119 Å for x = 0.11. It may be vividly observed that while no significant change in cell volume of monoclinic phase is observed, cubic phase shows an increase of 1.4%. The observed

increase in cell volume of the cubic phase further confirms the replacement of $Hf^{4+}$ ions with $Dy^{3+}$ which is having relatively larger ionic radius than $Hf^{4+}$ ion. This clearly indicates that a significant number of $Dy^{3+}$ ions acquiring $Hf^{4+}$ ion sites stabilize the high symmetry cubic phase even at room temperature. We have estimated the phase fraction by the integral peak area ratio of the cubic peak (111) to monoclinic peak (111) or ($\bar{1}$11).

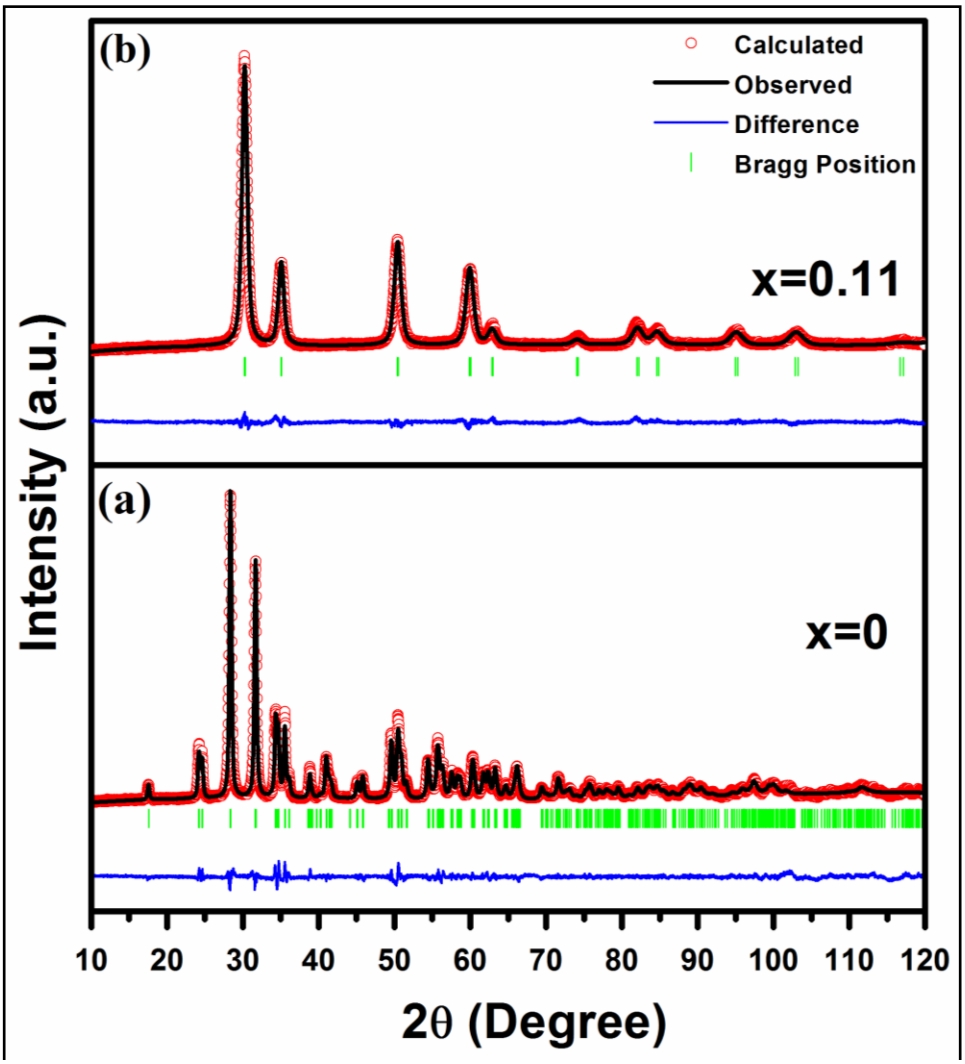


***Figure 3.4*** *Le-Bail profile fitting of XRD patterns using FULLPROF program* ***(a)*** *x = 0 with $P2_1/c$ and* ***(b)*** *x = 0.11 with $Fm\bar{3}m$.*

| JCPDS card no./Sample | Space group | Cell parameters | | | |
|---|---|---|---|---|---|
| | | a (Å) | b (Å) | c (Å) | Volume (Å$^3$) |
| 78-0049 | $P2_1/c$ | 5.117 | 5.175 | 5.291 | 138.32 |
| 53-0560 | $Fm\bar{3}m$ | 5.095 | 5.095 | 5.095 | 132.26 |
| $Hf_{1-x}Dy_xO_2$ (x = 0) | $P2_1/c$ | 5.117 | 5.176 | 5.290 | 138.302 |
| $Hf_{1-x}Dy_xO_2$ (x= 0.11) | $Fm\bar{3}m$ | 5.119 | 5.119 | 5.119 | 134.12 |

***Table 3.1*** *Standard JCPDS data for monoclinic and cubic phase of $HfO_2$ and refined cell parameters for $Hf_{1-x}Dy_xO_2$ (x = 0 and 0.11).*

Variation of $A_{CP(111)}/A_{MP(111)}$ or $A_{MP(T11)}$ with Dy concentration reveals that peak integral area ratio increases with increasing Dy concentration. While both the monoclinic and cubic phases coexist at an intermediate Dy concentration (x = 0.05 - 0.09), a complete cubic phase is eventually observed when x = 0.11. Williamson-Hall (W-H) method is employed to separate the particle size and lattice strain of the XRD line broadening using the following equation (1).[108]

$$\frac{\beta \mathrm{Cos}\,\theta}{\lambda} = \frac{k}{D} + \frac{4\varepsilon \mathrm{Sin}\,\theta}{\lambda} \qquad (1)$$

where β is full width at half maximum (FWHM in radians), k is constant related to shape of particle θ is Bragg angle, ε is lattice strain, D is the crystallite size and λ is the wavelength of X-ray.

In general, a plot drawn between 4Sinθ and βCosθ (straight line expected) allows one to extract the particle size and lattice strain from its intercept and slope, respectively. All samples show non-zero slopes indicating strain in both monoclinic and cubic lattices. The variation in particle size and lattice strain with Dy concentration are plotted as shown

in **figure 3.5**. In pure monoclinic phase, while particle size is of ~40 nm, pure cubic phase shows particles of around 10 nm in size. Although particle size is reduced by four times, the strain is increased by twice in cubic phase showing a maximum at 9 at% of Dy. One may note that strain is found to be higher in the range of 5 to 9 at% when the mixed phase of monoclinic and cubic is observed.

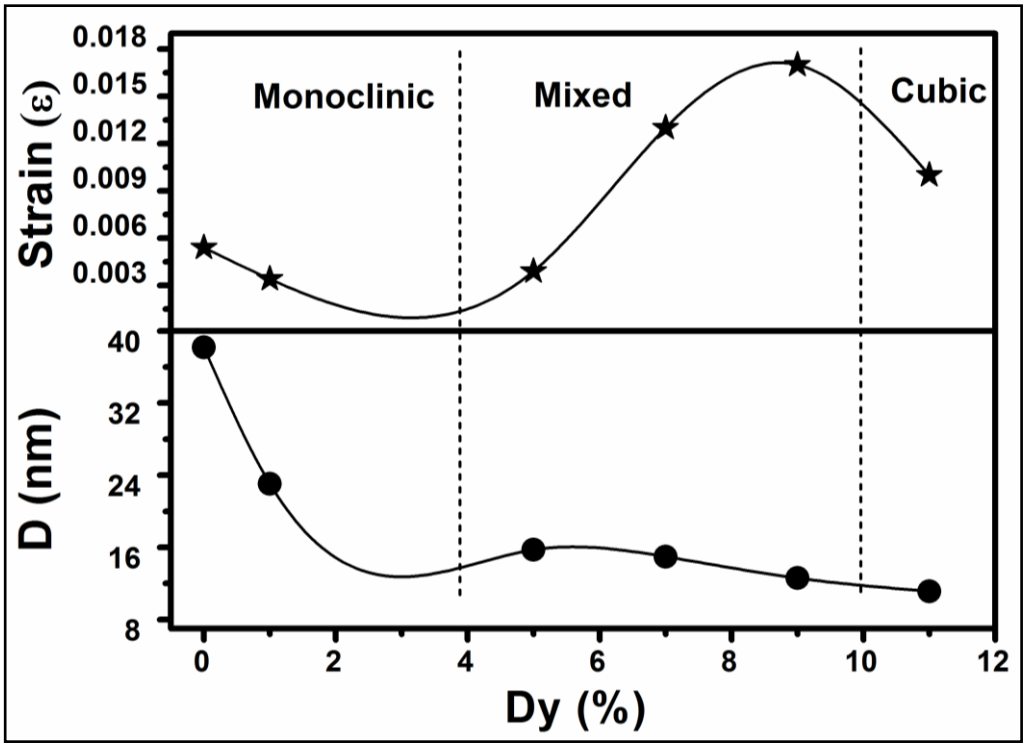


***Figure 3.5*** *Variation of crystallite size (D) and lattice strain (ε) in* $Hf_{1-x}Dy_xO_2$ *(*$0 \leq x \leq 0.11$*) samples.*

### 3.2.3 Microstructural Analysis

Transmission electron micrographs of monoclinic (x = 0) and cubic phase (x = 0.11) of $HfO_2$ show that the particles are slightly agglomerated and semi-spherical in shape (**figure 3.6**). From the particle size distribution histogram shown in the insets of **figure 3.7**

**(a) and (c)**, the average particle size is found to be ~36 and ~10 nm for x = 0 and 0.11, respectively, which matches well with the estimated average particle size from W-H plot. **Figure 3.7 (a) and (c)** give the distinguished diffraction rings observed from the selected area electron diffraction (SAED) patterns indexed as ($\bar{1}$11), ($\bar{1}$02), ($\bar{1}$21) and ($\bar{2}$13) of $P2_1/c$ and (111), (200, (220) and (311) of $Fm\bar{3}m$. High resolution TEM shows the interplanar spacing (*d*) as ~0.28 and ~0.308 nm which corresponds to (200) and (111) of $P2_1/c$ and $Fm\bar{3}m$, respectively as depicted in **figure 3.7 (b) and (d)**.

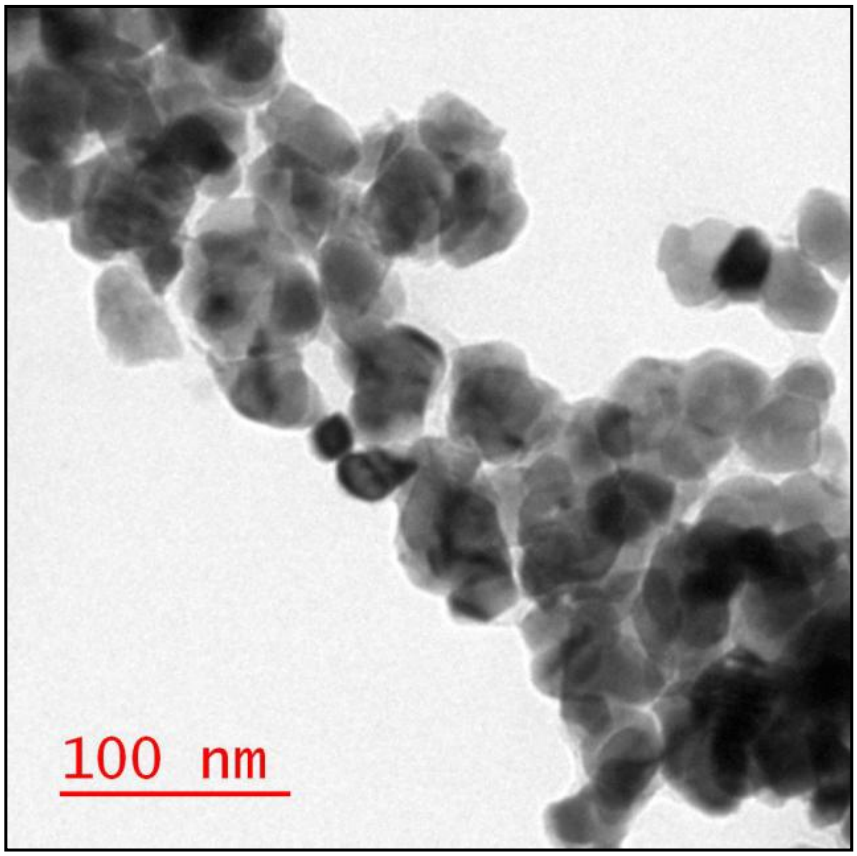


***Figure 3.6*** *Typical TEM micrograph of pure $HfO_2$ nanoparticles calcined at 900 $^oC$.*

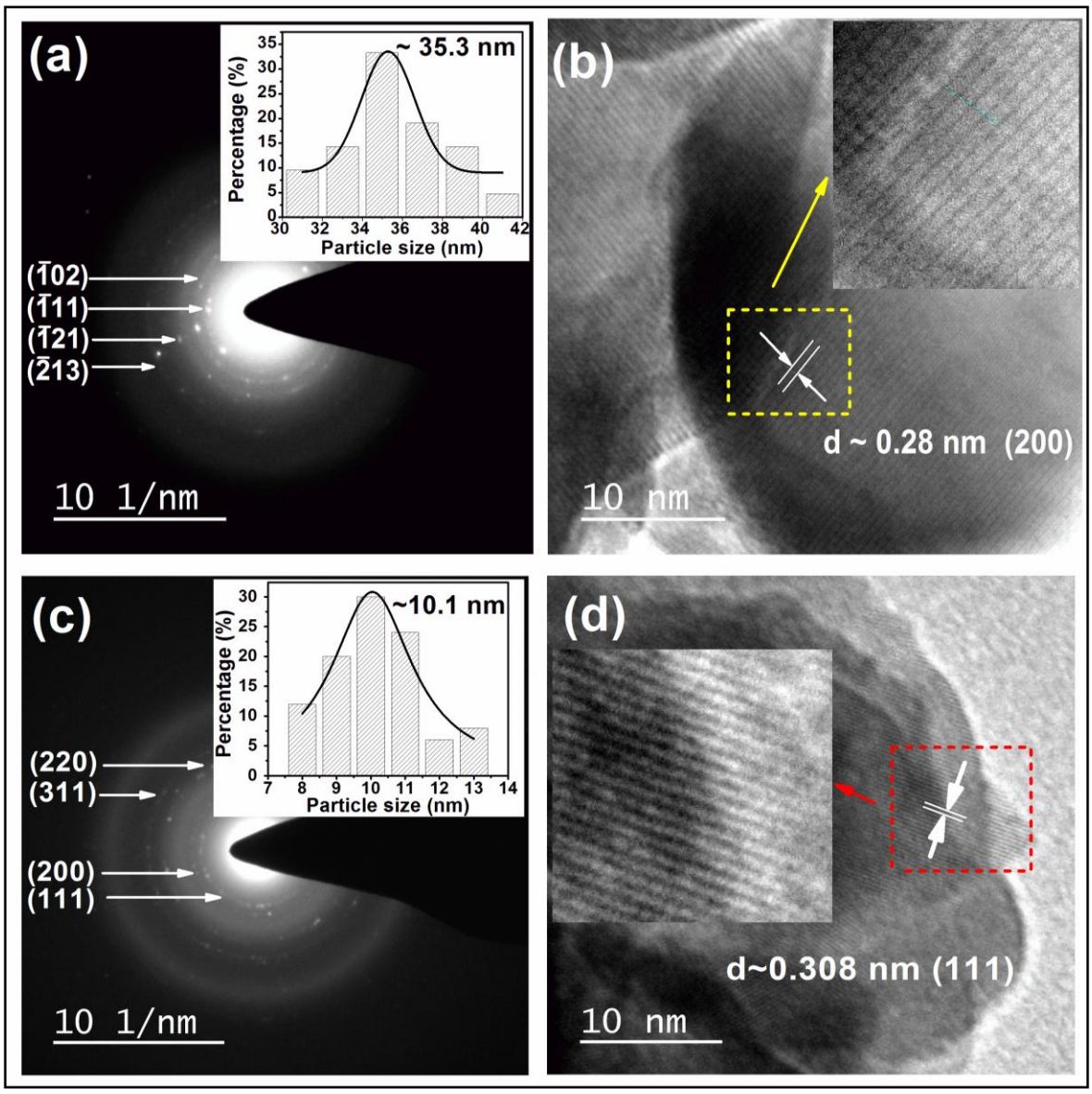


***Figure 3.7*** *SAED pattern and high resolution TEM for x = 0* ***(a and b)*** *and x = 0.11* ***(c and d),*** *respectively. Insets of* ***(a)*** *and* ***(c)*** *show the particle size distribution histogram. Insets of* ***(b)*** *and* ***(d)*** *show the lattice planes.*

### 3.2.4 Mechanism for Monoclinic to Cubic Phase Transformation

It is known in literature that bulk $HfO_2$ exists in polymorphs such as monoclinic phase at room temperature, tetragonal and cubic phases at around ~1700 and ~2600 $^{o}$C, respectively. It has been reported earlier that the high temperature phases of $HfO_2$ can be

stabilized at room temperature effectively by various dopants like Mn, Ce, Lu and Y etc. of different chemical valancies.[54, 109-111] For example, Dohčević-Mitrović *et al*. demonstrate the complete stabilization of pure cubic phase in $HfO_2$ by doping 15% of trivalent yttrium by metathesis synthesis.[66] Gálvez-Barboza *et al.,* through simple modified sol-gel method, obtain the pure cubic phase of $HfO_2$ nanoparticles after doping with 10% of trivalent Ce.[55] Mendoza-Mendoza *et al.* also report successful stabilization of the cubic phase by doping 10 mol% of Ce at a lower temperature through a molten LiCl/KCl chloride flux method.[110] On the other hand, Gao *et al.* report a fully stabilized cubic phase after doping with multi-valent Mn in $HfO_2$ nanoparticles by conventional solid state reaction method.[109] It has been shown that doping with 30% of Mn in $HfO_2$ and sintering in an argon atmosphere, the transformation from $Mn^{4+}$ to $Mn^{2+}$ takes place that stabilizes the cubic phase. However, sintering at 1000 $^{o}$C in the air, impurity phases of $Mn_2O_3$ and MnO are observed for more than 30% of Mn.[109] Furthermore, such high temperature cubic phase has not only been stabilized in $HfO_2$ but also in a similar system like $ZrO_2$. The key factors are the incorporation of dopants associated with the lattice expansion and consequent formation of oxygen vacancies. Therefore, the phase transformation from monoclinic to cubic in Dy doped $HfO_2$ could be explained in the light of stabilization process of doped $ZrO_2$ system.[112] It is a general agreement and is well accepted in literature that binary oxides are more prone to oxygen defects and to sample non-stoichiometry.[113, 114] Theoretically, Zhang *et al.*, through first principle calculation predicts that a divalent or trivalent cation substituting $Hf^{4+}$ ion induces oxygen vacancies ($V_o$) in the host lattice to maintain the overall charge neutrality. These dopants lower the required formation energy to introduce an oxygen vacancy in the host lattice.[115] The low

temperature monoclinic phase possesses seven coordinated $Hf^{4+}$ ions, whereas the high temperature tetragonal or cubic phase is coordinated by eight $Hf^{4+}$ ions. Therefore, it is expected in the present case that addition of $Dy^{3+}$ ions in $HfO_2$ lattice may also generate oxygen vacancies which vary with an increase in Dy concentration.

### 3.2.5 X-ray Photoelectron Spectroscopy (XPS)

XPS spectra for O 1*s* core level are shown in **figure 3.8** for x = 0 and 0.11. All the peaks are calibrated with respect to the C 1*s* peak located at ~284.6 eV. Due to the asymmetric shape of the spectra, we have deconvoluted the spectra into three peaks fitted with mixed Gaussian and Lorentzian functions using XPSPEAK version 4.1. The three curves centering at around 530.05, 531.1 and 533.0 eV are labeled as peak 1, 2 and 3, respectively. The peak with lower binding energy (BE) at 530.05 eV is associated with the oxygen atom in O—$Hf^{4+}$ bond.[66] The higher BE peak at 531.1 eV belongs to $O^{2-}$ ions in oxygen deficient regions in $HfO_2$ whereas peak at 533.0 eV originates partly from the hydroxyl groups and from the chemisorbed oxygen lying on the surface of the samples.[66, 116]

After deconvolution of each peak, due to the less pronounced peak corresponding to 533.0 eV in the spectra, we have ignored the area of the same peak. Comparing the peak area ratio of 2 and 1 ($A_2/A_1$), we observe that $A_2/A_1$ ratio is almost double in the cubic phase than in the monoclinic one. We, therefore, confirm that due to higher oxygen vacancies in x = 0.11, the high temperature cubic phase of $HfO_2$ is stabilized at room temperature. At the lowest concentration of Dy, $HfO_2$ shows only the monoclinic phase due to the insufficient amount of oxygen vacancy. With further increase in Dy concentration, the formation energy of oxygen vacancy is reduced significantly because of dipole formation between

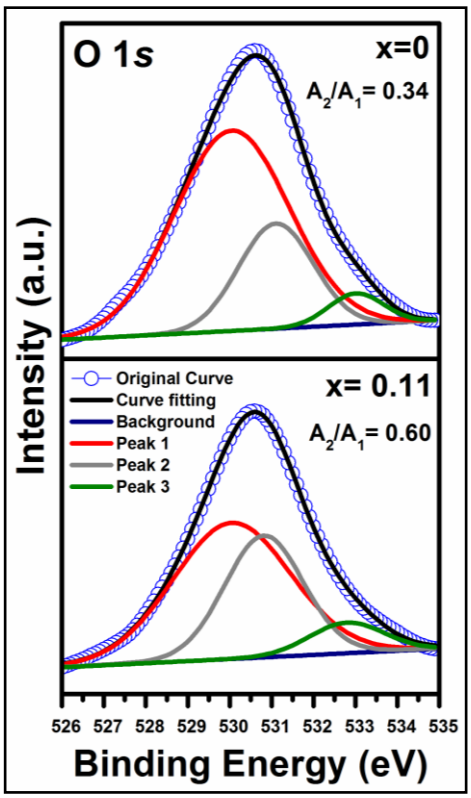


***Figure 3.8*** *The XPS spectra of O 1s region for x = 0 and x=0.11.*

Dy and $V_o$, introducing more oxygen vacancies in the lattice and hence, the monoclinic and cubic phases coexist for intermediate Dy concentrations (x = 0.05 - 0.07). Almost pure cubic phase is observed when Dy concentration approaches 9 at%. Eventually, at x = 0.11, a nominal concentration of oxygen vacancies is present that is sufficient enough to stabilize the cubic phase. Interestingly, one may notice that for dopants such as Y, Dy and Ce with ionic radii 1.019 Å, 1.027 Å and 1.143 Å, respectively i.e. more than $Hf^{4+}$ and also more than 1.00 Å, need a lower concentration of dopants to stabilize the cubic phase at room temperature. On the other hand, a relatively much higher concentration of dopants is needed when the ionic radii of dopants like $Mn^{2+}$ (0.96 Å) are slightly higher than $Hf^{4+}$ but less than 1.00 Å. When the ionic radius (0.67 Å) of $Mn^{4+}$ is quite less than the radius of $Hf^{4+}$, no cubic phase is observed even increasing the sintering temperature up to 1400 $^{o}$C in

the air.[109] Further, it is known that the oxygen vacancies are present in different charge states such as $V_o^{0}$, $V_o^{+}$ and $V_o^{++}$ etc. Due to filled defects states, $V_o^{0}$ does not essentially change the coordination number of Hf atoms and hence the relative phase stability. On the other hand, $V_o^{++}$ is more efficient in reducing the relative energies of cubic phase of $HfO_2$ with respect to the monoclinic one. Therefore, after incorporating a sufficient amount of Dy in $HfO_2$, the charged oxygen vacancies associated to 7-fold coordinated $Hf^{4+}$ ions around the defect site eventually result into 8-fold oxygen coordination with $Dy^{3+}$ ion thereby stabilizing the cubic phase of $HfO_2$ at room temperature. The above observations clearly indicate that the enhancement in lattice volume and nominal oxygen vacancies are needed to stabilize the cubic phase at room temperature with low dopant concentration.

### 3.2.6 Magnetic Properties

The magnetization (*M*) as a function of magnetic field (*H*) at 300 K for pure $HfO_2$ (x = 0) calcined at 500, 700 and 900 $^{o}$C are measured (**figure 3.9**). Sample calcined at 500 $^{o}$C exhibits a slim hysteresis loop at the lower magnetic field and at higher field, a linear increase in magnetization is observed. With increasing calcination temperature to 900 $^{o}$C, besides a linear increase in magnetization, the area under the hysteresis loop increases. The presence of noticeable hysteresis loop with low coercivity and remanence demonstrates a weak ferromagnetic behavior at room temperature induced primarily due to lattice defects. While coercivity ($H_c$) of ~45 Oe remains same in the sample calcined at 700 and 900 $^{o}$C, the remanence ($M_r$) is enhanced by an order of magnitude in sample calcined at 900 $^{o}$C. The observed $H_c$ is comparable to $H_c$ in $HfO_2$ reported by Coey *et al*.[117] In addition, it is worth noting that the maximum magnetization ($M_{max}$) decreases in sequence with

increasing calcination temperature. The reduction in $M_{max}$ is attributed to decrease in the surface to volume ratio.

Due to an appreciable hysteresis loop observed in sample calcined at 900 $^{o}$C, we have measured M vs. H at 2 and 35 K shown in **figure 3.10**. It is evident that the area under the hysteresis loop dramatically increases with decrease in measurement temperature as expected. At 2 K, while $H_c$ is ~650 Oe, at room temperature, it drastically falls to ~45 Oe

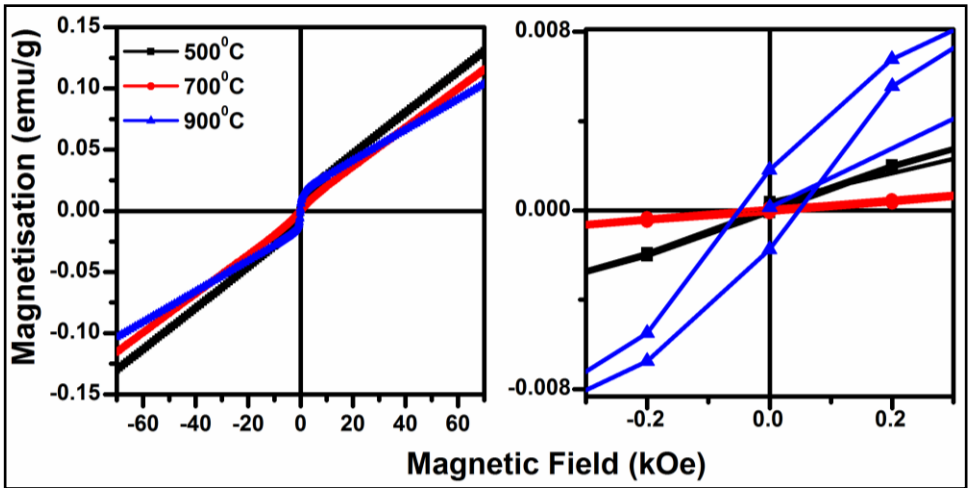


***Figure 3.9*** *Room temperature M vs.H curves for pure $HfO_2$ calcined at 500, 700 and 900 $^{o}$C. The right panel shows hysteresis at low magnetic field.*

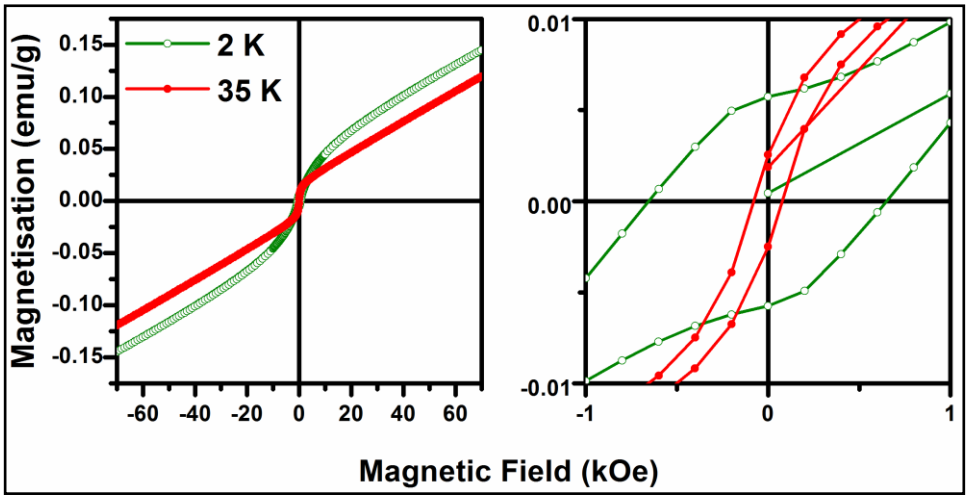


***Figure 3.10*** *M vs. H curves at 2 and 35 K for pure $HfO_2$ calcined at 900 $^{o}$C.*

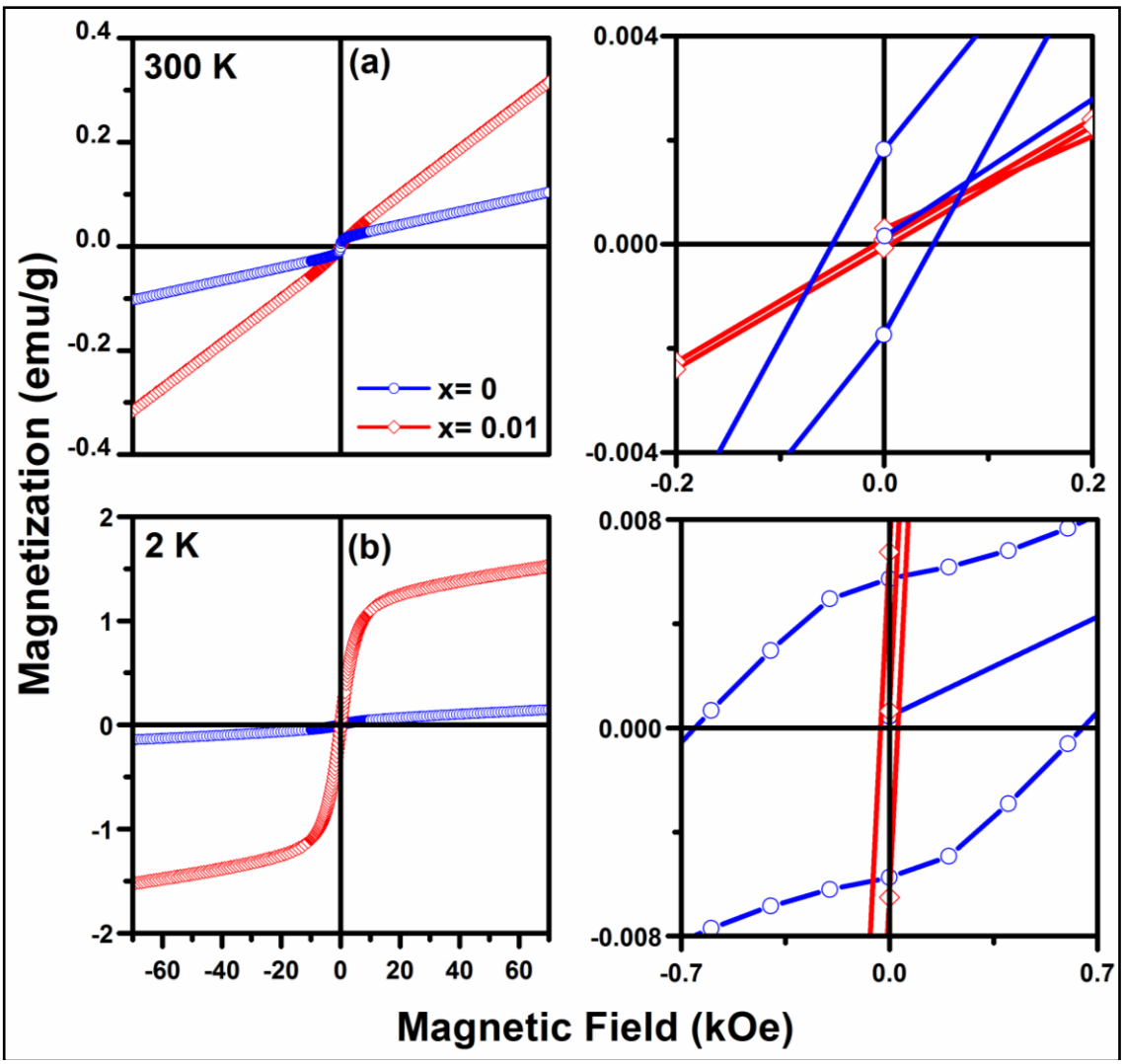


***Figure 3.11*** *M vs. H dependence measured at* ***(a)*** *300 K and* ***(b)*** *2 K for* $Hf_{1-x}Dy_xO_2$ *(x= 0 and 0.01). The right panel shows a zoomed-in view at lower field for x = 0 and 0.01.*

which is an order magnitude less. This indicates that ferro or ferrimagnetic ordering exist even at room temperature, which becomes more prominent at low temperature. Such a behavior is consistent with earlier reports on the colloidal $HfO_2$ nanorods, CaO nanopowders and $CeO_2$ powders.[118-120] While $M_{max}$ enhances by 30% at 2 K, $M_r$ increases from ~0.002 to ~0.006 emu/g with decreasing temperature from 300 to 2 K.

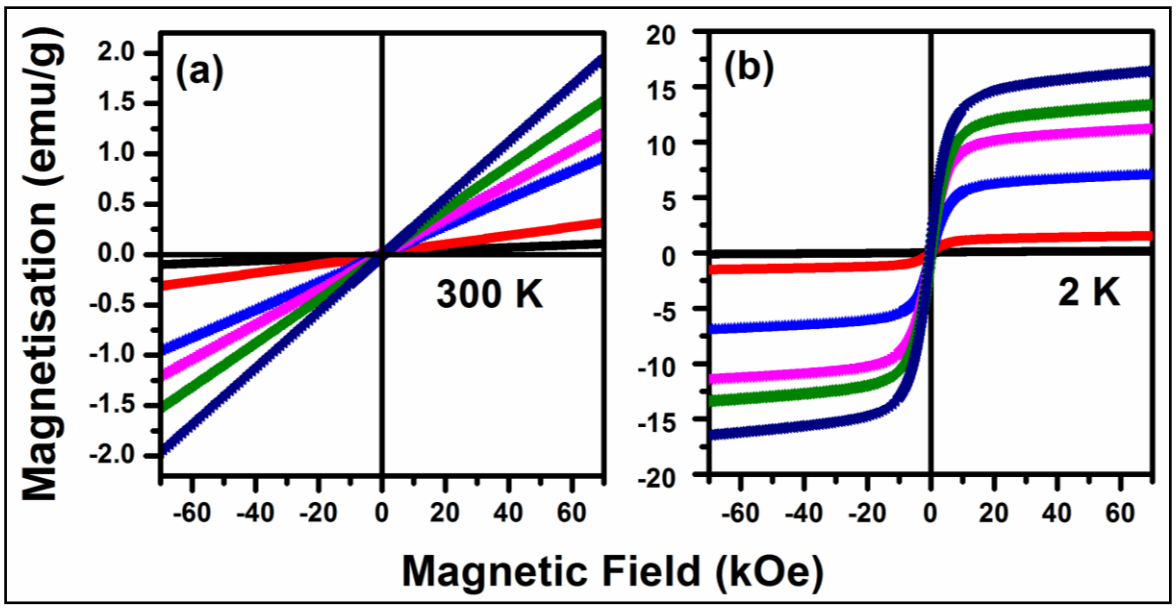


***Figure 3.12*** *M vs. H dependence measured at* ***(a)*** *300 K and* ***(b)*** *2 K for* $Hf_{1-x}Dy_xO_2$ *(x= 0-0.11).*

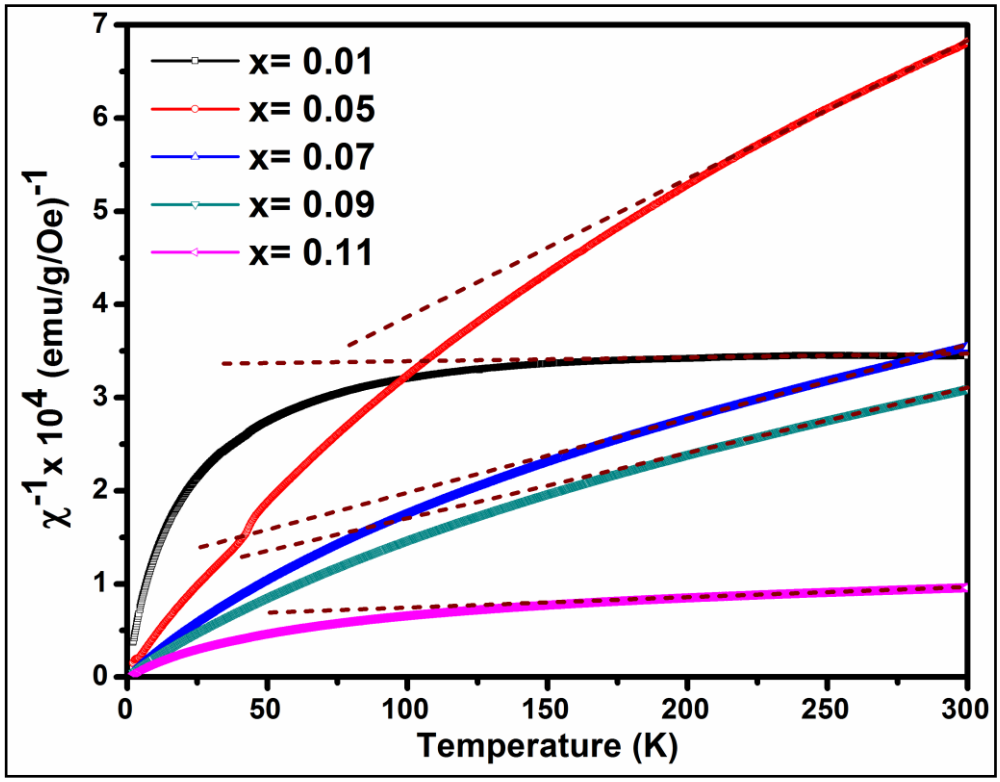


***Figure 3.13*** *Variation of* $\chi^{-1}$ *vs. T for* $Hf_{1-x}Dy_xO_2$ $(0.01 \leq x \leq 0.11)$.

Varying Dy concentration from 0 to 1 at% in $HfO_2$, we have shown M vs. H at room temperature in **figure 3.11 (a)**. Magnetization linearly increases with increasing magnetic field indicating paramagnetic behavior irrespective of Dy concentration. A closer inspection at low magnetic field reveals that addition of even 1 at% of Dy leads to a collapse of the hysteresis loop. This indicates severe quenching of the weak ferro or ferrimagnetic ordering observed in pure $HfO_2$ by doping Dy. However, $M_{max}$ shows a proportional enhancement with increasing Dy concentration in $HfO_2$. On the other hand, at 2 K we observe well-saturated hysteresis loop for $Hf_{1-x}Dy_xO_2$ (x = 0 and 0.1) (**figure 3.11 (b)**). It is interesting to note that $H_c$ drastically reduces from ~650 to ~30 Oe by incorporating 1 at% of Dy and remains unchanged for above concentration of Dy. An almost constant $H_c$ value of ~25±5 Oe is observed for all samples having more than 1 at% of Dy concentration. Saturation magnetization ($M_s$) increases from 0.14 to 16.2 emu/g with increasing Dy concentration upto 11 at% (**figure 3.12**).

In order to confirm the ferro or ferrimagnetic nature in Dy doped $HfO_2$, we have extrapolated the high temperature regime in the Curie-Weiss plot which gives negative Curie-Weiss temperature depicted in **figure 3.13**. It suggests an antiferromagnetic (AFM) correlation at the low temperature. However, the presence of hysteresis loop at low temperature reflects the finite magnetic moment. Combining both experimental observations, we conclude that the non-compensated antiferromagnetically ordered spins results in a finite magnetic moment exhibiting a ferrimagnetic behavior at low temperature. Further, susceptibility measurements with varying temperature shown in **figure 3.14**, shows the transition from antiferro and/or ferrimagnetic to paramagnetic phase for x = 0,

0.05, 0.07 and 0.11. We show that while Néel temperature ($T_N$) for x = 0 is found to be 45.5 K, for x = 0.05, 0.07 and 0.11, $T_N$ decreases to 4.6, 2.8 and 2.5 K, respectively.

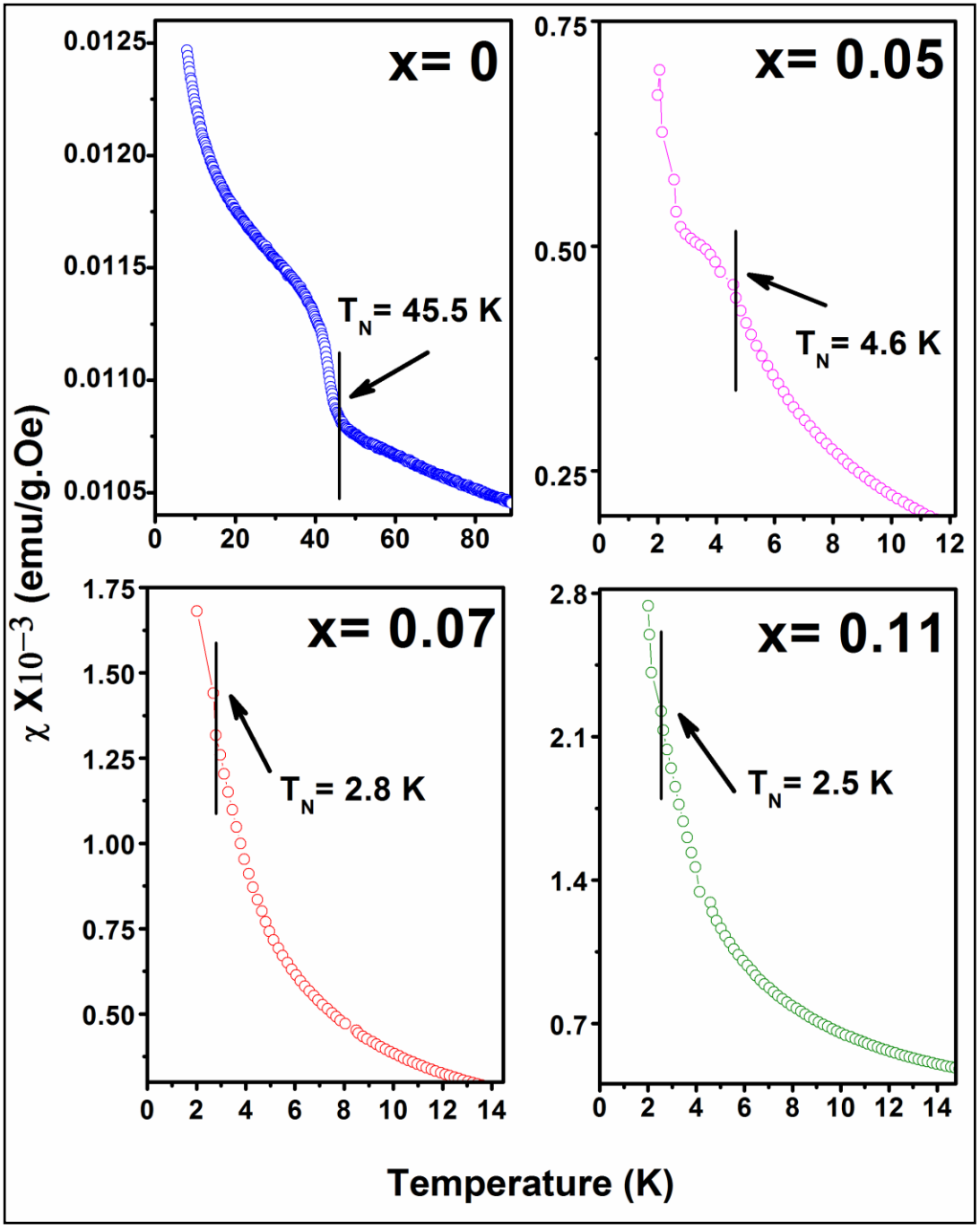


***Figure 3.14*** *Variation of susceptibility with temperature in $Hf_{1-x}Dy_xO_2$ (x = 0, 0.05, 0.07 and 0.11) nanoparticles.*

### 3.2.7 Origin of Room Temperature Ferromagnetism

It has been shown that RTFM in non-magnetic oxides like $TiO_2$, $HfO_2$, ZnO, $SnO_2$, $Al_2O_3$, MgO and $CeO_2$ is an inherent characteristic property of the nanostructured materials. The origin of such ferromagnetic ordering is likely due to various defects such as oxygen vacancies, F-centers, defect complexes etc and also depends on crystallinity, shape and morphology of the particles.[61, 77, 117, 119, 121-131] On the contrary to above reports, Lin *et al*. report the absence of ferromagnetic ordering in $HfO_2$ nanoclusters.[75] In this context, Dohčević-Mitrović *et al.* show that degradation of ferromagnetic ordering in Y doped $HfO_2$ could be due to various $(V_0{-}Y_{Hf})$ defect complexes in different charge states such as $(V_0{-}Y_{Hf})^0$, $(V_0{-}Y_{Hf})^+$ and $(V_0{-}Y_{Hf})^{++}$. Among them, $(V_0{-}Y_{Hf})^+$ is the most stable. Since these defects are usually located very near to the valence band, electrons could not be moved to 5*d* states to form the spin-split defect band to establish ferromagnetism.[66] On the other hand, in Pr doped $CeO_2$ nanoparticles, Paunović *et al.* believe that formation of $Pr^{3+}{-}V_0{-}Pr^{3+}$ or $Pr^{3+}{-}V_0{-}Ce^{3+}$ defect complexes are responsible for suppression of ferromagnetic ordering.[132] According to predictions using theoretical molecular mechanics method, generated oxygen vacancies mainly lie at the surface of nanoparticles that requires less energy to form an empty space corresponding to anions.[70] Also, oxygen vacancy at the surface is more efficient for mediating ferromagnetism than in the bulk.[131] These oxygen vacancies can exist in different charge states by electron trapping such as $V_0^{--}$, $V_0^{-}$, $V_0$, $V_0^{+}$ and $V_0^{++}$ forming defect band near the conduction band. It is well known that two electrons trapped in an oxygen vacancy called as $F^0$ centers are able to develop antiferromagnetic ordering while singly occupied vacancies ($F^+$ centers) establishes long range ferromagnetic ordering that lies deep in the impurity band gap. Also,

oxygen vacancies that are unoccupied known as $F^{++}$ centers do not contribute to ferromagnetic ordering.[72, 73]

In the present case, XPS analysis revealed that pure $HfO_2$ exhibiting monoclinic structure contains a considerable amount of oxygen vacancies at the surface of nanoparticles. We believe that these induced oxygen vacancies mediate ferromagnetic ordering via $F^{+}$ center exchange mechanism. The addition of $Dy^{3+}$ ion produces an oxygen vacancy ($V_0$) may bring two electrons in lattice to compensate charge neutrality which increases with increase in $Dy^{3+}$ concentration. In spite of a sufficient number of $V_0$, it is surprising that very small amount of substituted $Dy^{3+}$ ions destroy the weak ferromagnetism observed in pure $HfO_2$. In view of above reports and considering our experimental facts, it appears that quenching of ferromagnetic ordering in Dy doped $HfO_2$ could be either due to partial compensation of $F^{+}$ by $F^{0}$ and/or $F^{++}$ centers or because of defect states located far from the oxide conduction band minimum (CBM). However, it is obvious that substituted $Dy^{3+}$ ions for $Hf^{4+}$ ions in the lattice which are near to oxygen vacancy can create different kinds of unwanted complexes. In Dy doped $HfO_2$, a similar defect state of $Dy^{3+}$─$V_0$─$Dy^{3+}$ type can also be possibly formed which basically creates oxygen vacancies with no trapped electrons ($F^{++}$ centers). The abundant formation of $F^{++}$ centers negates long range ferromagnetic ordering and partially reduces the number of $F^{+}$ centers that hinders the appearance of ferromagnetism. On the other hand, defect complex formation can also displace the single electron energy levels of $V_0$ near or far from valence band maximum that prevents spin-splitting of defect bands developing ferromagnetism.[66, 133] Therefore, presence of $Dy^{3+}$ ions in the $HfO_2$ lattice can cause a reverse effect leading to the manifestation of the ferromagnetic ordering in Dy doped $HfO_2$ system.

### 3.2.8 Photoluminescence Properties

**Figure 3.15** depicts the room temperature excitation spectra recorded under emission wavelength of 490 nm for pure and Dy doped $HfO_2$ nanoparticles. In sample x = 0, the spectrum consists of a broad band in the range of 240 to 340 nm centered at ~296 nm and an another peak centered at ~398 nm. The former peak is attributed to the host absorption band.[54] The latter could originate from the most common defect state such as oxygen vacancies inherent in $HfO_2$. In x = 0.01, along with a host absorption peak at ~296 nm, the most intense peak is observed at 352 nm resulting from the electronic transition from the ground state, $^6H_{15/2}$ to hypersensitive, $^6P_{7/2}$. In addition, sharper secondary peaks are observed in the range of 300-410 nm. These peaks detected at around 326, 338, 366, 383 and 393 nm are ascribed to different f-f transitions of $Dy^{3+}$ ions from the ground state, such as $^6H_{15/2} \rightarrow {}^6P_{3/2}$, $^6H_{15/2} \rightarrow {}^4F_{5/2}/{}^4I_{9/2}$, $^6H_{15/2} \rightarrow {}^6P_{5/2}$,$^6H_{15/2} \rightarrow {}^4F_{7/2}$, and $^6H_{15/2} \rightarrow {}^4I_{13/2}$, respectively.[134, 135] The presence of host absorption peak at ~296 nm indicates a weak energy transfer from the host to $Dy^{3+}$ activator ions. Further, the intensity of these excitation peaks decreases with increasing Dy concentration and finally reaches a minimum when x = 0.11. The appearance of sharp absorption peaks after doping 1 at% of Dy occurs at the expense of host absorption band of $HfO_2$ lattice.

The emission spectra of $Hf_{1-x}Dy_xO_2$ ($0 \leq x \leq 0.11$) nanoparticles are collected after exciting with 352 nm which is the highest intensity excitation peak shown in **figure 3.16**. In x = 0, two emission peaks at 413 and 435 nm are superimposed and show a broad band in the range of 380-500 nm. These peaks are ascribed to the emissions of the host lattice. In addition to these peaks, for x = 0.01, two more emission peaks are observed at 490 and 577 nm falling in the blue and yellow region, respectively.

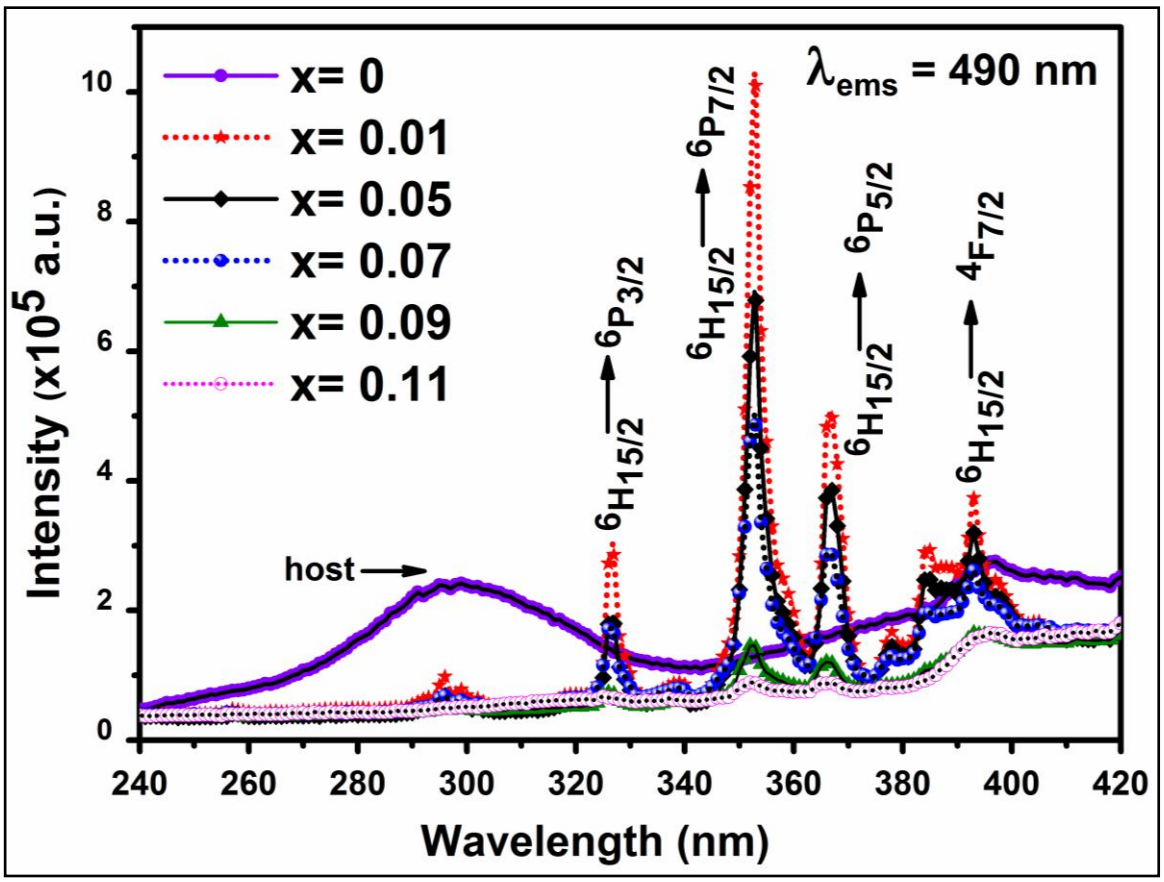


***Figure 3.15*** *Room temperature excitation spectra of* $Hf_{1-x}Dy_xO_2 (0 \leq x \leq 0.11)$ *by monitoring the emission wavelength at 490 nm.*

These peaks are the consequence of transitions from the metastable state to ground states such as $^4F_{9/2} \rightarrow {}^6H_{15/2}$ and $^4F_{9/2} \rightarrow {}^6H_{13/2}$.[135, 136] With increasing Dy concentration, the emission peak intensity decreases gradually up to 7 at% and further at x = 0.09 and 0.11, the peak intensity is drastically reduced. Moreover, we observe the most efficient emission behavior when we dope only 1 at% of Dy in $HfO_2$.

It is well-known that emission from the electronic transition, $^4F_{9/2} \rightarrow {}^6H_{13/2}$ of the $Dy^{3+}$ ion observed in yellow (Y) region is hypersensitive to the crystal field environment. In a site without inversion symmetry, usually, this transition becomes the dominant one.[137] The other strongest emission peak corresponding to the magnetic transition, $^4F_{9/2}$

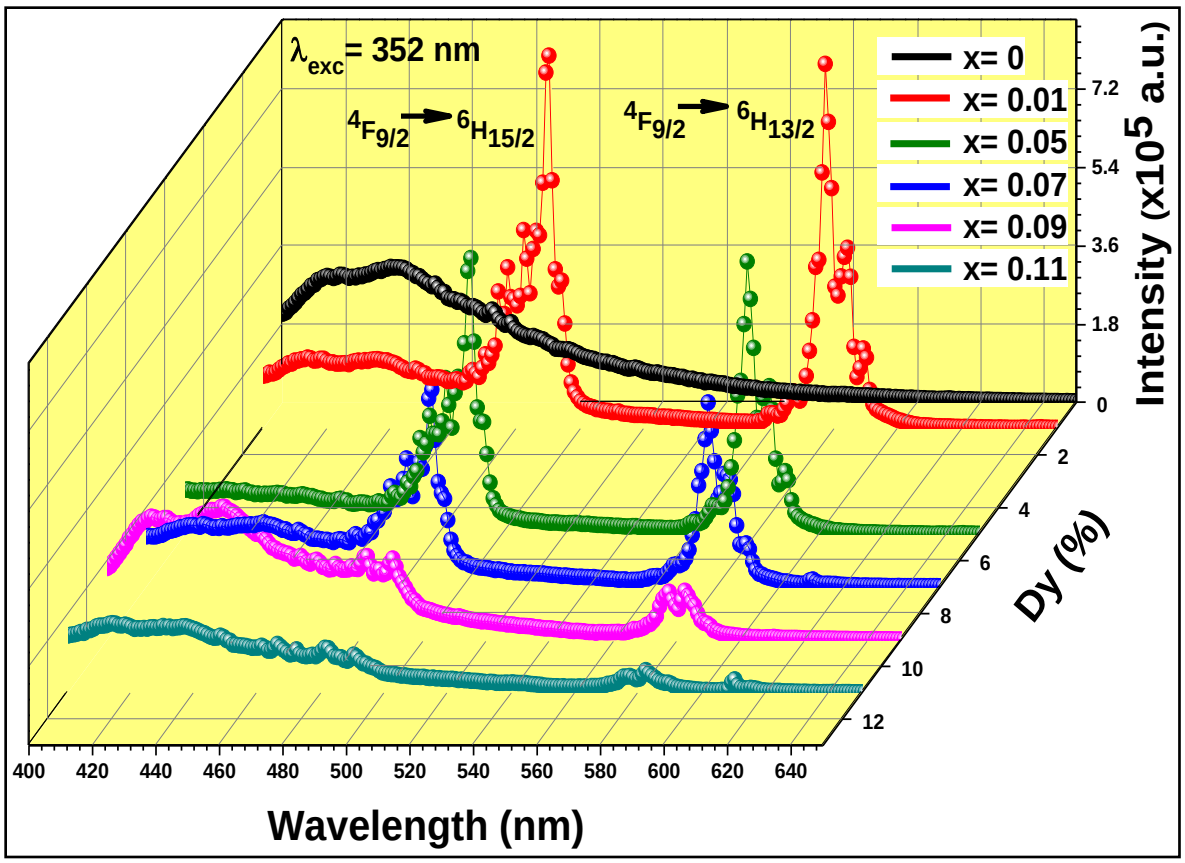


***Figure 3.16*** *Room temperature emission spectra of $Hf_{1-x}Dy_xO_2$ ($0 \leq x \leq 0.11$) at an excitation wavelength of 352 nm.*

$\rightarrow {}^6H_{15/2}$ detected in blue (B) region bears the information of the presence of $Dy^{3+}$ ions at a low symmetry site with inversion symmetry. Taking the intensity ratio of electronic to magnetic transition shown in equation (2) gives the indication of the local symmetry of $Dy^{3+}$ ion site.

$$\frac{Yellow\ (Y)}{Blue\ (B)} = \frac{I({}^4F_{9/2} \rightarrow {}^6H_{13/2})}{I({}^4F_{9/2} \rightarrow {}^6H_{15/2})} \qquad (2)$$

The estimated Y-B ratio decreases with increasing Dy concentration as shown in **figure 3.17 (a)** (blue line). One can notice that Y-B ratio found to be 0.95±0.03 at a lower Dy concentration and remains constant upto x = 0.07. However, at a higher Dy concentration,

i.e. at x = 0.09 and 0.11, the Y-B ratio reduces more rapidly, suggesting that the intensity of electronic transition decreases faster than that of the magnetic one.[73] The reduction in Y-B ratio above 7 at% of Dy concentration could be due to the changes in the local symmetry of $Dy^{3+}$ ions in $HfO_2$ lattice. It is evident from XRD analysis that while a high symmetry cubic phase obtained in x = 0.09 and 0.11, at x = 0.01-0.07, the low symmetry monoclinic phase remains present in the parent $HfO_2$ lattice.

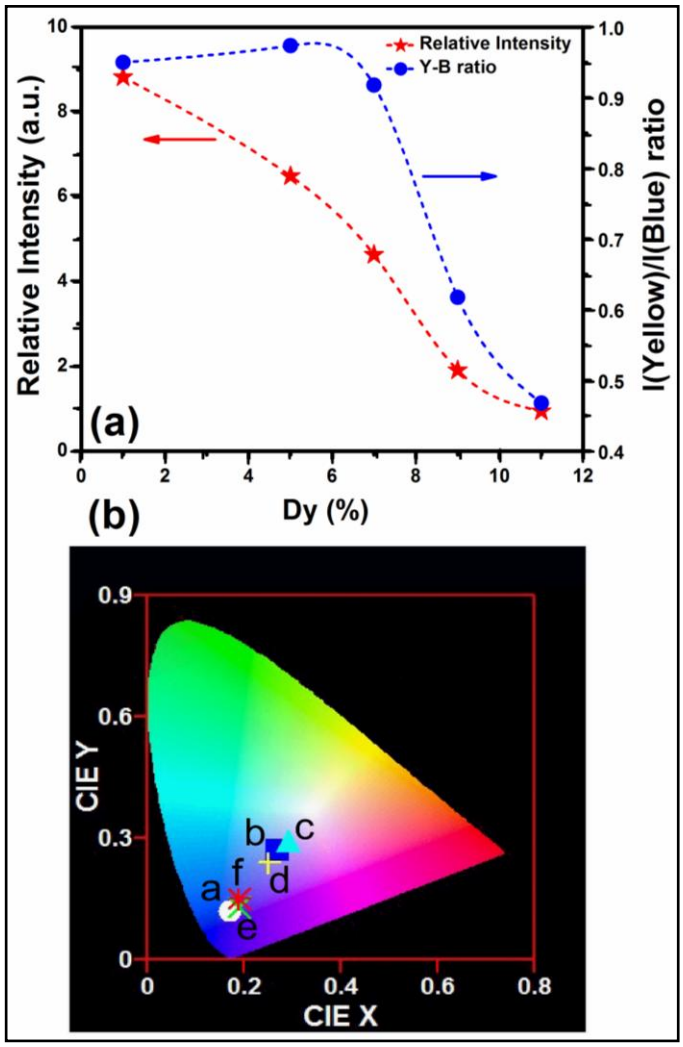


***Figure 3.17 (a)*** *Dependence of Y–B ratio and the relative intensity of the 490 nm emission peak in* $Hf_{1-x}Dy_xO_2$ *(*$0 \leq x \leq 0.11$*) and* ***(b)*** *the CIE colour space chromaticity diagram (****a–f*** *corresponds to x = 0-0.11) under an excitation wavelength of 352 nm.*

The low symmetry in x = 0.01 and a high symmetry in x = 0.11 realized from XRD well supports the luminescence behavior as observed in the present case. **Figure 3.17 (a)** (red line) depicts the variation of relative intensity of emission peak at 490 nm as a function of Dy concentration in $HfO_2$ nanoparticles. The emission intensity decreases rapidly with increasing Dy concentration in $HfO_2$. Such a behavior clearly indicates the quenching of luminescence taking place due to increase in Dy concentration. At a higher Dy concentration, this can be best explained in terms of the cross relaxation between two closely situated $Dy^{3+}$–$Dy^{3+}$ ions that includes mainly transition $Dy^{3+}$ ($^4F_{9/2}$) + $Dy^{3+}$ ($^6H_{15/2}$) → $Dy^{3+}$ ($^6F_{3/2}$) + $Dy^{3+}$ ($^6H_{11/2}$). Due to less separation between $Dy^{3+}$ ions, the electrons move from a high energy level, $^4F_{9/2}$ to $^6F_{3/2}$ a lower energy level.[136-138] The energy associated with such transition helps electrons sitting in the ground state of $Dy^{3+}$ activator ions to get transferred to a higher energy level, $^6H_{11/2}$. Such observation suggests that excellent photoluminescence properties can be perceived by doping a nominal amount of Dy (1 at%) in $HfO_2$. **Figure 3.17 (b)**depicts two dimensional (x,y) CIE color space chromaticity diagram for $HfO_2$ nanoparticles doped with varying Dy concentration under an excitation of 352 nm. The CIE chromaticity coordinates are found to be (0.17, 0.12), (0.27, 0.27), (0.29, 0.29), (0.25, 0.24), (0.19, 0.13) and (0.19, 0.15) for x = 0, 0.01, 0.05, 0.07, 0.09 and 0.11, respectively. Among all samples, the color coordinates of x = 0.01, 0.05 and 0.07 are close to that of the cool white emission having the highest Y-B ratio. This indicates that by adjusting the Y-B ratio, one can also realize white light emission in Dy doped $HfO_2$ system for white LED (WLED) and display application.

### 3.2.9 Energy Band Diagram

We have proposed an energy band diagram to illustrate the different energetic transitions involved in Dy doped $HfO_2$ system as shown in **figure 3.18**. We have labeled

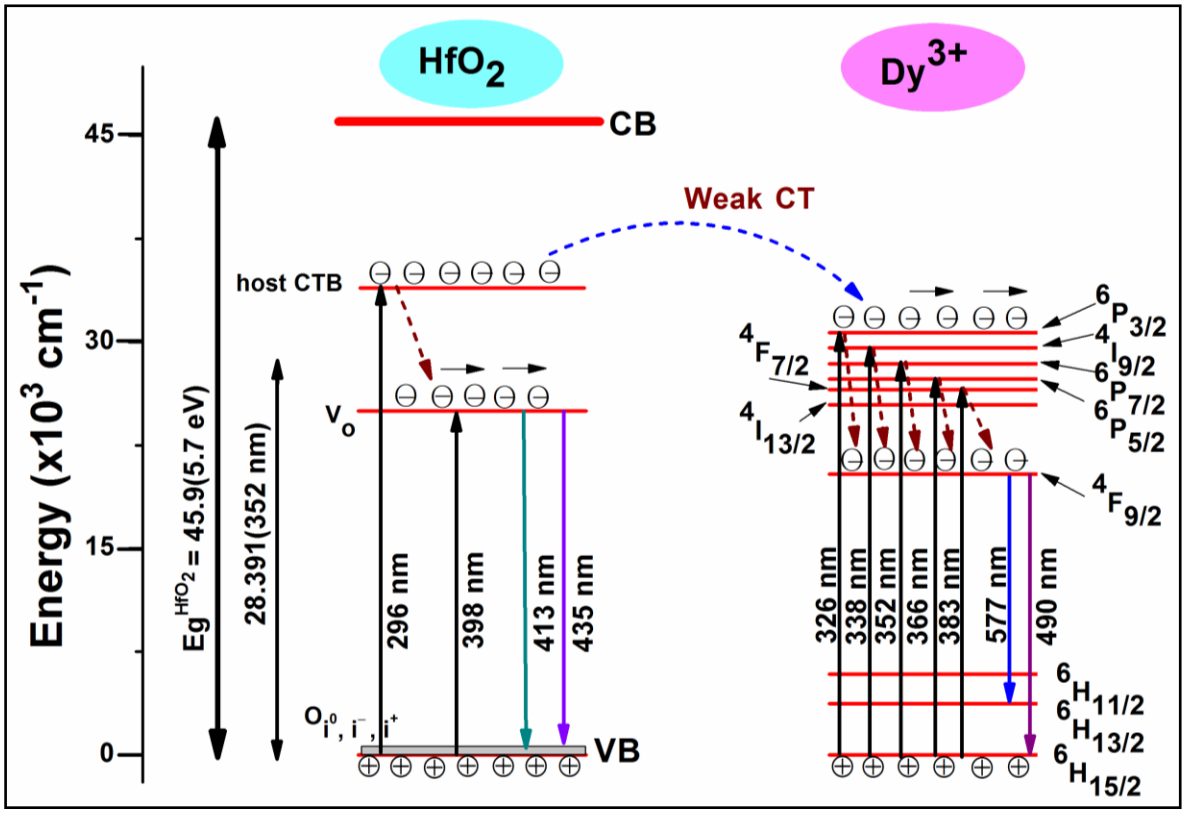


***Figure 3.18*** *The proposed energy band diagram illustrating the charge transfer (CT) mechanism taking place in* $Hf_{1-x}Dy_xO_2$.

the energy levels associated with the excitation and emission of $Dy^{3+}$ ions ($^6H_{11/2}$, $^6H_{13/2}$, $^6H_{15/2}$, $^4F_{9/2}$, $^4I_{13/2}$, $^4F_{7/2}$, $^6P_{5/2}$, $^6P_{7/2}$, $^6P_{3/2}$ and $^4I_{9/2}$) and the host lattice ($V_o$, $O_i^o$, $O_i^-$ and $O_i^+$ ). The host $HfO_2$ (donor) partially absorbs the pumping energy and the electrons are promoted either to the host charge transfer band (CTB) and/or to the inherent defect states ($V_o$) lying within the band gap of the host observed at ~296 and 398 nm in the excitation spectrum.

Consequently, the excited electrons relax from energy levels of the host CTB and from $V_o$ defect states to the ground state through deep defect levels lying near to the valence band of the host showing emissions at ~413 and 435 nm and/or is partially transferred from the host CTB to different energy levels of the $Dy^{3+}$ ion. The slight overlapping of $HfO_2$ broadband emission with Dy doped $HfO_2$ excitation band confirms the weak charge transfer from the host CTB to $Dy^{3+}$ activator (acceptor) ions. The similar emission profiles of the host suggest that the energy transfer process could be non-radiative.[139] Such charge transfers from the host CTB to an activator ion ($Sm^{3+}$ ions) have been shown by De la Rosa-Cruz *et al*. in Sm doped $ZrO_2$.[140] The electrons in the excited levels of $Dy^{3+}$ ion relax to different ground states such as $^6H_{13/2}$ and $^6H_{15/2}$ through metastable state, $^4F_{9/2}$ showing emissions at 490 and 577 nm.

## 3.3 Conclusions

In this chapter, $HfO_2$ and Dy doped $HfO_2$ synthesized through simple Pechini type sol-gel method were thoroughly studied for structure, magnetic and photoluminescence properties. We demonstrated that the monoclinic phase of $HfO_2$ nanoparticles transforms partially to cubic phase after incorporating Dy of 5 at%. Further increasing Dy (x = 0.07-0.11) concentration, the cubic phase enhanced at the expense of monoclinic one. At x = 0.11, the monoclinic phase completely transformed to cubic phase. We could able to stabilize the high temperature cubic phase of $HfO_2$ at room temperature after incorporating Dy. Selected area electron diffraction patterns confirmed the monoclinic and cubic phase in $HfO_2$ and $Hf_{0.89}Dy_{0.11}O_2$, respectively. High resolution TEM showed interplanar spacing of ~0.28 and ~0.308 nm corresponding to (200) and (111) of $P2_1/c$ and $Fm\bar{3}m$, respectively. A mechanism for stabilization of high temperature cubic phase in $Hf_{1-x}Dy_xO_2$ was proposed

where role of the substitution effect of Dy and the formation of oxygen vacancies was discussed. The magnetic properties of $HfO_2$ nanoparticles revealed the presence of hysteresis at room temperature indicating ferromagnetism in contrast to the diamagnetic behavior in bulk. Incorporation of even 1 at% of Dy quenched the ferromagnetic ordering. The disappearance of ferromagnetic behavior in Dy doped $HfO_2$ could be due to the formation of defect complex $Dy^{3+}$─$V_0$─$Dy^{3+}$ which mainly creates $F^{++}$ centers, highly unfavorable for long range ferromagnetic ordering. From the photoluminescence studies, we observed an excellent blue and yellow light emission by incorporating even 1 at% of Dy in $HfO_2$ lattice. The peak intensity of the blue and yellow emission decreased with increasing Dy concentration. The emissions of $Dy^{3+}$ ion were found to be partially accompanied by a non-radiative weak energy transfer from the host CTB to $Dy^{3+}$ activator ions. Combining all the photoluminescence properties, we proposed an energy band diagram showing different transitions occurring in $Hf_{1-x}Dy_xO_2$. Looking at the rich photoluminescence behavior of $Hf_{0.99}Dy_{0.01}O_2$, it may be used as an efficient phosphor material for scintillator application.

# Chapter 4

## 4.1 Introduction

In this chapter, we have studied the structural and photoluminescence properties of $HfO_2$ and Sm doped $HfO_2$ nanoparticles synthesized by a Pechini type sol-gel technique. $HfO_2$ nanoparticles showing monoclinic phase transforms to the high temperature cubic phase upon doping Sm upto 12 at% followed by a mixed phase of monoclinic and cubic at intermediate concentration (5-11 at%) of Sm. Photoluminescence studies of $HfO_2$ demonstrate different strong emission bands in the visible region after exciting with UV light. Under excitation with visible light, the characteristic emissions of $Sm^{3+}$ ion appear producing near green and red color light. A detailed phase transformation and photoluminescence behavior in Sm doped $HfO_2$ have been discussed.

## 4.2 Results and Discussion

### 4.2.1 Structure and Phase Transformation

X-ray diffraction (XRD) patterns of $Hf_{1-x}Sm_xO_2$ (x = 0-0.12) powders calcined at 900 $^oC$ in air are depicted in **figure 4.1(a)**.The XRD patterns show well distinguished, sharp diffraction peaks indicating crystalline nature of the particles. At x = 0, the observed diffraction peaks such as (011), (110), ($\bar{1}$11), (111), (020), (200), (021), ($\bar{2}$11) and (112) are indexed as the monoclinic phase of $HfO_2$ with space group, $P2_1/c$ (JCPDS card no. 78-0049). No secondary phase has been detected in the powders. While at x = 0.01, the diffraction peaks match well with the monoclinic phase, at $x \geq 0.05$, along with the diffraction peaks of the monoclinic phase, a weak peak at ~30.20$^o$ is appeared which corresponds to (111), the most intense peak of the cubic phase (JCPDS card no. 53-0560).

Further increase in Sm concentration, the intensity of (111) increases. At $0.09 \leq x \leq 0.11$, although the diffraction peaks corresponding to both monoclinic and cubic phase are present, the cubic phase fraction increases at the expense of monoclinic one. At x = 0.12, it is evident that all diffraction peaks such as (111), (002), (022), (113) and (222) correspond to the pure cubic phase, space group, $Fm\bar{3}m$ of $HfO_2$. Absence of any impurity phase confirms that $Sm^{3+}$ ions substitute $Hf^{4+}$ ions in both monoclinic and cubic lattice. We, for the first time, demonstrate that the incorporation of $Sm^{3+}$ ions into $HfO_2$ lattice stabilize the high temperature cubic phase of $HfO_2$ at room temperature. The phase transformation from monoclinic to cubic one with an increase in Sm concentration is accompanied with gradual change in phase fraction of monoclinic to cubic. We have estimated the phase fraction by taking the integral peak area ratio of (111) of cubic to (111) or ($\bar{1}$11) of monoclinic phase (**figure 4.1 (b)**). It is observed that the peak integral area ratio i.e. $A_{CP(111)}/A_{MP(111)}$ or $A_{MP(\bar{1}11)}$ increases with increase in Sm concentration. While a mixed phase of monoclinic and cubic exists at an intermediate Sm concentration (x = 0.05-0.11), the pure cubic phase of $HfO_2$ is observed at x = 0.12. The cubic phase of $HfO_2$ obtained after calcining at 900 $^oC$, could be stabilized at room temperature by doping Sm upto 12 at%.

Further, the structural refinements are carried out using the Le-Bail profile fitting of FULLPROF program with pseudo-Voigt function. Typical observed and simulated XRD patterns for x = 0 and 0.12 using $P2_1/c$ and $Fm\bar{3}m$ are shown in **figure 4.2**. The observed pattern, simulated data after fitting and the difference pattern between observed and simulated data are shown as dots, continuous line and as bottom line, respectively. The tick marks above the difference plot show the positions of the Bragg peak. All the peaks corresponding to $P2_1/c$ and $Fm\bar{3}m$ are matched with observed peak positions.

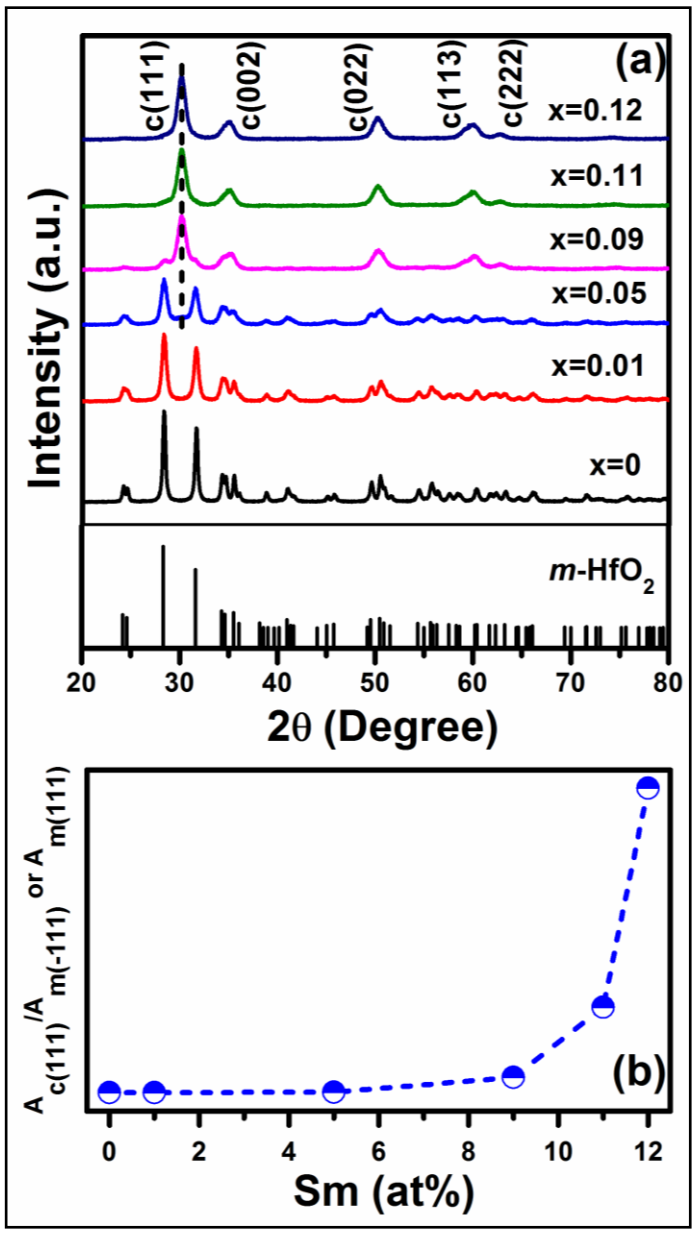


***Figure 4.1 (a)*** *X-ray diffraction patterns of* $Hf_{1-x}Sm_xO_2$ *(0 ≤x ≤0.12) powders calcined at 900 °C and* ***(b)*** *integral peak area ratio of (111) of cubic phase to (T11) or (111) of monoclinic phase as a function of Sm concentration.*

The volume and cell parameters derived from the refinements are tabulated in **Table 4.1**.While lattice parameters of the monoclinic phase does not show any significant change compared to the standard value, in the cubic phase, '*a*' increases from 5.095 to 5.134 Å.

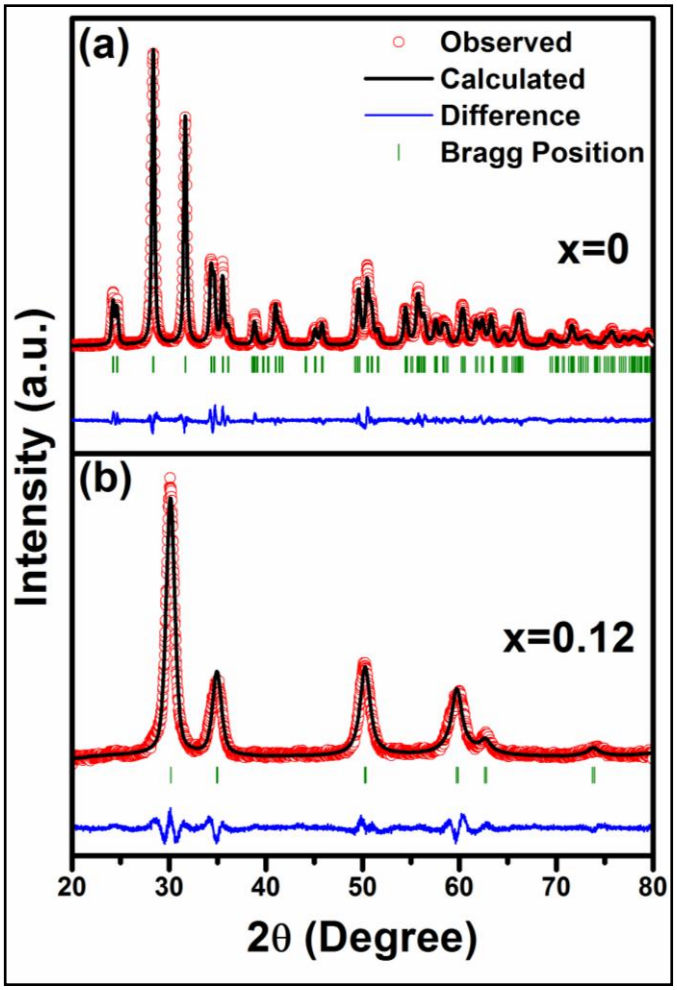


***Figure 4.2*** *Le-Bail profile fitting of $Hf_{1-x}Sm_xO_2$* ***(a)*** *x = 0 with $P2_1/c$ and* ***(b)*** *x = 0.12 with $Fm\bar{3}m$ space groups.*

| JCPDS card no./Sample | Structure | Space group | Cell parameters | | | |
|---|---|---|---|---|---|---|
| | | | a (Å) | b (Å) | c (Å) | Volume (Å$^3$) |
| 78-0049 | Monoclinic | $P2_1/c$ | 5.117 | 5.175 | 5.291 | 138.32 |
| 53-0560 | Cubic | $Fm\bar{3}m$ | 5.095 | 5.095 | 5.095 | 132.26 |
| $Hf_{1-x}Sm_xO_2$ (x=0) | Monoclinic | $P2_1/c$ | 5.117 | 5.176 | 5.290 | 138.30 |
| $Hf_{1-x}Sm_xO_2$ (x=0.12) | Cubic | $Fm\bar{3}m$ | 5.134 | 5.134 | 5.134 | 135.22 |

***Table 4.1*** *Refined cell parameters and cell volume for $Hf_{1-x}Sm_xO_2$ (x = 0 and 0.12) compared with standard JCPDS data for monoclinic and cubic phase of $HfO_2$*

Consequently, the cell volume of cubic phase shows an increment of 2.3%. The considerable enhancement in cell volume is in agreement with the increase in the ionic radius of $Sm^{3+}$ ion (1.079 Å) than that of $Hf^{4+}$ (0.83 Å) one. Such observation in Sm doped $HfO_2$ further endorses the substitution of $Sm^{3+}$ at $Hf^{4+}$sites in the lattice favoring the stabilization of the high temperature cubic phase of $HfO_2$ at room temperature. Because of significant difference in ionic radii i.e. ~0.25 Å, it is worth to examine strain in the lattice with an increase in Sm concentration. Therefore, we have examined the Williamson-Hall (W-H) plot using following expression where $\varepsilon$ is the lattice strain and $D$ is the crystallite size.[141]

$$\frac{\beta \mathrm{Cos}\,\theta}{\lambda} = \frac{\mathrm{k}}{\mathrm{D}} + \frac{4\varepsilon \mathrm{Sin}\,\theta}{\lambda} \qquad (1)$$

In this plot, $\beta\mathrm{Cos}\theta/\lambda$ is plotted as a function of $\mathrm{Sin}\theta/\lambda$ where $\theta$ is Bragg angle, $\lambda$ is the wavelength of X-ray, k is constant related to shape of particle and $\beta$ is full width at half maximum (FWHM in radians) taken after removing $K\alpha_2$ contribution and instrumental broadening effects. In case of pure particle size broadening, this plot is likely to be a straight line parallel to $4\mathrm{Sin}\theta/\lambda$ at x-axis, whereas it shows a non-zero slope in the presence of strain in the lattice.[142] The change in particle size and lattice strain as a function of Sm concentration is depicted in **figure 4.3**. It is observed that upto x = 0.09, XRD peak broadening is only due to the particle size. The particle size found to be ~35 nm at x = 0 reduces substantially to ~20 nm at x = 0.01. No significant change in particle size observed upto x = 0.09. At x > 0.09, while the lattice strain increases and is enhanced by two orders of magnitude at x = 0.12, particle size is reduces ~10 nm.

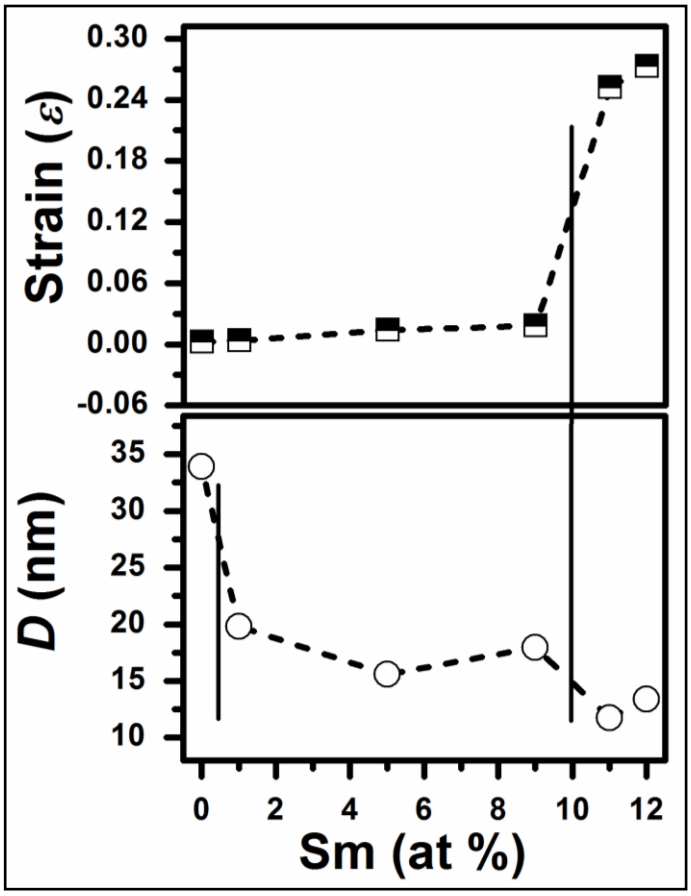


***Figure 4.3*** *Variation of crystallite size (D) and lattice strain (ε) in $Hf_{1-x}Sm_xO_2$ ($0 \leq x \leq 0.12$) obtained from Williamson-Hall plot.*

### 4.2.2 Microstructural Analysis

In order to further confirm the monoclinic and cubic phase, we have taken the selected area electron diffraction (SAED) pattern of $Hf_{1-x}Sm_xO_2$ (x = 0 and 0.12) as shown in **figure 4.4 (a) and (b)**. The well-defined diffraction rings in SAED are indexed as $(\bar{1}11)$, $(\bar{1}02)$, $(\bar{1}21)$ and $(\bar{2}13)$ of $P2_1/c$ and (111), (200), (220) and (311) of $Fm\bar{3}m$, respectively. The high resolution TEM images show different lattice planes in x=0 and 0.12 depicted in **figure 4.4 (c) and (d)**. The estimated interplanar spacing, as ~0.387 and 0.28 nm correspond to (011) and (111) of $P2_1/c$. The lattice planes with spacing of ~0.174 or ~0.206

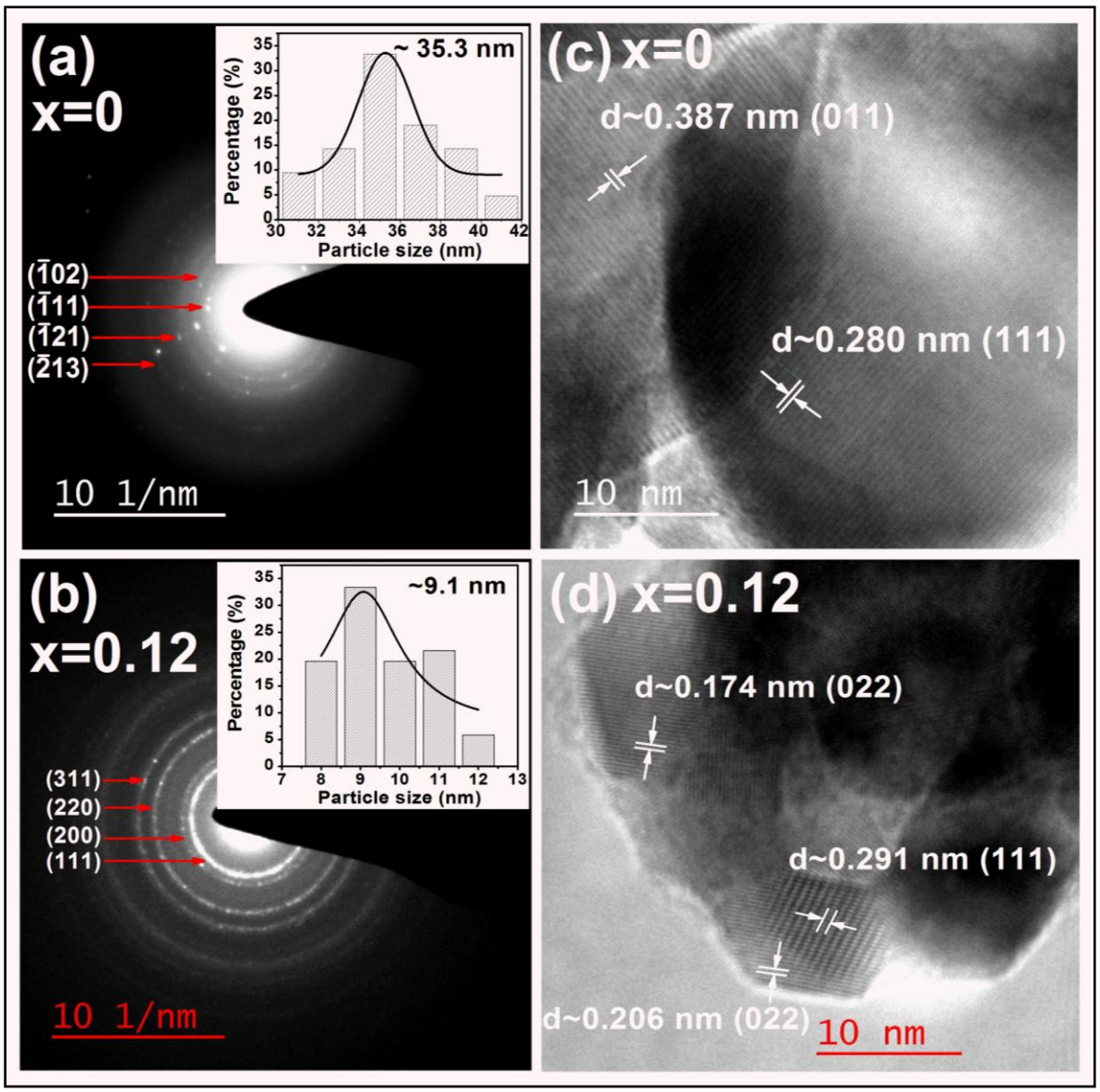


***Figure 4.4*** *SAED patterns of* ***(a)*** $HfO_2$ *and* ***(b)*** $Hf_{0.88}Sm_{0.12}O_2$ *and; High resolution TEM showing different lattice planes of* ***(c)*** $HfO_2$ *and* ***(d)*** $Hf_{0.88}Sm_{0.12}O_2$*. The particle size distribution histograms are shown as inset of* ***(a)*** *for* $HfO_2$ *and inset* ***(b)*** *for* $Hf_{0.88}Sm_{0.12}O_2$*.*

and ~0.291 nm are associated to (022) and (111) of $Fm\bar{3}m$. Transmission electron micrographs show that the particles are agglomerated and semi-spherical in shape (see **figure 3.6**). The particle size distribution histograms reveal that the average particle size is

found to be ~35 nm for x = 0 and ~9 nm for x = 0.12 (see insets of **figure 4.4 (a) and (b)**) which matches well with the average particle size calculated from W-H plot.

### 4.2.3 Mechanism for Monoclinic to Cubic Phase Transformation

Bulk $HfO_2$ possesses different polymorphs such as monoclinic, tetragonal and cubic phase. While monoclinic phase is stable at room temperature, $HfO_2$ undergoes a phase transition to the tetragonal and cubic phase at ~1700 and ~2600 $^oC$, respectively. According to previously reported literature, the stabilization of the high temperature cubic phase of $HfO_2$ at room temperature can be achieved by incorporating dopants such as Mn, Ce, Lu, Dy and Y with different charge states.[54, 109, 111, 143, 144] In this context, Gao *et al.* synthesized Mn doped $HfO_2$ nanoparticles through a solid state reaction method and demonstrate the stabilization of the cubic phase within a narrow composition range of 20-30% of Mn.[109] It has been revealed that the monoclinic to cubic phase transformation involves the combined effect of size of Mn ion and charge states. Gálvez-Barboza *et al.* have achieved the cubic phase in 10 wt% Ce doped $HfO_2$ synthesized by a modified sol-gel technique.[143] Mendoza-Mendoza *et al.* prepare pure cubic $HfO_2$ nanoparticles by incorporating 10 mol% of Ce at lower temperature. A eutectic mixture of LiCl/KCl is employed as a molten flux to synthesize Ce doped $HfO_2$ nanoparticels as an alternate to conventional solid state route.[145] Matović *et al.* report the stabilization of the cubic phase of $HfO_2$ at room temperature after doping 20 mol% of yttrium.[111] We have recently shown that by incorporating Dy upto 11 at%, the monoclinic phase of $HfO_2$ transforms to the high temperature cubic phase which remains stable at room temperature. The stabilization of the cubic phase is ascribed to the formation of oxygen vacancies generated by the substitution of $Dy^{3+}$ ions at $Hf^{4+}$ ion site.[144] It is supported by the first

principle calculation which predicts that when a trivalent dopant cation substitutes $Hf^{4+}$ ion, the deficiency of electrons in the host lattice occur and results in the formation of oxygen vacancies ($V_o$) due to charge compensation.[146, 147] The amount of oxygen vacancies vary with increase in trivalent dopant concentration. The incorporation of trivalent dopants in $HfO_2$ lattice lead to reduction in the formation energy to produce an oxygen vacancy. It is well known that in monoclinic $HfO_2$, the coordination number of $Hf^{4+}$ cation is 7, whereas the coordination number in high symmetry cubic phase of $HfO_2$ is 8.[146] In the present case, when the$Sm^{3+}$ ions having a lower charge state and a larger ionic radius, replace $Hf^{4+}$ ions, the oxygen vacancies are generated which prefer to reside near Hf atoms and leave 8-fold oxygen coordination to $Sm^{3+}$ ions in the host lattice.When$Sm^{3+}$ion concentrations are low, due to insufficient amount of oxygen vacancy, $HfO_2$exhibits the monoclinic phase and Hf is covalently bonded with O favoring 7-fold Hf coordination. With increase in Sm concentration, the energy needed to form an oxygen vacancy significantly decreases. As a result, a mixed phase of the monoclinic and cubic is observed for $0.05 \leq x \leq 0.11$. When a sufficient number of $Sm^{3+}$ ion forming a 8-fold coordination with oxygen ion are present in the lattice, the high temperature cubic phase of $HfO_2$ becomes stable even at room temperature. At $x = 0.12$, there exists a nominal concentration of oxygen vacancies associated to Hf cation resulting in a 8-fold oxygen coordination to $Sm^{3+}$ ions that surpass the 7-fold Hf coordination, thereby stabilizing the cubic phase at room temperature. Since RTFM behavior in Dy doped $HfO_2$ nanoparticles was quenched, we have not investigated the magnetic properties further.

### 4.2.4 Photoluminescence Properties

The monoclinic to cubic phase transformation driven by oxygen vacancies are further probed through its luminescence properties. The room temperature emission spectra of $HfO_2$ taken at the excitation wavelengths of 293 and 321 nm are shown in **figure 4.5 (a) and (b)**. Exciting $HfO_2$ under 293 nm, a broadband in the range of 360 to 550 nm showing a maximum at ~470 nm and two sharp emission peaks at 557 and ~613 nm are observed. The sharp peak located at 557 nm is attributed to 4-fold coordinated uncharged ($_{IV}V_o$) and single positively charged ($_{IV}V_o^+$) oxygen vacancies.[82, 147] The emission band at ~613 nm falling near red region could be due to $O(^1D) \rightarrow O(^3P)$ i.e. transition from singlet to triplet ground state of oxygen atom.[82, 148, 149] Due to the asymmetric shape of the broadband observed in the range of 360-550 nm, we have deconvoluted the spectrum into two distinct peaks named as peak 1 and 2located at 423 and 466 nm, respectively (see left inset of **figure 4.5 (a)**). While the former emission band (peak 1) is ascribed to 3-fold coordinated $_{III}V_o$ and the latter one (peak 2) could originate due to $_{III}V_o^+$.[82, 150, 151] Exciting $HfO_2$ with321 nm, except a significant increase in the intensity of peak at ~613 nm, no other peak is detected. Deconvoluted peaks such as peak 1 and 2 are found to be located at 440 and 479 nm indicating a red shift of ~15 nm. While peak 1 is quite suppressed under excitation wavelength of 293 nm, after exciting at 321 nm, the area under the peak is enhanced significantly.

**Figure 4.6 (a), (b) and (c)** depict the photoluminescence emission spectra of $Hf_{1-x}Sm_xO_2$ (x = 0,0.01, 0.05 and 0.12) excited at wavelength of 321, 410 and 465 nm, respectively. After exciting with 321 nm, $HfO_2$ shows emission peaks induced by oxygen vacancies related defects. In $Hf_{0.99}Sm_{0.01}O_2$, while the broadband is suppressed, emission

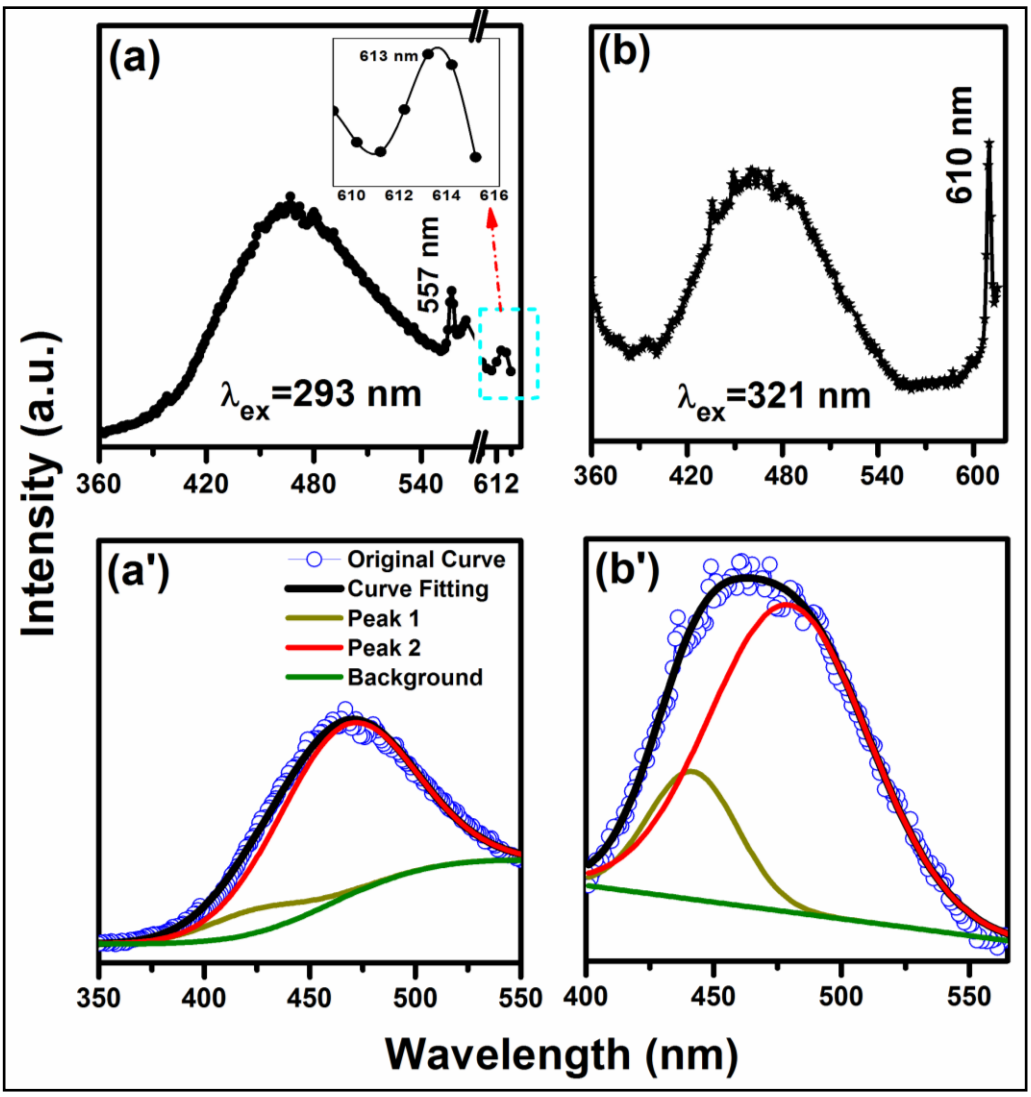


***Figure 4.5*** *Photoluminescence spectra of $HfO_2$ excited at* ***(a)*** *293 nm and* ***(b)*** *321 nm. The right inset of* ***(a)*** *shows emission peak at ~613 nm.****(a') and (b')****illustrate the deconvolution of broadband for 293 and 321 nm excitation wavelength, respectively.*

peak at ~613 nm of the host remain unchanged. With an increase in Sm concentration upto 12 at%, the intensity of peak at ~613 nm gradually decreases. Surprisingly, we do not observe any emission peak associated to $Sm^{3+}$ activator ion when excited with either 293 nm or 321 nm. Exciting $HfO_2$with 410 nm, a significant sharp emission peak is observed at 557 nm (**figure 4.6 (b)**). It could be due to relaxation of electrons from ${}_{IV}V_o$ and ${}_{IV}V_o^{+}$ to

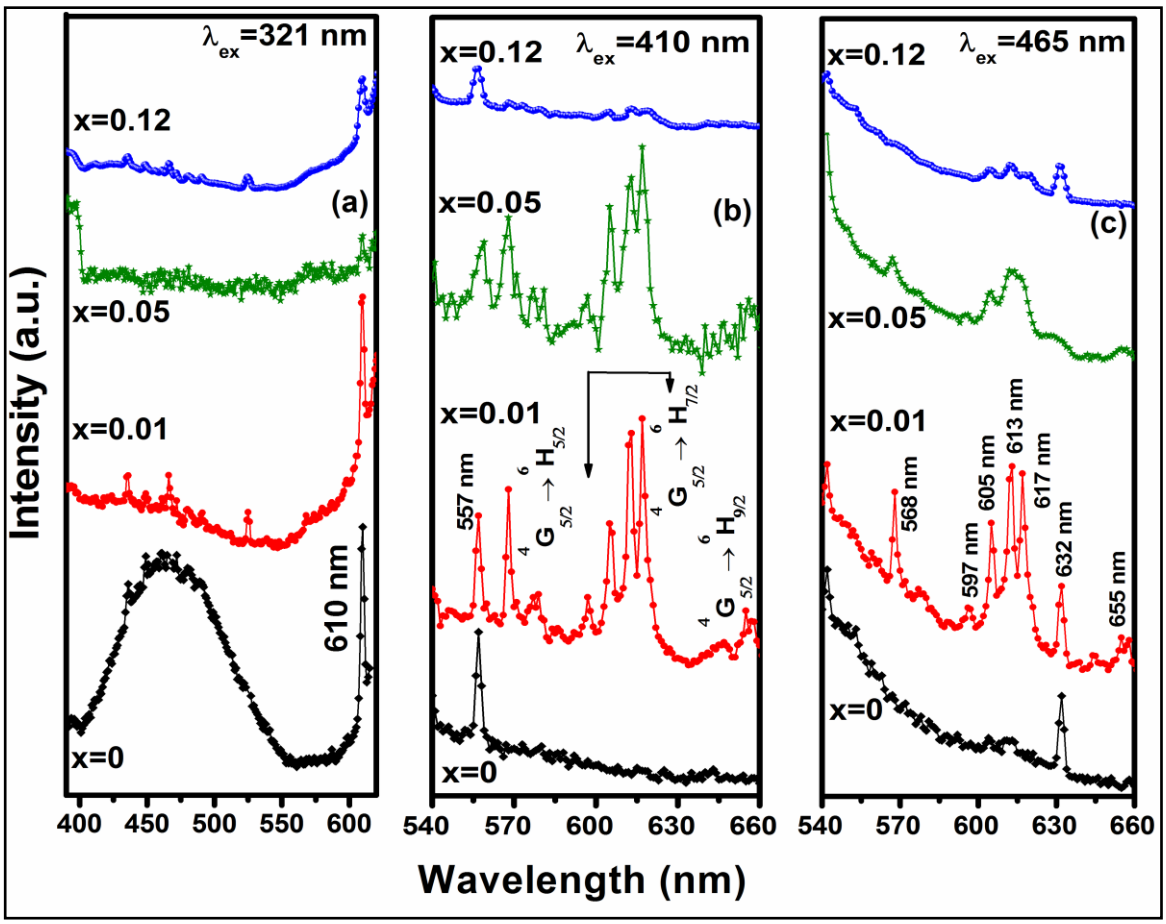


***Figure 4.6*** *Photoluminescence spectra of $Hf_{1-x}Sm_xO_2$ (x=0, 0.01, 0.05 and 0.12) excited at* ***(a)*** *321 nm,* ***(b)*** *410 nm and* ***(c)*** *465 nm.*

valence band of the host $HfO_2$.[82] After incorporating 1 at% of Sm, along with emission peak at 557 nm, the emission spectrum consists of several well resolved and distinct peaks at 568, 577, 597, 605, 613, 617 and 656 nm. These emission peaks emerge due to different *f-f* transition taking place within the energy level of $Sm^{3+}$ activator ion. The set of peaks centered at 568 and 577 nm in green/yellow, 597-617 nm in near red and 656 nm in pure red region are attributed to the transition from $^4G_{5/2}$ to $^6H_{5/2}$, $^6H_{7/2}$ and $^6H_{9/2}$, respectively.[152, 153] Such a nature of the $Sm^{3+}$ ion emission band is a characteristic of the Stark splitting induced because of the crystalline field of $HfO_2$. It is known that while

$^4G_{5/2} \rightarrow {}^6H_{5/2}$ is a magnetic dipole transition, $^4G_{5/2} \rightarrow {}^6H_{9/2}$ is an electric dipole transition which is hypersensitive to the crystal field environment. $^4G_{5/2} \rightarrow {}^6H_{7/2}$ exhibits a mix-up of electric and magnetic dipole transition components.[154] The low peak intensity corresponding to electric dipole transition than the magnetic one is an indication of the less asymmetric nature of the host $HfO_2$ lattice. The dominant nature of magnetic transition also demonstrates the presence of $Sm^{3+}$ ion at a low symmetry site with an inversion symmetry in the host lattice.[154, 155] Further, the intensity of these emission peaks decreases with increasing Sm concentration to 5 at%. At Sm concentration of 12 at%, except the peak at 557 nm of the host, all other emission peaks are significantly suppressed. Under an excitation wavelength of 465 nm, in the emission spectrum of $HfO_2$, one can observe the host emission peak at 632 nm which is red shifted by ~20 nm (**figure 4.6 (c)**). In $Hf_{0.99}Sm_{0.01}O_2$, the spectrum exhibits all characteristic emission peaks of $Sm^{3+}$ ion in the wavelength range of 540-660 nm. With increasing Sm concentration to 5 at%, all emission peaks become significantly broader and intensity decreases considerably. At x = 0.12, while emission peaks of $Sm^{3+}$ ion are reduced drastically, the peak at 632 nm of the host remains present. The broadness of the peaks is attributed to difference in crystal field strength and to different local environment, in particular, the high symmetry of cubic phase in this case.[156] The drastic reduction in the intensity of the emission peaks could be due to the change in the local symmetry around $Sm^{3+}$ ions. Besides the high symmetry, a higher Sm concentration leads to reduction in the mean distance between two $Sm^{3+}$ ions. This results in the cross relaxation between themselves present at different sites in the lattice by non-radiative transition processes such as exchange interaction, radiation reabsorption or electric multipolar interaction.[157-159] Considering the fact that $Hf_{0.88}Sm_{0.12}O_2$ exhibits

the high symmetry cubic phase, the observed luminescence behavior is in agreement with reported literature which also supported by our XRD results.[54, 156, 157, 160] In this context, Rauwel *et al*. observe an emission peak at 3.1 eV (390-400 nm) in cubic phase $HfO_2$ stabilized using benzyl amine solvent.[51] However, this emission peak is not only absent in emission spectrum of $Hf_{0.88}Sm_{0.12}O_2$, but also in cubic phase stabilized using 7 at% of Lu in $HfO_2$:3.3% Eu and 10 mol% of Lu in $HfO_2$:1 mol% Eu do not show the emission peak at 3.1 eV.[156]

Since the host emission is observed at ~470 nm and characteristic emission of $Sm^{3+}$ at 617 nm, we have taken the excitation spectra of $HfO_2$ and $Hf_{0.99}Sm_{0.01}O_2$ depicted in **Figure 4.7 (a)**. In $HfO_2$, it can be found that the excitation spectrum shows a broadband in the range of 250-350 nm with a maximum at ~293 nm. Another sharp peak is observed at 430 nm. While the former band is ascribed to the host absorption, the latter peak appears due to the defect states such as oxygen vacancies in $HfO_2$ lattice.[54, 144] However, for $Hf_{0.99}Sm_{0.01}O_2$, the broadband disappears completely and the peak at 430 nm remains present with reduced intensity. It is to be noted that no peak related to $Sm^{3+}$ ion is observed. **Figure 4.7(b)** depicts the excitation spectra recorded by monitoring the characteristic emission peak at 617 nm corresponding to $Sm^{3+}$ ion. In $HfO_2$, the spectrum exhibits peaks of low intensity in the wavelength range of 450-480 nm. This appears because of the host absorption to $_{III}V_o^+$ defect states. In addition, these peaks could correspond to the host emission observed at ~613 nm since it lies very near to the characteristic emission band of $Sm^{3+}$ ion. However, for $Hf_{0.99}Sm_{0.01}O_2$, one can observe two prominent sharp peaks within the excitation spectrum. While the excitation peaks located within the wavelength range of 400-420 nm (maximum at 405 nm) originate due to

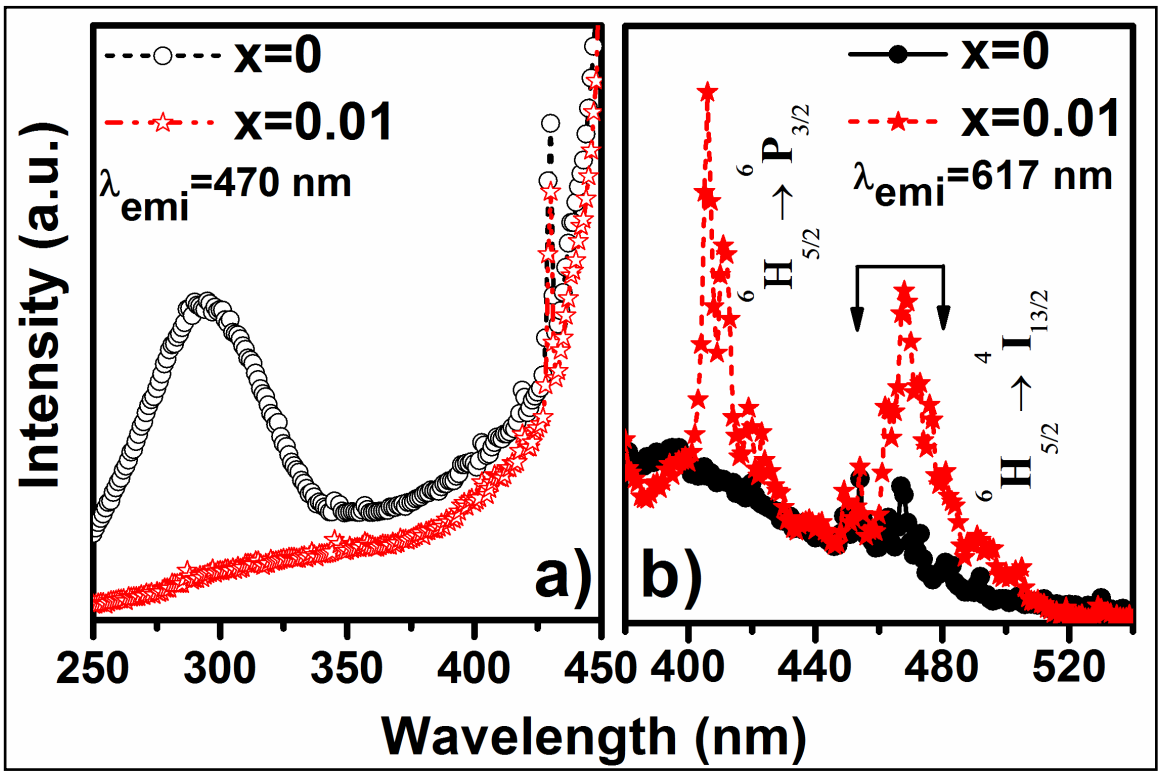


***Figure 4.7*** *Room temperature excitation spectra of $HfO_2$ and $Hf_{0.99}Sm_{0.01}O_2$ monitored at emission wavelength* ***(a)*** *470 nm and* ***(b)*** *617 nm.*

the transition $^6H_{5/2} \rightarrow {}^6P_{3/2}$, the peaks in the wavelength range of 460-490 nm (maximum at 468 nm) correspond to $^6H_{5/2} \rightarrow {}^4I_{13/2}$ transition of $Sm^{3+}$ ion.[161] One may note that the excitation peaks within the wavelength range of 450-490 nm coexist for both $HfO_2$ and $Hf_{0.99}Sm_{0.01}O_2$. The similar peak positions in 460-490 nm range in the excitation spectra show that a few defect levels of $HfO_2$ takes part by transferring charge weakly to $Sm^{3+}$ion inducing their characteristic emissions. **Figure 4.8** depicts the two dimensional (x, y) CIE color space chromaticity diagram of $Hf_{1-x}Sm_xO_2$ (x = 0 and 0.01) under different excitation wavelengths. The CIE chromaticity coordinates of $HfO_2$ are found to be (0.18,0.26) and (0.26, 0.28) for $\lambda_{ex}$ = 293 and 321 nm, respectively. For $Hf_{1-x}Sm_xO_2$ (x = 0.01), CIE

coordinated are (0.40, 0.50) and (0.28, 0.46) for $\lambda_{ex}$ = 410 and 465 nm, respectively. Since the broadband in the range of 350-550 nm is dominating compared to emission peaks at557 and ~613 nm, the host $HfO_2$ emits a blue color light under an excitation wavelength of 293 nm. When excited with 321 nm, although the emission peak at 557 nm is disappeared, due to significant contribution from the emission peak at ~613 nm, the host $HfO_2$ produces a bluish cool white light. In $Hf_{1-x}Sm_xO_2$ (x = 0.01), we reveal near green and green-yellow emission from CIE diagram after exciting with 410 and 465 nm, respectively.

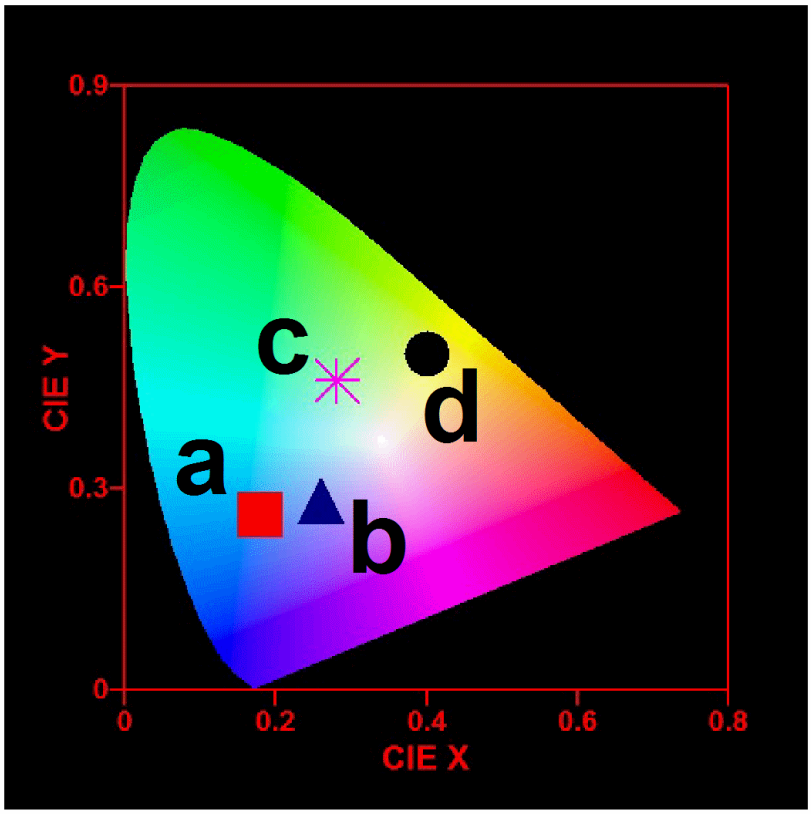


***Figure 4.8*** *The CIE color space chromaticity diagram (Point 'a' and 'b' correspond to $HfO_2$ for $\lambda_{ex}$ = 293 and 321nm; 'c' and 'd' correspond to $Hf_{0.99}Sm_{0.01}O_2$ for $\lambda_{ex}$ = 410 and 465 nm, respectively).*

### 4.2.5 Energy Band Diagram

In order to understand the detailed photoluminescence behavior of $Hf_{1-x}Sm_xO_2$, a schematic energy level diagram has been presented considering the different excitation and emission processes (**figure 4.9**). The various energy levels are specified as $^6P_{3/2}$, $^4I_{13/2}$, $^4G_{5/2}$, $^6H_{5/2}$, $^6H_{5/2}$ and $^6H_{5/2}$ corresponding to $Sm^{3+}$ ion and $_{III}V_o$, $_{III}V_o^+$, $_{IV}V_o$, $_{IV}V_o^+$, O($^1$D) and O($^3$P) associated to the host $HfO_2$ lattice. Exciting with 293, 321, 410, 425 or 465 nm, electrons at valence band (VB) of $HfO_2$ are not excited to conduction band (CB) due to wide band gap of ~5.7 eV of $HfO_2$. The electrons can only be excited to the host charge transfer band (CTB) located below CB, after exciting with the highest energy i.e. lower excitation wavelength of 293 nm. The relaxation of excited electrons to VB through different defect levels show host related emissions as observed at 423, 466, 557 and ~613 nm from emission spectra of $HfO_2$ (**figure 4.5**). Exciting at 321 nm, we also observed similar emission peaks which are only host related emissions. In 1 at% Sm doped$HfO_2$, no peak of $Sm^{3+}$ion is detected after exciting with either 293 or 321 nm which indicates the absence of charge transfer from the host CTB to $Sm^{3+}$ activator ion. This is mainly because of the significant energy difference between the host CTB and emission level of $Sm^{3+}$ ion. However, at higher excitation wavelengths of 410, 425 or 465 nm of visible range, along with one of the host emissions at ~557 or ~613 nm, characteristic emission peaks of $Sm^{3+}$ ion are observed in the range of 568-580, 600-620 and 650-657 nm. Such emissions are only possible when there is a charge transfer from the defect levels of host to different energy levels of $Sm^{3+}$ activator ion. Previously, we report that host CTB weakly sensitize sensitize the luminescence of $Dy^{3+}$ ions producing bluish cool white emission (CIE coordinate: (0.27, 0.27) for 1 at% Dy).[144]

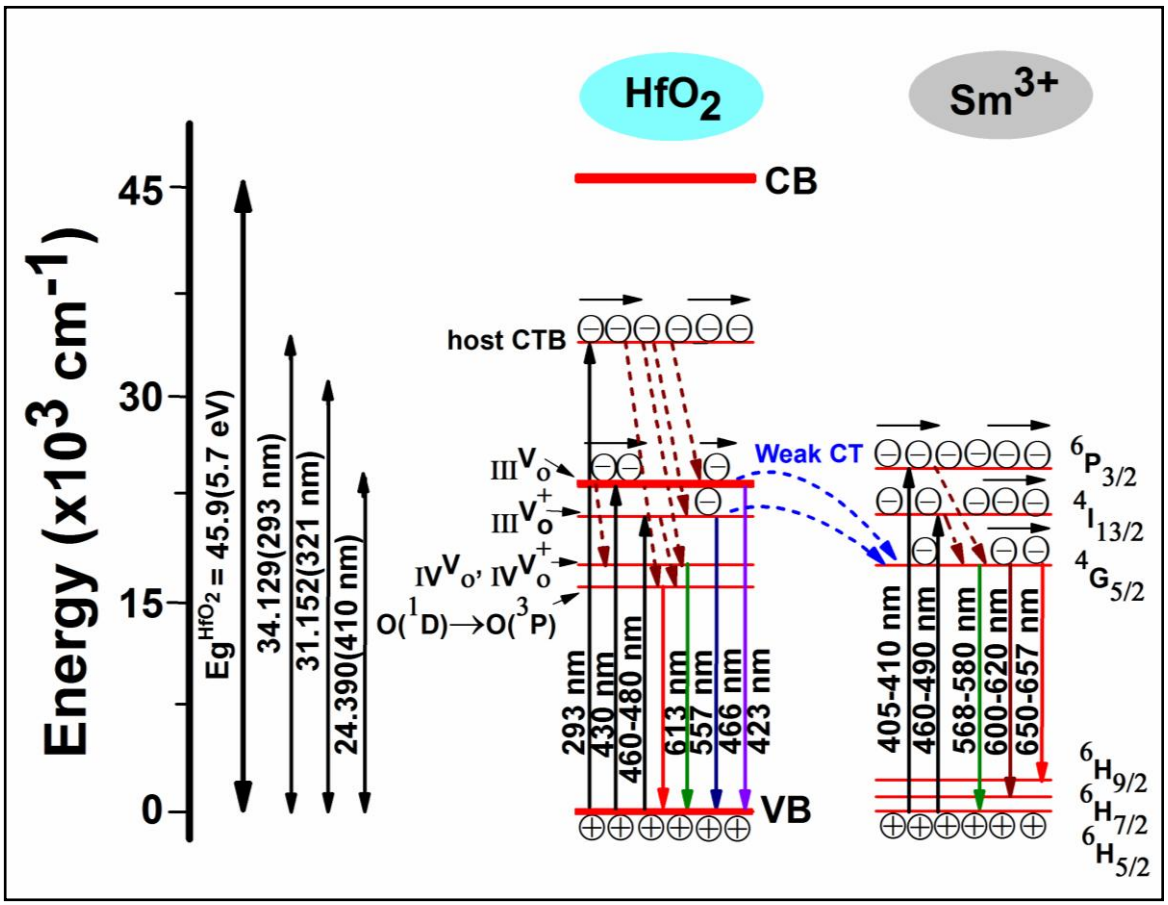


***Figure 4.9*** *A schematic energy band diagram showing the excitation and emission processes involved in* $HfO_2$ *and* $Hf_{0.99}Sm_{0.01}O_2$ *nanoparticles.*

Herein, under an excitation wavelength of 321 nm, without any rare earth ion, the host $HfO_2$ gives a similar CIE coordinate of (0.26, 0.28). While the host CTB do not transfer charge to $Sm^{3+}$ ions exciting with UV light, the optically active oxygen related defect levels acting as sensitizers show weak charge transfer phenomenon when excited at energy comparable to the energy of defect levels of $HfO_2$. Therefore, one may note that in wide band gap oxides like $HfO_2$, by incorporating $Sm^{3+}$ ion, it is possible to tune the light emissions producing a range of colors in visible region. These materials are thus important for optoelectronic device applications.

## 4.3 Conclusions

This chapter systematically investigated the structural and photoluminescence properties of $HfO_2$ and Sm doped $HfO_2$ nanoparticles with varying Sm concentration (1-12 at%). $HfO_2$ crystallized in monoclinic phase with an average particle size of ~35 nm. By incorporation of 5 at% of Sm into $HfO_2$ lattice, it could be possible to partly transform the monoclinic phase to cubic one. Above 5 at%, cubic phase fraction increased at the cost of monoclinic one and at x = 0.12, the cubic phase of $HfO_2$ was completely stabilized at room temperature. The phase transformation from the monoclinic to cubic phase was accompanied with dramatic enhancement of lattice strain and reduction in size analyzed from Williamson-Hall plot. A prospective role of Sm incorporation stabilizing the cubic phase in $HfO_2$ lattice has been examined considering the valency of Sm and difference in ionic radii of $Sm^{3+}$ and $Hf^{4+}$ ion. Selected area electron diffraction patterns and the lattice spacing estimated from high resolution TEM further confirmed the monoclinic, $P2_1/c$, and cubic, $Fm\bar{3}m$, phase in $HfO_2$ and $Hf_{0.88}Sm_{0.12}O_2$ nanoparticles, respectively. Being $HfO_2$ an outstanding host material, after $Sm^{3+}$ ion incorporation, the photoluminescence studies

revealed an excellent emissions in near green and red region due to the charge transfer phenomenon occurring between the host and different energy levels of $Sm^{3+}$ ion. Combining different excitation and emission processes, a schematic energy band diagram was proposed.

# Chapter 5

## 5.1 Introduction

Previously, in chapter 3 and 4, we have established that after incorporating either 11 at% of Dy or 12 at% of Sm into $HfO_2$ lattice, one can completely stabilize the high temperature cubic phase at room temperature. This chapter primarily investigates the structure and photoluminescence properties of Dy and Sm codoped $HfO_2$. In particular, we introduce the concept of stabilizing cubic phase of $HfO_2$ at room temperature after codoping Dy and Sm. Since 1 at% of Dy or Sm doped $HfO_2$ demonstrate excellent luminescence properties, *x*Dy,*y*Sm:$HfO_2$ nanophosphors having low dopant concentrations have been utilized as prospective dusting powder to demonstrate the robustness in developing latent fingerprint (LFPs) for forensic investigations. The developed LFPs onto multivariate object surfaces such as aluminum foil, glass and colored plastic sheets etc exhibit vital details including termination sand bifurcations.

## 5.2 Results and Discussion

### 5.2.1 Phase and Structural Transformation of Dy and Sm:$HfO_2$

In order to investigate the phase transformation in $HfO_2$ after codoping Dy and Sm, first, *x*Dy,*y*Sm:$HfO_2$ powders ((*x*=*y*=6); (*x*=6, *y*=7) and (*x*=7, *y*=6)) calcined at 900 $^oC$ have been characterized by XRD and results are shown in **figure 5.1.** It is evident from XRD patterns that at *x*=*y*=6, along with the intense characteristic diffraction peaks such as (111), (002), (022), (113), and (222) corresponding to the cubic phase, $Fm\bar{3}m$ of $HfO_2$, a few other peaks at $2\theta$ = 24.6 and 28.3$^o$ appear which are attributed to the monoclinic phase. Because of meager contribution of the monoclinic phase, the cubic phase of $HfO_2$ prevails

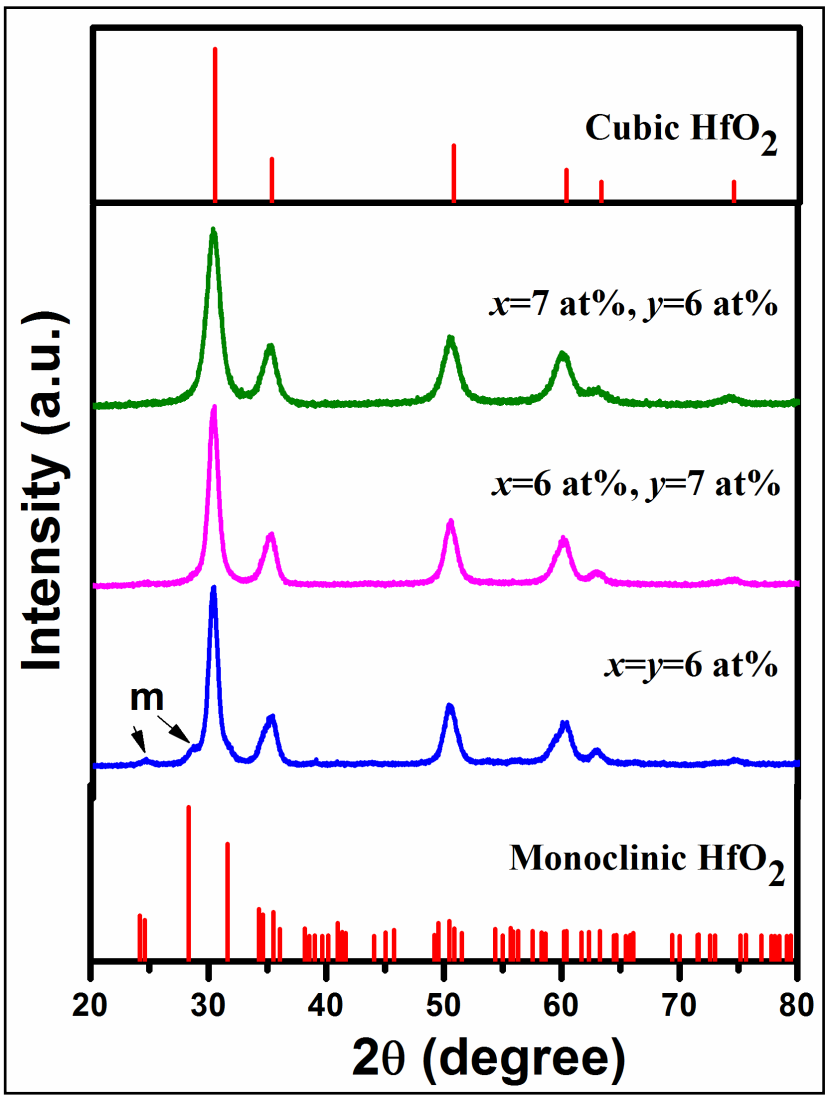


***Figure 5.1*** *XRD patterns of xDy,ySm:$HfO_2$powders ((x=y=6); (x=6, y=7) and (x=7, y=6)) calcined at 900 $^oC$.*

| **Dy (*x*), Sm (*y*) (at%)** | *x*=0, *y*=0 | *x*=0.5, *y*=0 | *x*=0, *y*=0.5 | *x*=0.5, *y*=0.1 | *x*=0.5, *y*=0.3 | *x*=0.5, *y*=0.5 | *x*=0.5, *y*=1 | *x*=0.5, *y*=2 |
|---|---|---|---|---|---|---|---|---|
| **Sample** | D0S0 | D0.5S0 | D0S0.5 | D0.5S0.1 | D0.5S0.3 | D0.5S0.5 | D0.5S1 | D0.5S2 |

***Table 5.1*** *List of synthesized samples with various compositions of xDy,ySm:$HfO_2$ powders with low dopant concentration.*

in this sample. However, in case of *x*=6, *y*=7 and *x*=7, *y*=6 at%, the monoclinic phase of $HfO_2$ is completely suppressed and the diffraction peaks corresponding to pure cubic phase are obtained. Therefore, in Dy and Sm codoped $HfO_2$, it is established that the high temperature cubic phase can be stabilized at RT when Dy and Sm codopant concentration attains 13 at%.

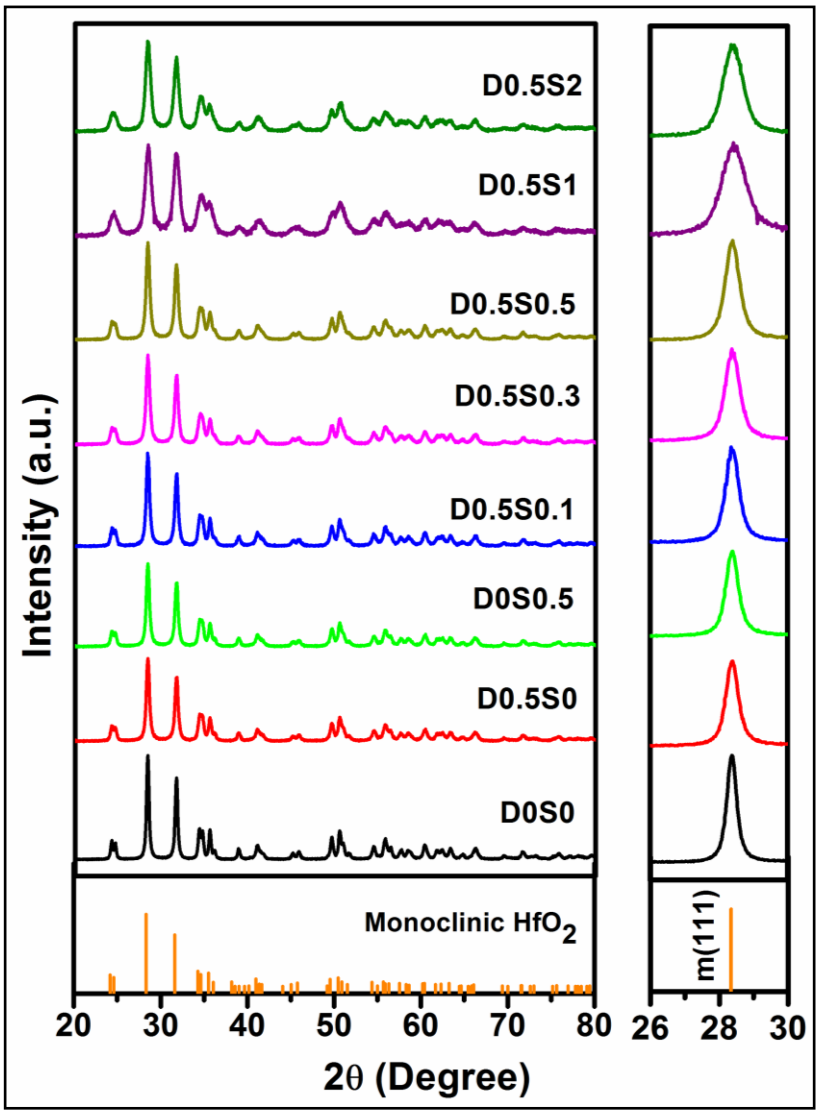


***Figure 5.2*** *XRD of $Dy^{3+}$ and $Sm^{3+}$ coactivated $HfO_2$ powders calcined at 900 $^oC$ (left panel). Right panel indicates broadening of (T11) peak corresponding to monoclinic phase of $HfO_2$.*

**Figure 5.2** depicts the XRD patterns of *x*Dy,*y*Sm:$HfO_2$ powders with low dopant concentration (listed in **table 5.1**) calcined at 900 °C under ambient conditions. Apparently, XRD patterns exhibit sharp and well resolved diffraction peaks distinctive to crystalline particles. For D0S0, the diffraction peaks are identified as (011), (110), ($\bar{1}$11), (111), (020), (200), (021), ($\bar{2}$11) and (112) of the monoclinic phase, space group, $P2_1/c$ (JCPDS card no. 78-0049) of $HfO_2$. In D0.5S0.5 sample, one can explicitly note that the intensity of diffraction peaks diminishes noticeably and peaks become broad indicating a significant reduction in crystallite size. While keeping Dy concentration constant at 0.5 at%, increase

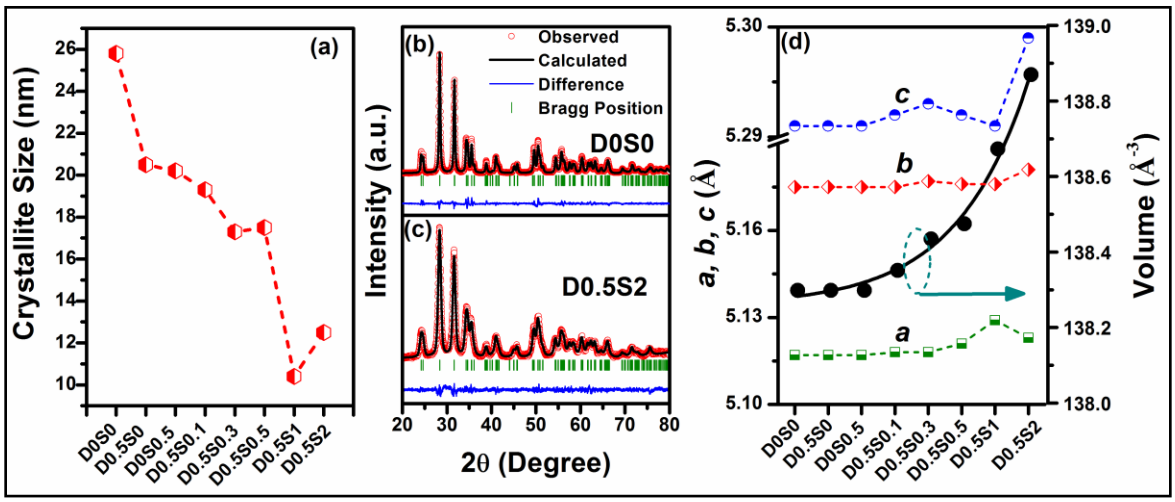


***Figure 5.3 (a)*** *Variation in crystallite size calculated along ($\bar{1}$11) as a function of Dy and Sm concentration; Le-Bail refinement profiles of XRD data of* ***(b)****D0S0* ***(c)*** *D0.5S2 and* ***(d)*** *dependence of lattice constants such as a, b, c and volume upon Dy and Sm concentrations.*

in Sm concentration upto 2 at% indicates broad diffraction peaks demonstrating fine particles. Considering the fact that positions of diffraction peaks remain same, it is noteworthy to mention that incorporation of Sm upto 2 at% in $HfO_2$ lattice does not change

the crystal structure. The crystallite size of the above compounds is estimated using Debye-Scherrer equation as given below.[162]

$$D = k\lambda/\beta Cos\theta$$

where D is crystallite size, λ is X-ray wavelength, k is constant related to shape of particles, β is full width at half maximum (FWHM in radians) estimated after subtracting instrumental broadening and K$\alpha_2$ contributions and θ is the Bragg's angle. The variation in crystallite size calculated along (T11) is shown in **figure 5.3 (a)**. For D0S0, the crystallite size is found to be ~25 nm which substantially decreases to ~20 nm for D0.5S0.5 sample. The crystallite size further reduces to ~10 nm with increasing Sm concentration upto 2 at%. Such a systematic reduction in crystallite size with Sm concentration indicates a higher nucleation rate than the growth rate. It is worth to determine the lattice parameters while the particle size reduces from ~25 to ~10 nm with increase in Sm concentration.

Therefore, XRD patterns are fitted using Le-Bail profile fitting of FULLPROF program with pseudo-Voigt function to refine unit cell parameters such as lattice constants and cell volume. **Figure 5.3 (b) and (c)** shows the typical Le-Bail profile fitting of XRD data with space group, $P2_1/c$ for D0S0 and D0.5S2, respectively. The observed pattern, calculated data after fitting, and the difference pattern between observed and calculated data are shown as open circle, continuous line and as a bottom line, respectively. The vertical tick marks on top of the difference pattern show respective positions of Bragg peaks. All the observed Bragg profiles fit well with monoclinic phase, $P2_1/c$ of $HfO_2$. The variation in lattice constants and cell volume of *x*Dy,*y*Sm:$HfO_2$with different Sm and Dy concentrations is shown in **figure 5.3 (d)**. One can clearly observe the gradual increment of lattice constants such as '*a'*, '*b'* and '*c'* resulting in enlarged cell volume with increasing Sm

concentrations. While the lattice constant *a* and *b* varies from 5.117 to 5.123 Å and 5.175 to 5.181 Å, respectively, *c* monotonically increases from 5.291 to 5.299 Å. As a result, an exponential expansion of monoclinic cell volume from 138.30 to 138.87 $Å^3$ is observed with increasing Sm concentration. In the monoclinic phase of $HfO_2$, Hf forms a covalent bond with oxygen and exhibits seven coordinated $Hf^{4+}$ ions.[53, 109] For a 7-fold coordination, the ionic radius of $Dy^{3+}$ (0.97 Å) and $Sm^{3+}$ (1.02 Å) is relatively larger than that of $Hf^{4+}$ (0.76 Å) ion. Therefore, an enhancement in cell volume is attributed to the significant difference in ionic radii of $Dy^{3+}$, $Sm^{3+}$ and $Hf^{4+}$ cations. Further, it is observed that the crystallite size decreases while cell volume is enhanced exponentially. Yang *et al*. report a similar trend of exponential enhancement of cell volume with reduction in crystallite size for Eu doped $GdVO_4$ nanoparticles.[163] The plausible reason is described in the context of so called "Madelung model". The model suggests that an effective negative pressure can be triggered in nanosized particles due to surplus of Madelung energy which is a manifestation of both Coulomb attractive and repulsive interactions.[164, 165] Despite preserving the monoclinic phase of $HfO_2$, it can be inferred from the above observations that a nominal concentration of $Dy^{3+}$ and $Sm^{3+}$ substitute $Hf^{4+}$ ions in the lattice.

### 5.2.2 Microstructural Analysis

In order to realize the shape and size of synthesized powders, FE-SEM images of D0S0, D0.5S0, D0.5S0.3 and D0.5S2 are shown in **figure 5.4.** It clearly reveals the aggregate nature of particles. Therefore, transmission electron micrograph depicted in **figure 5.5** shows partially agglomerated particles that exhibited semi-spherical shape. The estimated particle size histograms show the average particle size of ~31, 22, 18 and 16 nm

for D0S0,D0.5S0, D0.5S0.3 and D0.5S2, respectively which are sufficiently close to the crystallite size calculated using Debye-Scherrer equation.

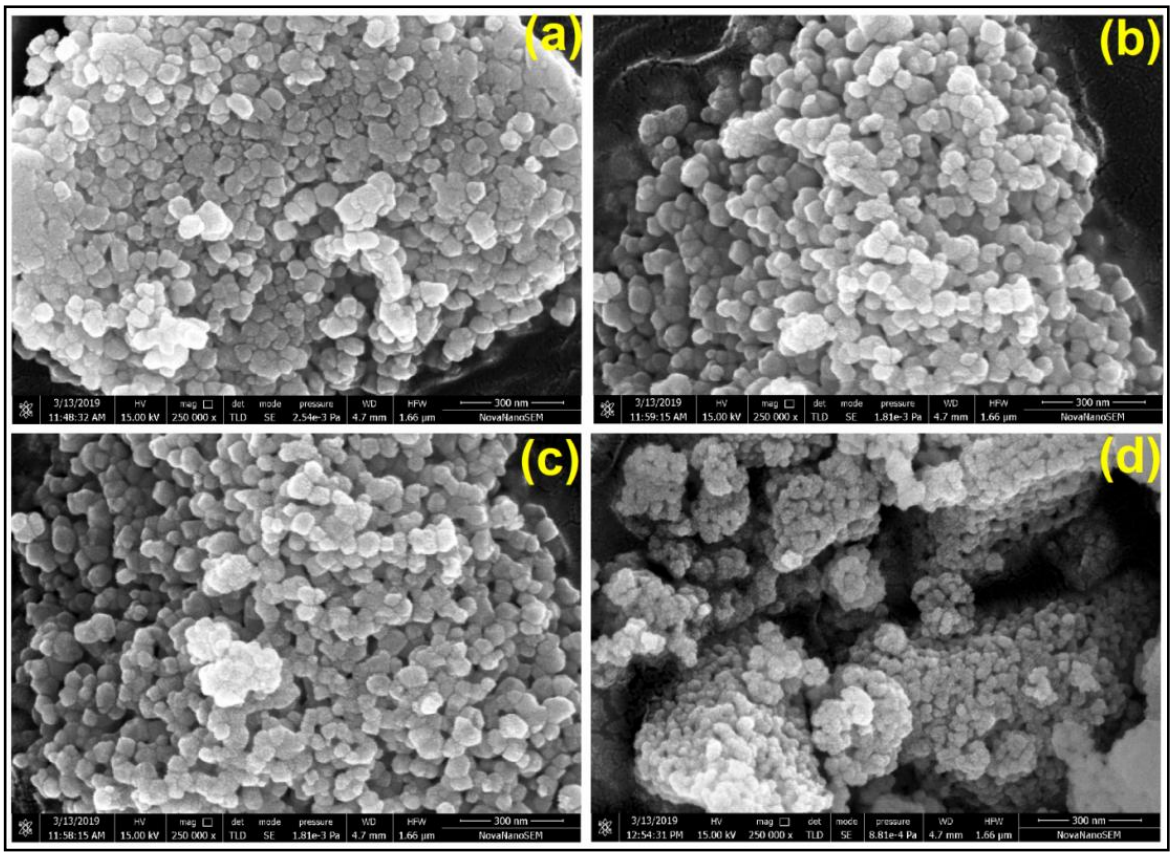


***Figure 5.4*** *Field emission- scanning electron micrographs (FE-SEM) of* ***(a)*** *D0S0,* ***(b)*** *D0.5S0,* ***(c)*** *D0.5S0.3 and* ***(d)*** *D0.5S2.*

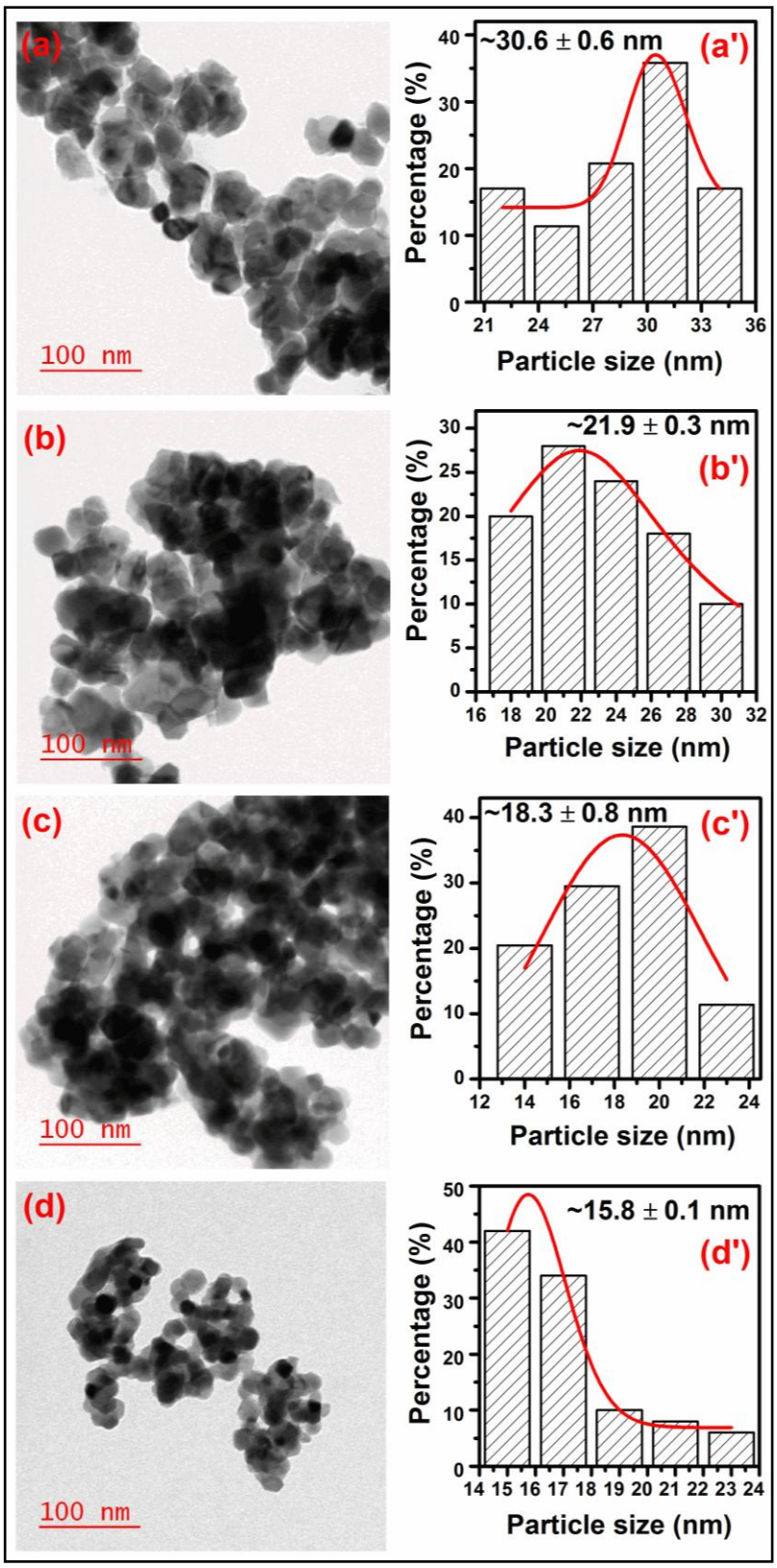


***Figure 5.5*** *TEM micrographs of* ***(a)*** *D0S0,* ***(b)*** *D0.5S0,* ***(c)*** *D0.5S0.3 and* ***(d)*** *D0.5S2.* ***a'-d'*** *show corresponding particle size distribution histograms.*

### 5.2.3 Photoluminescence properties

The photoluminescence (PL) properties of *x*Dy,*y*Sm:$HfO_2$ nanoparticles with different Dy and Sm concentrations are studied by means of emission, excitation and time resolved decay spectra. The excitation and emission spectra discretely correspond to the different excited and ground energy states, respectively available for electronic transitions. The excitation spectra are crucial in determining the distinct wavelengths of light that exclusively produce desired fluorescence and also useful for examining charge transfer phenomenon. The emission or excitation spectra have been measured after exposing sample by selecting the highest excitation/emission peak observed in respective PL spectrum. **Figure 5.6 (a)** depicts the excitation and emission spectra of D0.5S0 nanoparticles. The excitation spectrum observed by monitoring $Dy^{3+}$ ion characteristic emission at 577 nm demonstrates the strongest peak centered at 352 nm emerging due to a direct excitation of electrons from $^6H_{15/2} \rightarrow {}^6P_{7/2}$ energy level. In addition, few more sharp peaks are found to be located at 367, 383 393, 425 and 448 nm assigned to various *f-f* band transitions of $Dy^{3+}$ activator ion taking place from the ground state, $^6H_{15/2}$ to $^6P_{5/2}$, $^4F_{7/2}$, $^4I_{13/2}$, $^6G_{11/2}$ and $^4I_{15/2}$ excited energy levels, respectively. After exciting D0.5S0 nanoparticles at a wavelength of 393 nm (**figure 5.6 (a')**), the emission spectrum reveals two strong characteristic emission peaks of $Dy^{3+}$ activator ion centered at 490 and 577 nm.[135, 166] Previously, we have obtained a similar emission spectrum for 1 at% Dy doped $HfO_2$ nanoparticles under an excitation wavelength of 352 nm.[167] Such characteristic emission peaks appear due to different electronic transitions occurring within distinct $Dy^{3+}$ ion energy levels. While emission peak centered at 490 nm in blue region is ascribed to $^4F_{9/2} \rightarrow {}^6H_{15/2}$, the well separated peak located at 577 nm in yellow region

emerges primarily due to radiative relaxation of energetic electrons from metastable state, $^4F_{9/2}$ to $^6H_{13/2}$, ground state of $Dy^{3+}$ activator ion. The emission peak occurring because of $^4F_{9/2} \rightarrow {}^6H_{13/2}$ transition is an allowed electric dipole transition which can be significantly affected by the crystal field strength around $Dy^{3+}$ activator ion. However, the magnetic dipole transition, $^4F_{9/2} \rightarrow {}^6H_{15/2}$ is nearly insensitive to crystal field environments when $Dy^{3+}$ ion resides at an inversion centre site with low symmetry. More often, at a site without an

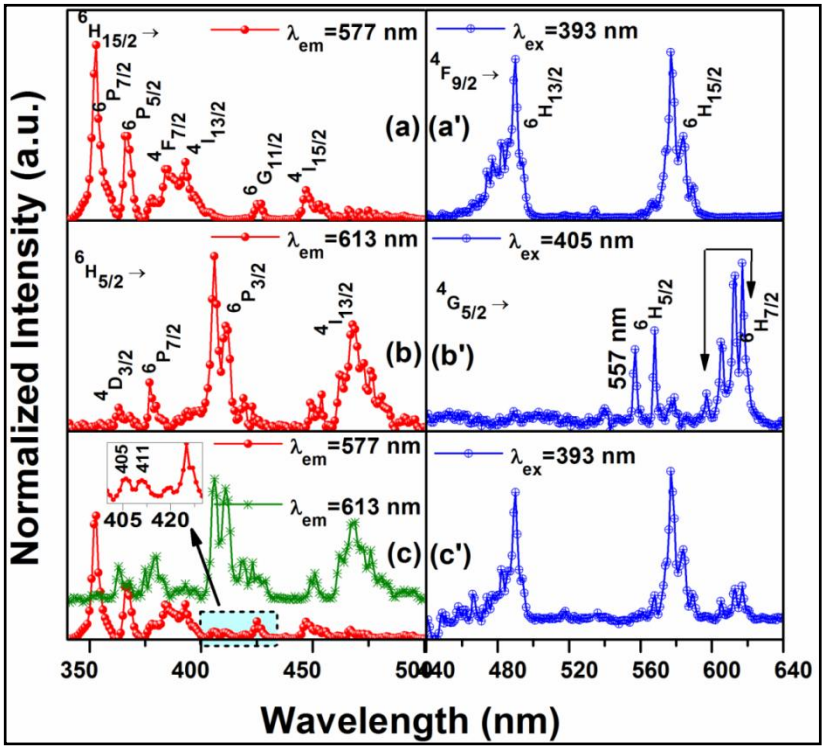


***Figure 5.6*** *Room temperature excitation and emission spectra of xDy,ySm:$HfO_2$ nanoparticles* ***(a)*** *D0.5S0 ($\lambda_{ex}$=393 nm, $\lambda_{em}$=577 nm),* ***(b)*** *D0S0.5 ($\lambda_{ex}$=405 nm, $\lambda_{em}$=613 nm) and* ***(c)*** *D0.5S2 ($\lambda_{ex}$=393 nm, $\lambda_{em}$=577 and 613 nm).*

inversion symmetry, the electric dipole transition prevails over the magnetic one.[137, 138, 167, 168] For D0S0.5 nanoparticles, the excitation spectrum is obtained in wavelength range of 340 to 500 nm after fixing the typical emission wavelength at 613 nm of $Sm^{3+}$ ion as shown in **figure 5.6 (b)**. The excitation spectrum reveals distinguished set of intense peaks within the wavelength range of 400-420 nm (vertex at 405 nm) and 460-490 nm

(vertex at 468 nm). While the former set of excitation peaks corresponds to transition, $^6H_{5/2} \rightarrow {}^6P_{3/2}$, the latter one originates essentially due to $^6H_{5/2} \rightarrow {}^4I_{13/2}$, transition of $Sm^{3+}$ ion. Two more excitation peaks having moderate intensity located at 362 and 378 nm in lower wavelength region are attributed to transition of electrons from ground state, $^6H_{5/2}$ to $^4D_{3/2}$ and $^6P_{7/2}$ excited states, respectively.[169, 170] It is to be noted that the excitation wavelength of 393 nm does not show any emission in D0S0.5 nanoparticles. Therefore, the emission spectrum is obtained after exciting at a wavelength of 405 nm in the wavelength range of 440-640 nm as demonstrated in **figure 5.6 (b')**. Several discrete peaks are found at 568, 577, 597, 605, 613 and 617 nm. The emission peaks located at 568 and 577 nm lying in yellow or green region arise when excited electrons relax directly from $^4G_{5/2}$ to $^6H_{5/2}$, ground state, whereas peaks in the wavelength range of 597-617 nm in near red region appear due to electronic transition, $^4G_{5/2} \rightarrow {}^6H_{5/2}$.[155] Additionally, one can notice a sharp peak at 557 nm predominantly associated to transitions occurring from different defect levels within the host, $HfO_2$.[82, 169, 171]

**Figure 5.6 (c)** compares the excitation spectra of D0.5S2 nanoparticles taken by monitoring the wavelengths of 577 and 613 nm corresponding to characteristic emissions of $Dy^{3+}$ and $Sm^{3+}$ ion, respectively. For $\lambda_{em}$ = 577 nm, the excitation spectrum exhibits a similar set of excitation peaks to that of $Dy^{3+}$ ion along with new small peaks within the wavelength range of 400-430 nm. With an enlarged view of 400-430 nm wavelength regime, the inset in **figure 5.6 (c)** clearly demonstrates the existence of excitation peaks such as 405 and 411 nm corresponding to $Sm^{3+}$ ion ($^6H_{5/2} \rightarrow {}^6P_{3/2}$). It is surprising that the excitation peaks of $Sm^{3+}$ coexist within excitation spectrum corresponding to $Dy^{3+}$ ion. Since, the excitation peak located at 393 nm of $Dy^{3+}$ ($^4I_{13/2}$) is sufficiently close to $^6P_{3/2}$

energy level of $Sm^{3+}$ ion, thereby D0.5S2 nanoparticles are excited under an excitation wavelength of 393 nm. Interestingly, the emission spectrum reveals the typical set of emission peaks associated to $Dy^{3+}$ ion together with prominent peaks in wavelength range of 600-640 nm attributed to $Sm^{3+}$ activator ion. Such a coexistence of characteristic emission peaks corresponding to $Dy^{3+}$ and $Sm^{3+}$ ion is only possible if there is transfer of excited electrons between energy levels of $Dy^{3+}$ and $Sm^{3+}$ active ions. Villabona-Leal *et al.* report the enhancement in luminescence intensity due to an energy transfer process occurring among $Eu^{3+}$ and $Gd^{3+}$ active ions codoped in a similar system like $ZrO_2$.[172]

After exciting at 393 nm, the emission spectra of *x*Dy,*y*Sm:$HfO_2$ are shown in **figure 5.7**. For D0.5S0 sample, the emission spectrum consists of two prominent peaks observed at 490 and 577 nm. Keeping Dy concentration constant at 0.5 at%, with increase in Sm concentration from 0.01 to 0.05 at%, along with strong emissions corresponding to$Dy^{3+}$ ion, a set of emission peaks are observed at 605, 613 and 617 nm (see right panel of **figure 5.7**). Interestingly, these emission peaks become well resolved, distinguishable and more prominent with increasing Sm concentration upto 2 at%. These set of emission peaks in near red region (605-617 nm) are result of electronic transition taking place from $^4G_{5/2}$ to $^6H_{7/2}$, ground state of $Sm^{3+}$ ion. The distinct character of emission peaks corresponding to $Sm^{3+}$ ion is indicative of Stark splitting under the crystalline field of host lattice. The direct transition, $^4G_{5/2} \rightarrow {}^6H_{7/2}$ includes contributions from both the magnetically and electrically allowed dipole transitions.[155, 173, 174] Therefore, it can be accomplished that in Dy and Sm codoped $HfO_2$, $Dy^{3+}$ ions are capable of sensitizing the photoluminescence properties of $Sm^{3+}$ activator ion through an efficient mutual interaction rendering improved optical properties.

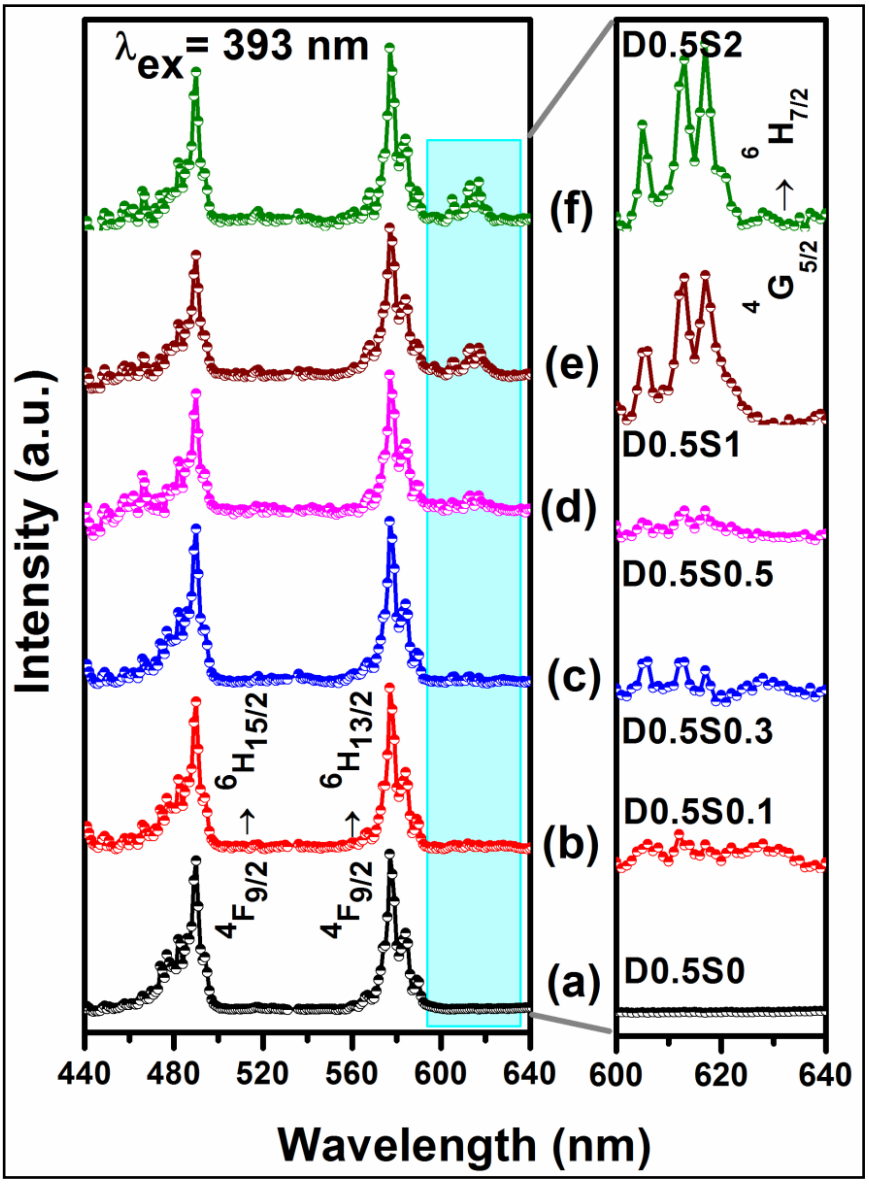


***Figure 5.7*** *Room temperature PL emission spectra of xDy,ySm:$HfO_2$ nanoparticles obtained under an excitation wavelength of 393 nm. In right panel, an enlarged view of emission peaks within the wavelength range of 600-640 nm is shown. (**a-f** correspond to D0.5S0, D0.5S0.1, D0.5S0.3, D0.5S0.5, D0.5S1, and D0.5S2, respectively).*

### 5.2.4 Time Resolved Decay Curves

The presence of possible inter-system energy transfer phenomenon occurring within $Dy^{3+}$ and $Sm^{3+}$ coactivated $HfO_2$ nanoparticles is studied in the context of time resolved luminescence decay curves. **Figure 5.8 (a-f)** show the luminescence decay curves of

*x*Dy,*y*Sm:$HfO_2$ nanoparticles as a function of Sm concentration with constant Dy concentration (0.5 at%). The time resolved decay curves are collected in millisecond time domain after exciting at a wavelength of 393 nm while monitoring emission peak at 577 nm of $Dy^{3+}$ ion. Apparently, the luminescence decay lifetime could be affected by the presence of $Dy^{3+}$ and/or $Sm^{3+}$ ions which may not be evenly distributed in $HfO_2$ lattice. As

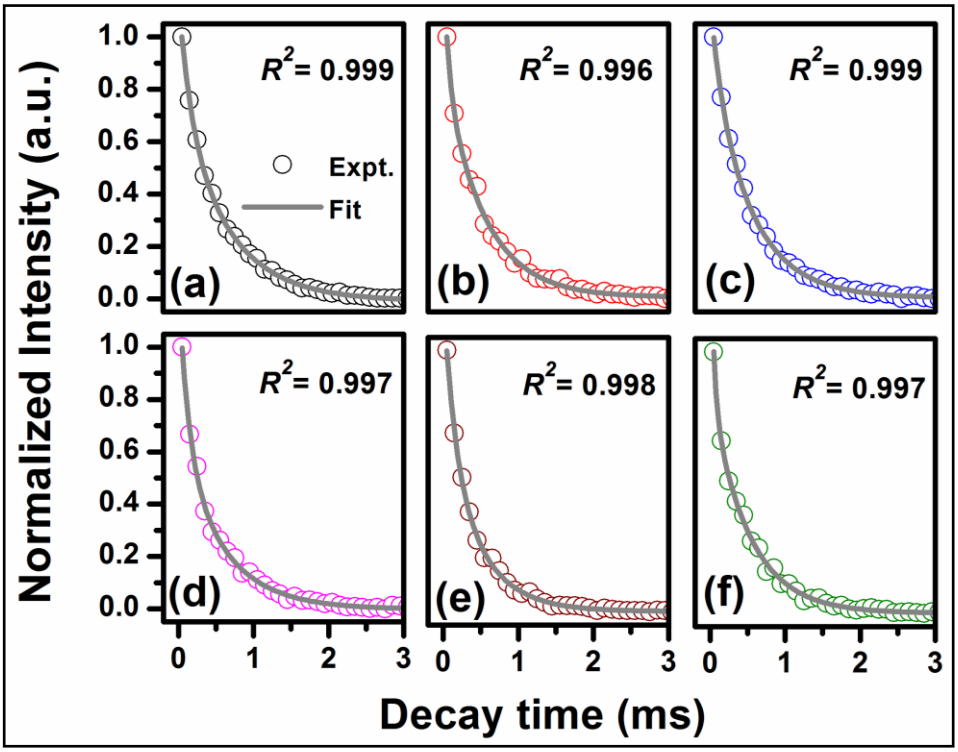


***Figure 5.8*** *Time resolved luminescence decay curves of emission peak at 577 nm corresponding to $Dy^{3+}$ ion monitored after exciting at a wavelength of 393 nm for different Sm concentrations. (**a-f** correspond to D0.5S0, D0.5S0.1, D0.5S0.3, D0.5S0.5, D0.5S1, and D0.5S2, respectively).*

a result, the different local environments around RE active ions can give rise to different luminescence decay behavior.[175, 176] In general, luminescence decay curve is fitted using single-exponential function given as $I(t) = I_0 e^{-t/\tau}$ where $I_0$ and $I$ are luminescence

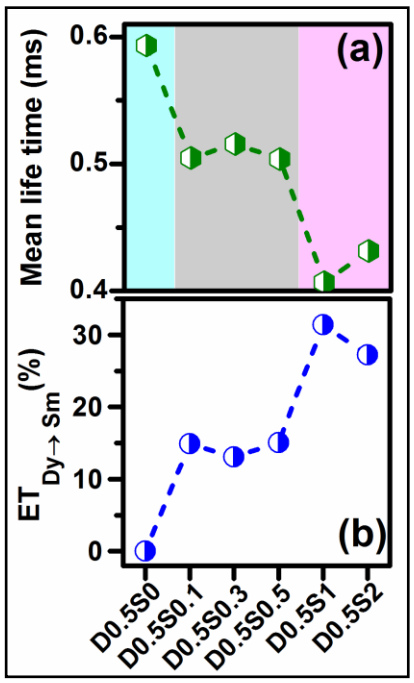


***Figure 5.9*** *Variation in* ***(a)*** *mean lifetime and* ***(b)*** *efficiency of energy transfer from* $Dy^{3+}$ *to* $Sm^{3+}$ *ion as a function of Sm concentration.*

intensity measured at 0 and at an instant, *t*, respectively and $\tau$ is the resulted lifetime. For Dy and Sm codoped $HfO_2$, in contrast to single exponential fitting, a double-exponential function, $I(t) = I_1 e^{-t/\tau_1} + I_2 e^{-t/\tau_2}$ fits well with the experimental data. The parameters, *I* is intensity corresponding to $Dy^{3+}$ ions, $I_1$ and $I_2$ are respective constants, $\tau_1$ and $\tau_2$ are known as characteristic lifetimes denoted as fast and slow decay components.[176] The calculated coefficient of determination (COD), $R^2$ values are found to be ~0.995 and ~0.999 for single and double exponential function fits, respectively. Hence, we have adopted a double-exponential function to fit all decay curves. After fitting experimental data, the extracted parameters like $I_1$, $I_2$, $\tau_1$ and $\tau_2$ have been utilized to estimate the mean lifetime ($\tau_m$) through following relation.[175]

$$\tau_m = (I_1\tau_1^2 + I_2\tau_2^2) / (I_1\tau_1 + I_2\tau_2)$$

The mean lifetimes are found to be in the range of ~0.59 to 0.43 ms for *x*Dy,*y*Sm:$HfO_2$ shown in **figure 5.9 (a)**. It is evident that $HfO_2$ nanoparticles doped with only $Dy^{3+}$ ion show longer lifetime value of ~0.6 ms. The estimated $\tau_m$ value agrees well with the reported value for $Dy^{3+}$ ion characteristic emission at 577 nm.[176, 177] However, after doping 0.1 at% of Sm, keeping Dy concentration fixed, $\tau_m$ decreases to ~0.5 ms which remains almost constant upto 0.5 at% of Sm. At 1 and 2 at% of Sm concentration, $\tau_m$ further shortens and reaches ~0.4 ms showing ~30% reduction in $\tau_m$ value. This fact indicates a more rapid decay of $Dy^{3+}$ ions with increasing Sm concentration which could be due to non-radiative transfer of energetic electrons from $Dy^{3+}$ to $Sm^{3+}$ active ions. Considering the existence of an energy exchange between $Dy^{3+}$ and $Sm^{3+}$ active ions, the efficiency of energy transfer (ET) is related to activator ion lifetime expressed as follows.[178]

$$(ET)_{Dy\rightarrow Sm} = 1 - (\tau_{Dy}'/\tau_{Dy})$$

where $\tau_{Dy}'$ and $\tau_{Dy}$ are lifetimes of sensitizer i.e. $Dy^{3+}$ ions in presence and absence of $Sm^{3+}$ ions, respectively. The variation in calculated efficiency of energy transfer from $Dy^{3+}$ to $Sm^{3+}$ ions with increasing Sm concentration depicted in **figure 5.9 (b)** shows that $(ET)_{Dy\rightarrow Sm}$ enhances with increasing Sm concentration. A maximum of ~30% energy is being transferred from $Dy^{3+}$ to $Sm^{3+}$ ions when Sm concentration reaches upto 2 at%.

In order to realize $Dy^{3+}$ and $Sm^{3+}$ interaction process, we discuss the energy transfer mechanism after calculating the distance between two neighboring active ions pairs such as $Dy^{3+} - Dy^{3+}$, $Dy^{3+} - Sm^{3+}$ or $Sm^{3+} - Sm^{3+}$ using following expression.[179]

$$R = (M_{HfO_2}/N_A \rho C)^{1/3}$$

| **Sample** | **Average Distance, *R* (Å)** | | |
|---|---|---|---|
| | **$Dy^{3+}$–$Dy^{3+}$** | **$Dy^{3+}$–$Sm^{3+}$** | **$Sm^{3+}$–$Sm^{3+}$** |
| D0.5S0 | 19.18 | - | - |
| D0.5S0.1 | 19.18 | 18.06 | 32.63 |
| D0.5S0.3 | 19.18 | 16.43 | 22.71 |
| D0.5S0.5 | 19.18 | 15.26 | 19.18 |
| D0.5S1 | 19.18 | 13.36 | 15.25 |
| D0.5S2 | 19.18 | 11.27 | 12.15 |

***Table 5.2*** *The average distance (R) between different neighboring ion pairs for varying Sm concentration in $HfO_2$ nanoparticles.*

where *R* is the distance between two adjacent active ions, *C* is total concentration of $Dy^{3+}$ and/or $Sm^{3+}$ ions, $N_A$ is Avogadro number, $M_{HfO_2}$ is molecular weight and $\rho$ is the density (9.7 g/$cm^3$) of of host $HfO_2$, respectively. The estimated average values of *R* at different concentrations of Sm are listed in **Table 5.2**. The average *R* value varies from ~18.1 to 11.3 and ~32.6 to 12.2 Å for $Dy^{3+}$ − $Sm^{3+}$ and $Sm^{3+}$ − $Sm^{3+}$ ion pairs, respectively. On the basis of above results, it can be inferred that at low Sm concentrations (0.1-0.5 at%), $Sm^{3+}$ ions are located far from adjacent $Dy^{3+}$ or $Sm^{3+}$ active ion and sparsely distributed in $HfO_2$ lattice acting as isolated luminescent centers. As a consequence, a few excited electrons transfer from sensitizer $Dy^{3+}$ to $Sm^{3+}$ ion diminishing the sensitizer lifetime appreciably. After increasing Sm concentration upto 2 at%, *R* value further decreases and activator ions such as $Dy^{3+}$ and $Sm^{3+}$ form pairs which essentially evoke transfer of more and more electrons from sensitizer to Sm active ions enhancing photoluminescence properties. Further, in order to determine the process by which the energy is being transferred from sensitizer to activator ion, two processes/mechanisms are suggested (i) exchange

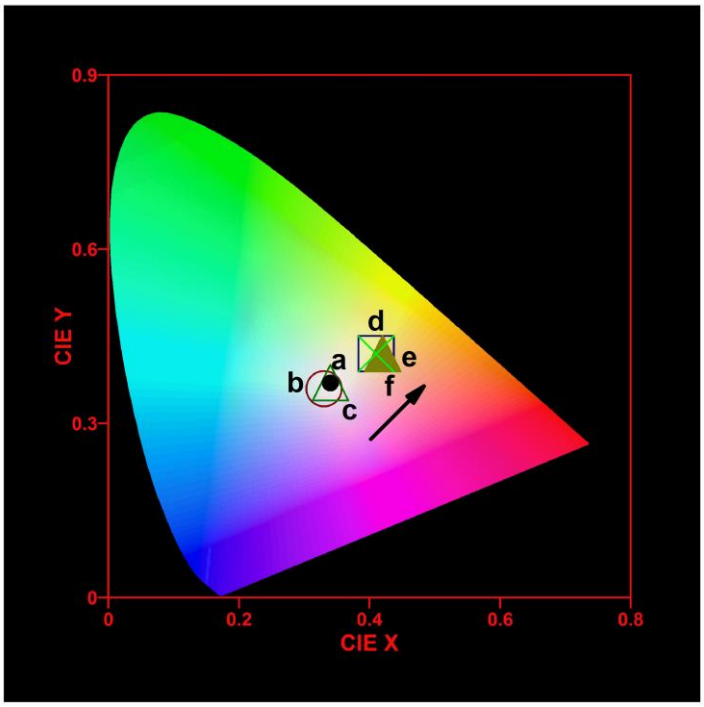


***Figure 5.10*** *CIE chromaticity diagram of xDy,ySm:$HfO_2$ nanoparticles after exciting with a wavelength of 393 nm. (**a-f** correspond to D0.5S0, D0.5S0.1, D0.5S0.3, D0.5S0.5, D0.5S1, and D0.5S2, respectively)*

interaction and (ii) multipolar interaction process.[180] Depending on the critical distance between sensitizer and activator ion, one of two processes become dominant and contribute in energy transfer mechanism. It is established that at a critical distance below 5 - 6 Å, the energy is transferred predominantly through an exchange interaction process.[179, 180] However, in our case, the calculated *R* values are well above 6 Å. This reveals that multipolar interaction prevails over exchange interaction type mechanism and governs the existing energy transfer process from sensitizer $Dy^{3+}$ to $Sm^{3+}$ active ions in $HfO_2$ nanoparticles. A two dimensional Commission Internationale de I'Eclairage 1931 (CIE xy) chromaticity diagram for *x*Dy,*y*Sm:$HfO_2$ nanoparticleswith varying Sm concentration obtained after exciting with wavelength of 393 nm is shown in **figure 5.10**. The CIE coordinates are estimated as (0.35,0.37), (0.33,0.36), (0.34,0.37), (0.41,0.42), (0.42,0.42)

and (0.41,0.41) for *x*Dy,*y*Sm:$HfO_2$, respectively. It can be noted that at low concentrations, *x*=0.5 and *y*=0.1 and 0.3 at %, CIE coordinates are almost similar rendering near white light emission. However, at higher concentration of Sm, $HfO_2$ produces purplish light color due to significant contribution from $Sm^{3+}$ ion characteristic emissions emerging along with $Dy^{3+}$ emission peaks.

### 5.2.5 Energy Band Diagram

On the basis of excitation, emission and time resolved luminescence decay spectra, we, herein suggest a simplified schematic energy level diagram to realize different processes involved in $Dy^{3+}$ and $Sm^{3+}$ coactivated $HfO_2$ nanoparticles (**figure 5.11**). The respective energy levels of $Dy^{3+}$ ion such as $^6H_{11/2}$, $^6H_{13/2}$, $^6H_{15/2}$, $^4F_{9/2}$, $^4I_{13/2}$, $^4F_{7/2}$, $^6P_{5/2}$, $^6P_{7/2}$, $^6P_{3/2}$ and $^4I_{9/2}$ and$^6P_{3/2}$, $^4I_{13/2}$, $^4G_{5/2}$, $^6H_{5/2}$, $^6H_{5/2}$, $^6H_{5/2}$ corresponding to $Sm^{3+}$ ion are labeled. Due to wide band gap (~5.7 eV) of host, $HfO_2$, electrons can only reach to specific energy levels of activator ions after exciting with a wavelength of 393 nm i.e. lower energy. Upon excitation under a wavelength of 393 nm, electrons at ground state, $^6H_{15/2}$, absorb the pumping energy and get populated at higher energy level, $^4I_{13/2}$ of $Dy^{3+}$ ion. Afterwards, excited electrons follow a multistep nonradiative relaxation to a metastable state, $^4F_{9/2}$ and while finally arriving at ground states such as $^6H_{15/2}$ and $^6H_{13/2}$ induce intense emissions at 490 and 577 nm corresponding to $Dy^{3+}$. However, in the presence of $Sm^{3+}$ ion, characteristic emissions due to electronic transitions from excited state, $^4G_{5/2}$ to ground state of $Sm^{3+}$, $^6H_{7/2}$ produce a set of emission peaks at 600-640 nm along with $Dy^{3+}$ emissions. These emission peaks become stronger as the efficiency of energy transfer enhances considerably with increasing Sm concentration in $HfO_2$.

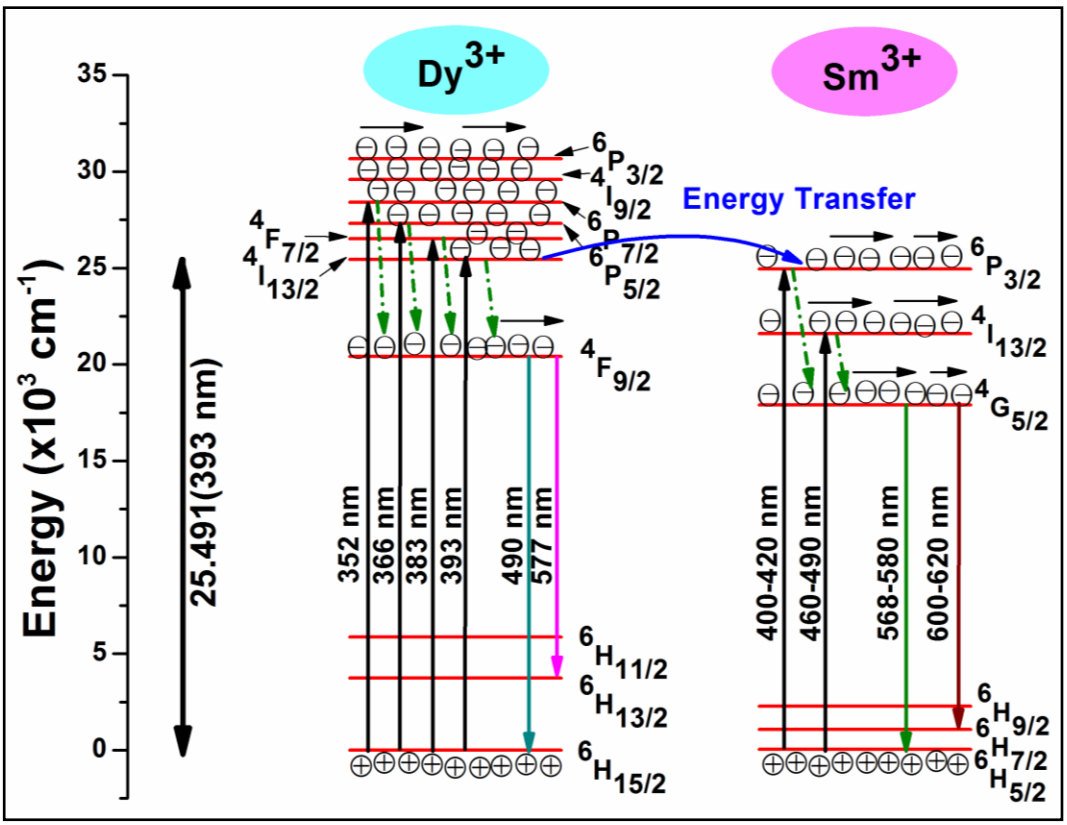


***Figure 5.11*** *A simplified schematic energy level diagram demonstrating different emission, excitation processes and energy transfer in Dy and Sm codoped $HfO_2$ nanoparticles.*

Such an observation of simultaneous emissions from $Dy^{3+}$ and $Sm^{3+}$ ion is realized because of significant energy exchange through multipolar interaction between different energy levels of both activator ions. Since excited energy level, $^4I_{13/2}$ of sensitizer $Dy^{3+}$ and $^6P_{3/2}$ corresponding to $Sm^{3+}$ active ion lie within close regime, electrons populated at these levels can reciprocate easily to produce characteristic emissions. The higher levels of sensitizer $Dy^{3+}$ ion such as $^6P_{7/2}$ and $^6P_{5/2}$ do not participate in such energy exchange process due to appreciably large energy separation between $Dy^{3+}$ excited and $Sm^{3+}$ emission levels. Therefore, it can be concluded that in $Dy^{3+}$ and $Sm^{3+}$ coactivated $HfO_2$ nanoparticles, the energy transfer from $Dy^{3+}$ is possible only between excited levels lying in close proximity of $Sm^{3+}$ energy levels which can remarkably tune the photoluminescence

properties furnishing desired optical performance. Looking at promising luminescence properties, we have exploited the synthesized nanoparticles for application in latent fingerprint imaging.

### 5.2.6 Application in Latent Fingerprint Imaging

Using $Dy^{3+}$ and $Sm^{3+}$ coactivated $HfO_2$ nanoparticles, we demonstrate a proof of concept for detecting latent fingerprints on different object surfaces. In general, human finger skin is covered with lipid substances insoluble in water and leave practically invisible marks upon object surfaces when touched.[181] In practice, a good contrast between fingerprint impression and substrate background is sought after for LFPs development with highly detailed and distinct features for an individual identification. In addition, a better adherence of labeling powder with ridges present in fingerprint patterns is a prerequisite and equally important.[182, 183] For an effective, fast, and hassle free development of LFPs, a step by step procedure is followed as depicted schematically in **figure 5.12**. First, the left hand thumb finger of donor to be marked is washed properly with soap solution and dried under hot air blower. LFPs are obtained by gently pressing thumb over thoroughly clean surface of different objects such as transparent glass, aluminum foil, colored plastic sheets, and stainless steel. The synthesized Dy and Sm codoped $HfO_2$ has been utilized as proposed dusting or labeling powder and sprinkled onto object surface containing LFPs. Any excess amount of powder is then blown-off which revealed undistinguished and vague fingerprint under bright light environment. However, under long UV light of 395 nm irradiation, LFPs become completely visible demonstrating a well defined and distinguishable fingerprint ridge pattern. Finally, a digital camera was

used to capture the photographs of LFPs developed after sprinkling Dy and Sm codoped $HfO_2$ powder.

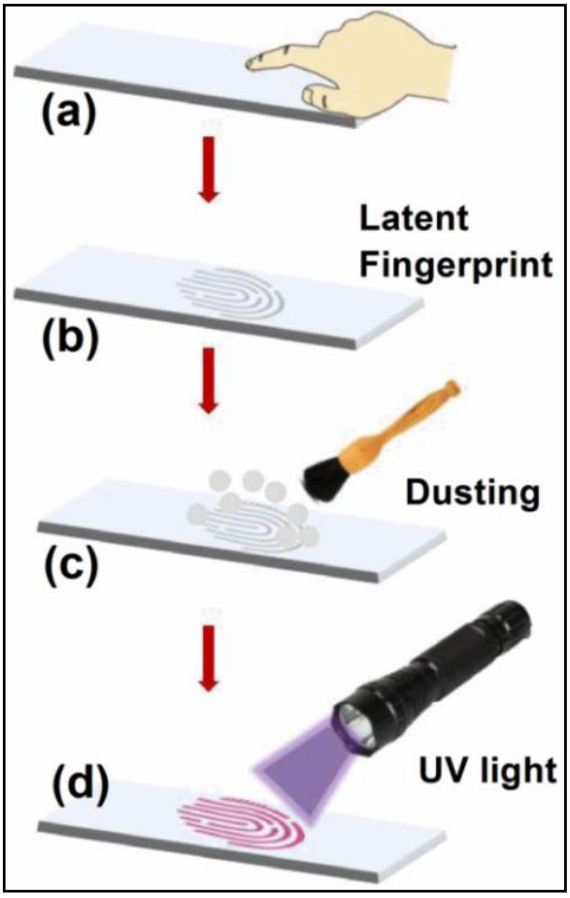


***Figure 5.12*** *An illustration of the process flow adopted for developing latent fingerprint using Dy and Sm coactivated $HfO_2$ powders* ***(a)*** *printing finger impression on a substrate,* ***(b)*** *latent fingerprint,* ***(c)*** *dusting using synthesized powders and* ***(d)*** *exposure under ultra-violet (UV) light of 395 nm.*

**Figure 5.13 (a), (b) and (c)** compares fresh LFPs impressions onto transparent glass, LFPs after D0.5S2 powder labeling in bright light condition and under 395 nm UV illumination, respectively. The fresh fingerprint impression on glass substrate is completely invisible to naked eye. However, in bright light environment (**figure 5.13 (b)**), the stained

latent fingerprint appears ambiguous to naked eyes and it is difficult to realize the whole fingerprint impression distinctively. Interestingly, under irradiation using a handheld 395 nm UV light (**figure 5.13(c)**), a complete fingerprint pattern is clearly recognized with discrete ridge shaped pattern. This observation confirms a good adsorption efficiency of $Dy^{3+}$ and $Sm^{3+}$ coactivated $HfO_2$ nanoparticles with ridges of fingerprint on a glass surface.

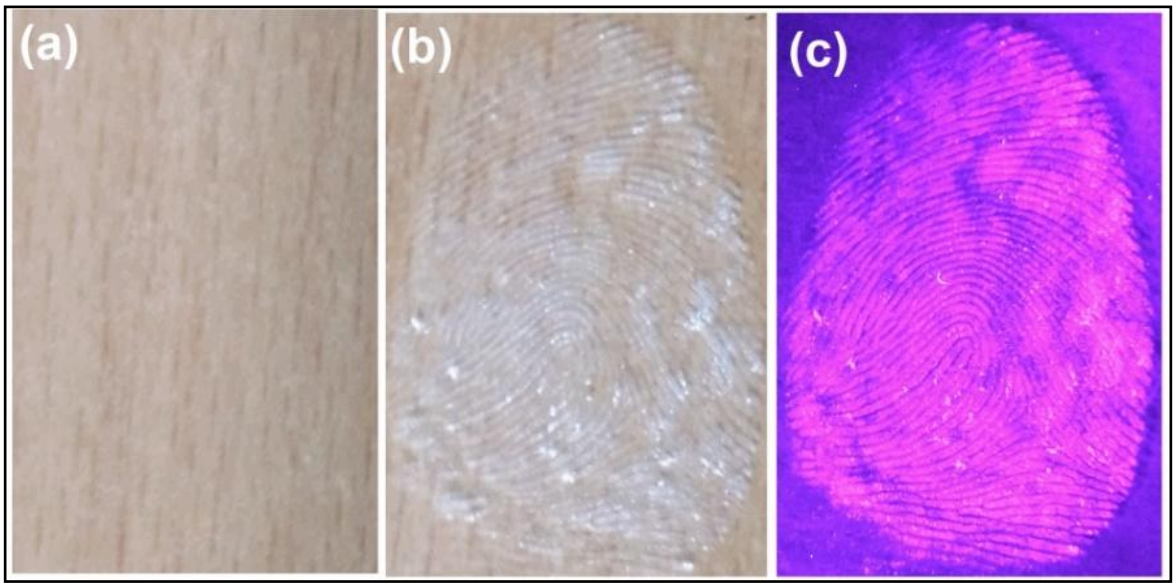


***Figure 5.13*** *An illustrative comparison of developed latent fingerprints marked over transparent glass surface sprinkled with $Dy^{3+}$ and $Sm^{3+}$ coactivated $HfO_2$ nanoparticles* ***(a)*** *LFP over glass* ***(b)*** *LFP after dusting in bright light environment and* ***(b)*** *under illumination of UV light (395 nm).*

To determine the viability and developing selectivity, we investigate the adsorption capability and performance of $Dy^{3+}$ and $Sm^{3+}$ coactivated $HfO_2$ nanoparticles labeled latent fingerprints marked onto common household object surfaces such as transparent glass, plastic sheet and stainless steel etc. **Figure 5.14 (a-f)** show LFPs imaging developed using D0.5S2 powder and then observed under illumination of 395 UV light upon aluminum foil,

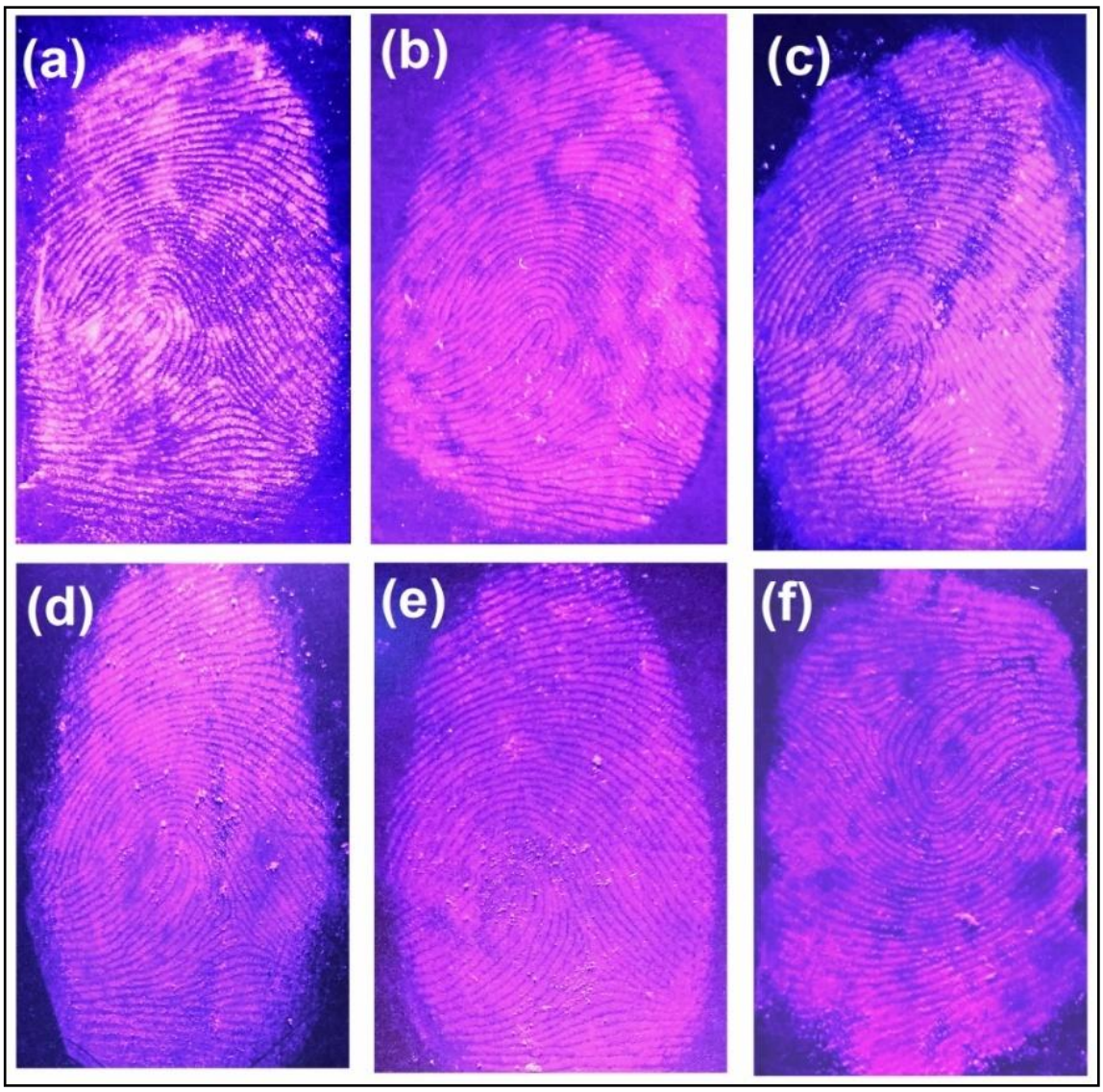


***Figure 5.14*** *The optical images of latent fingerprints developed using $Dy^{3+}$ and $Sm^{3+}$ coactivated $HfO_2$ nanophosphors and detected under 395 nm UV irradiation:* ***(a)*** *aluminum foil,* ***(b)*** *transparent glass,* ***(c)*** *black colored glass,* ***(d)*** *wine colored,* ***(e)*** *red colored plastic sheets and* ***(f)*** *stainless steel.*

transparent glass, black colored glass, wine and red colored plastic sheets and stainless steel, respectively. All LFPs images developed over different surfaces reveal lucid and bright fingerprint impressions containing a full ridge flow and pattern. A sufficiently distinguished and well defined appearance of developed LFPs with an explicit ridge pattern

demonstrate a high contrast with background and excellent resolution of imaged fingerprints. In order to achieve a high developing selectivity of latent fingerprints, an enough color contrast between luminescent powders and background is desirable.[184]

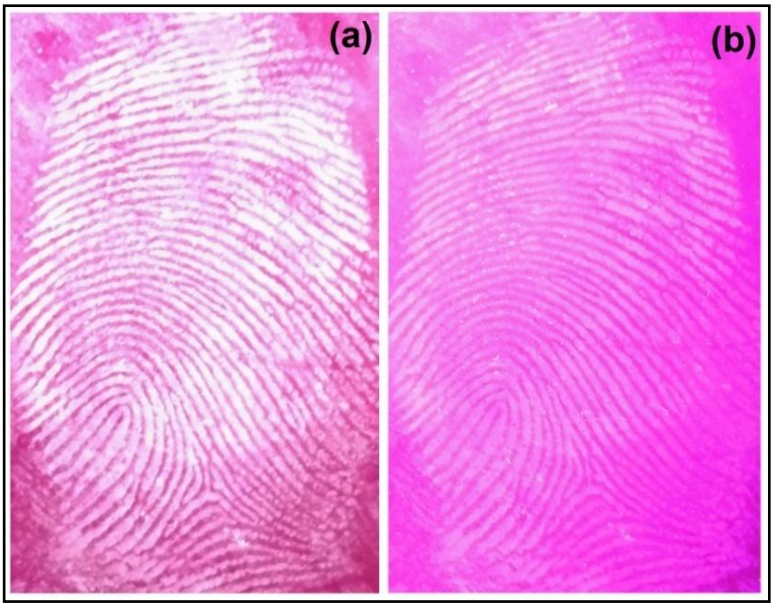


***Figure 5.15*** *A comparison of LFPs images developed using D0.5S2 powder over purplish colored surface recorded* ***(a)*** *in bright light environment and* ***(b)*** *under 395 nm UV irradiation.*

Nevertheless, latent fingerprints impressions labeled with $Dy^{3+}$ and $Sm^{3+}$ coactivated $HfO_2$ nanoparticles under 395 nm UV exposure examined over various object surfaces maintained an appropriate resolution, less interference with background and suitable color contrast for extracting minute details to identify an individual. Further, we have examined the purplish colored surface background interference with developed LFPs (**figure 5.15**). The result indicates minor background interference with an acceptable resolution revealing minute characteristic details. In present investigations on LFPs recognition, all fingerprint impressions formed onto object surfaces are enriched essentially with sweat or sebum. It is

known that adsorption efficiency of powders onto fingerprint is dependent on adhesive bond formation between powder particles and ridges of fingerprint.[185, 186] The luminescent dusting powders constituting of smaller particle size provide a better degree of adhesion with most of the object surfaces. The mechanical adhesion process is explained in terms of pressure deficiency produced among powder particle and a ridge within fingerprint.[181] Owing to nanorange particle size (~15 nm) of $Dy^{3+}$ and $Sm^{3+}$ coactivated $HfO_2$ nanoparticles, the synthesized luminescent powder offers superior adsorption capability for developing LFPs.

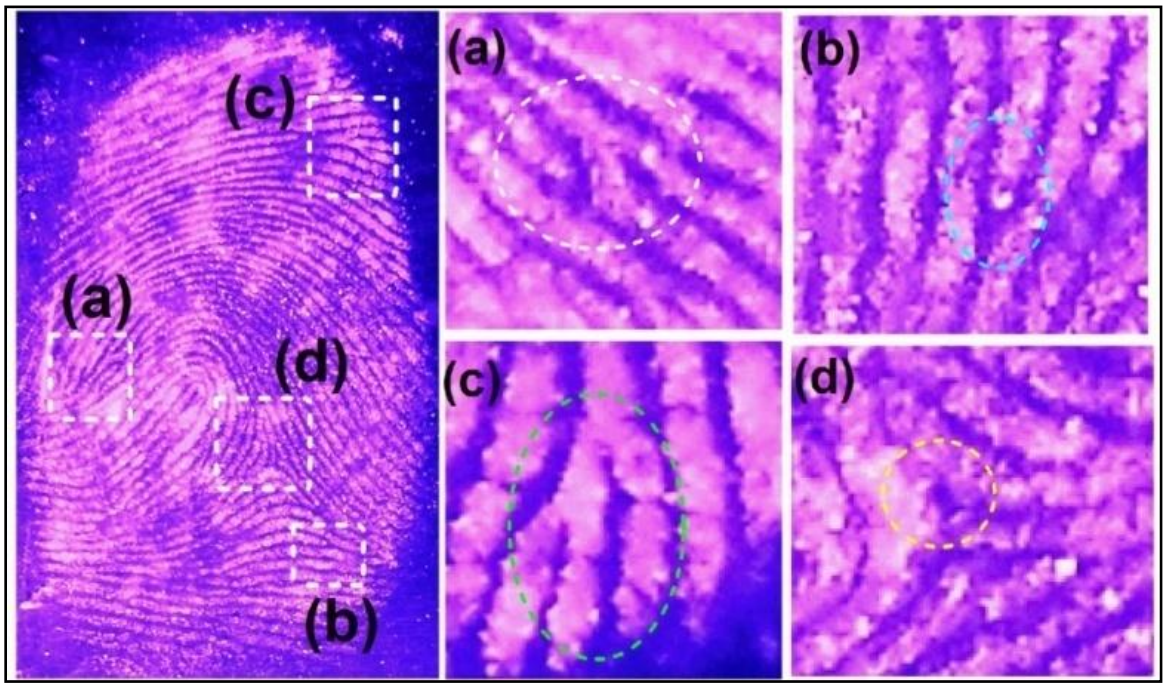


***Figure 5.16*** *The developed latent fingerprint over aluminum foil labeled by $Dy^{3+}$ and $Sm^{3+}$ coactivated $HfO_2$ nanophosphors showing selected magnified regions with third-level details distinctive to an individual such as (a) termination along with single bifurcation, (b) termination of a ridge, (c) a crucial double bifurcation and (d) an enclosure.*

**Figure 5.16** depicts a typical fingerprint on aluminum foil substrate labeled with $Dy^{3+}$ and $Sm^{3+}$ coactivated $HfO_2$ nanoparticles along with four highlighted enlarged regions of investigation. The specified sections, **figure 5.16 (a-d)** demonstrate the existence of a termination along with single bifurcation, termination of a ridge, a crucial double bifurcation and an enclosure, respectively. Such third-level details of a fingerprint remain distinguishable even after magnification. These distinct features are very crucial and eventually utilized for identifying an individual easily.[187, 188] In consideration to above observations, one can conclude that $Dy^{3+}$ and $Sm^{3+}$ coactivated $HfO_2$ nanoparticles is proficient at developing clear latent fingerprints over different household object surfaces. Under 395 nm UV irradiation, Dy and Sm codoped $HfO_2$ developed LFPs show full ridge flow and pattern with characteristic features comparable to LFPs labeled with $NaYF_4$:Yb,Er; $YVO_4$:Eu and $LaPO_4$:Ce,Tb powders imaged under 980 nm NIR or 254 nm deep UV irradiation, respectively. A fine nature of prepared nanoparticles guarantees a high stability against fingerprints marked onto variable surfaces. Thereby, the developed fingerprints comprise of well resolved and comprehensible minutiae details e.g. ridge termination, bifurcations and enclosures useful for hassle-free individual identification process. Since $Dy^{3+}$ and $Sm^{3+}$ coactivated $HfO_2$ nanoparticles are non-hazardous, it is more appropriate to be employed in LFPs imaging with good developing selectivity and sensitivity.

## 5.3 Conclusions

To summarize, after codoping Dy and Sm upto the total concentration of 13 at%, we successfully demonstrated the stabilization of high temperature cubic phase of $HfO_2$ at room temperature. The robustness of luminescent Dy and Sm codoped $HfO_2$ nanoparticles

was investigated as a prospective dusting powder for an effective development of latent fingerprints. Dy and Sm codoped $HfO_2$ having low dopant concentration showed only the monoclinic phase of $HfO_2$ as observed by XRD, Le-Bail profile fitting and selected area electron diffraction pattern. With increasing Sm concentration, the crystallite size decreased significantly from ~25 to ~10 nm leading to an exponential enhancement of cell volume essentially due to negative pressure effect manifested by nanosize characteristic of the particles. Detailed photoluminescence studies demonstrated that under an excitation wavelength of 393 nm, Dy and Sm codoped $HfO_2$ revealed prominent emission peaks in blue, yellow and near red spectral regions producing purplish colored light. A systematic study of the time resolved decay spectra confirmed the existence of an energy transfer from $Dy^{3+}$ to $Sm^{3+}$ ions occurring via a multipolar interaction which eventually induced excellent emissions from Dy and Sm coactivated $HfO_2$. On the basis of excitation and emission spectra, we proposed an energy band diagram to perceive different allowed electronic transitions. Dy and Sm coactivated $HfO_2$ nanophosphors were successfully applied as a versatile luminescent powder for selective LFPs imaging. The developed LFPs onto several surfaces including aluminum foil, float glass, black colored glass, wine and red colored plastic sheets and stainless steel exhibited third-level details, good background contrast, selectivity and resolution. The effectiveness of non-hazardous luminescent powders in detecting LFPs was realized due to nanosize nature of particles with improved adsorption capability.

# Chapter 6

## 6.1 Introduction

This chapter investigates the evolution of structure and resistive switching behavior in pristine and Sm, Dy doped $HfO_2$ thin films. The grazing incidence X-ray diffraction (GIXRD) reveals that while pristine film exhibits the monoclinic phase of $HfO_2$, the high temperature cubic phase is stabilized at room temperature in Sm and Dy doped $HfO_2$ films after doping almost half of the concentration compared to 12 at% of Sm or 11 at% of Dy in $HfO_2$nanoparticles reported by us.[189, 190] The fabricated $HfO_2$ based RRAM devices exhibit the bipolar forming-free resistive switching behavior. The role of oxygen vacancy formation in the stabilization of cubic phase as well as the resistive switching behavior in Sm and Dy doped $HfO_2$films are discussed.

## 6.2 Results and Discussion

### 6.2.1 X-ray Reflectivity and Phase transformation

**Figure 6.1 (a-c)** depict XRR data of $HfO_2$, Sm:$HfO_2$ and Dy:$HfO_2$, respectively. In order to evaluate the film density and thickness, XRR data have been fitted with suitable stack models using Parratt software. In XRR pattern, the thickness and density are estimated from the critical angle for external reflection and period of the oscillations, respectively. The fittings show that the observed data and simulated curves are in good agreement in case of all thin films. For $HfO_2$, Sm:$HfO_2$ and Dy:$HfO_2$ films, the thickness is estimated as ~59.8, 59 and 58 nm, respectively. The film density is found to be 9.2, 8.4 and 8.1 g/cm$^3$ corresponding to $HfO_2$, Sm:$HfO_2$ and Dy:$HfO_2$ films, respectively. In addition,

from EDS spectra, the atomic concentrations of Sm and Dy ions are found to be ~5.56 and ~4.46 at% in Sm and Dy doped $HfO_2$ films, respectively (**figure 6.2**).

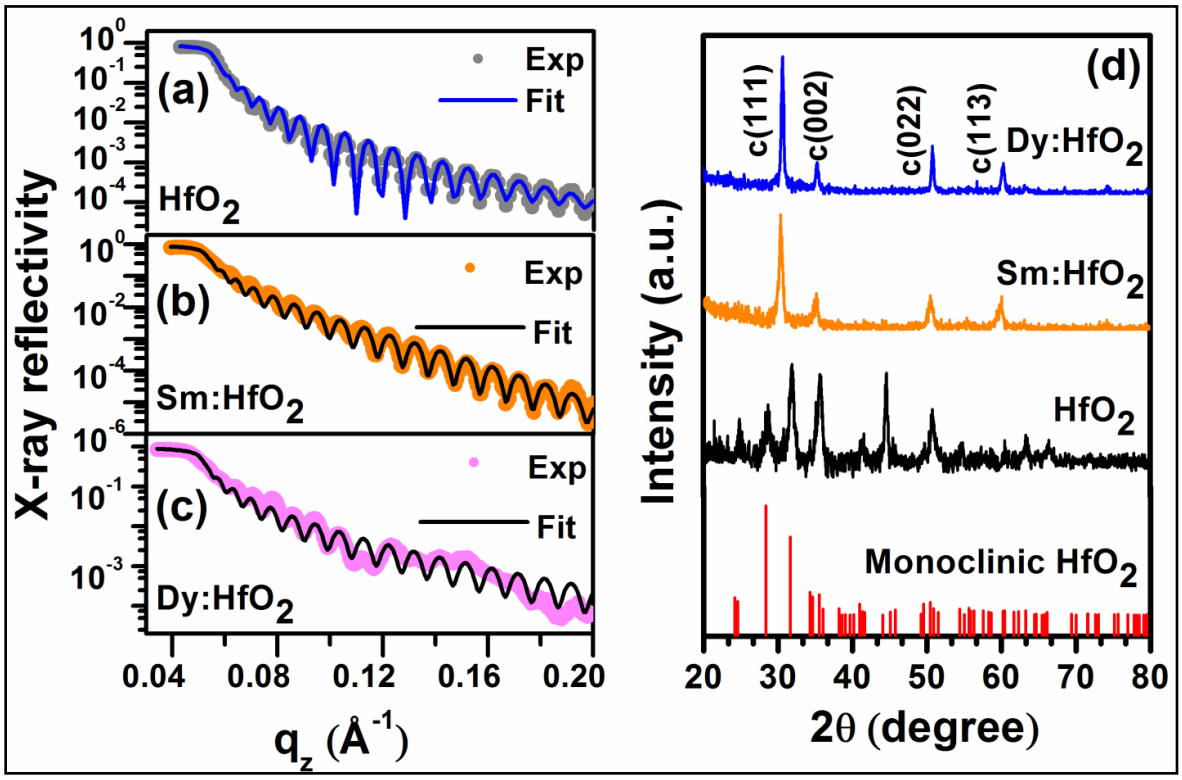


***Figure 6.1*** *X-ray reflectivity of* ***(a)*** *$HfO_2$,* ***(b)*** *Sm: $HfO_2$ and,* ***(c)*** *Dy:$HfO_2$;* ***(d)*** *GIXRD patterns of $HfO_2$, Sm:$HfO_2$ and Dy:$HfO_2$ films.*

The GIXRD patterns of $HfO_2$, Dy:$HfO_2$ and Sm:$HfO_2$ films annealed at 550 $^0$C are depicted in **figure 1 (d)**. The presence of sharp diffraction peaks specify the crystalline nature of the films.For $HfO_2$, the diffraction peaks identified as (110), ($\bar{1}$11), (111), (020), (200), (021), ($\bar{2}$11) and(112) are well matched with the monoclinic phase of $HfO_2$, space group, $P2_1/c$ (JCPDS card no. 78-0049). However, after incorporating Sm or Dy, the observed peaks such as (111), (002), (022) and (113) are attributed to cubic phase of $HfO_2$,

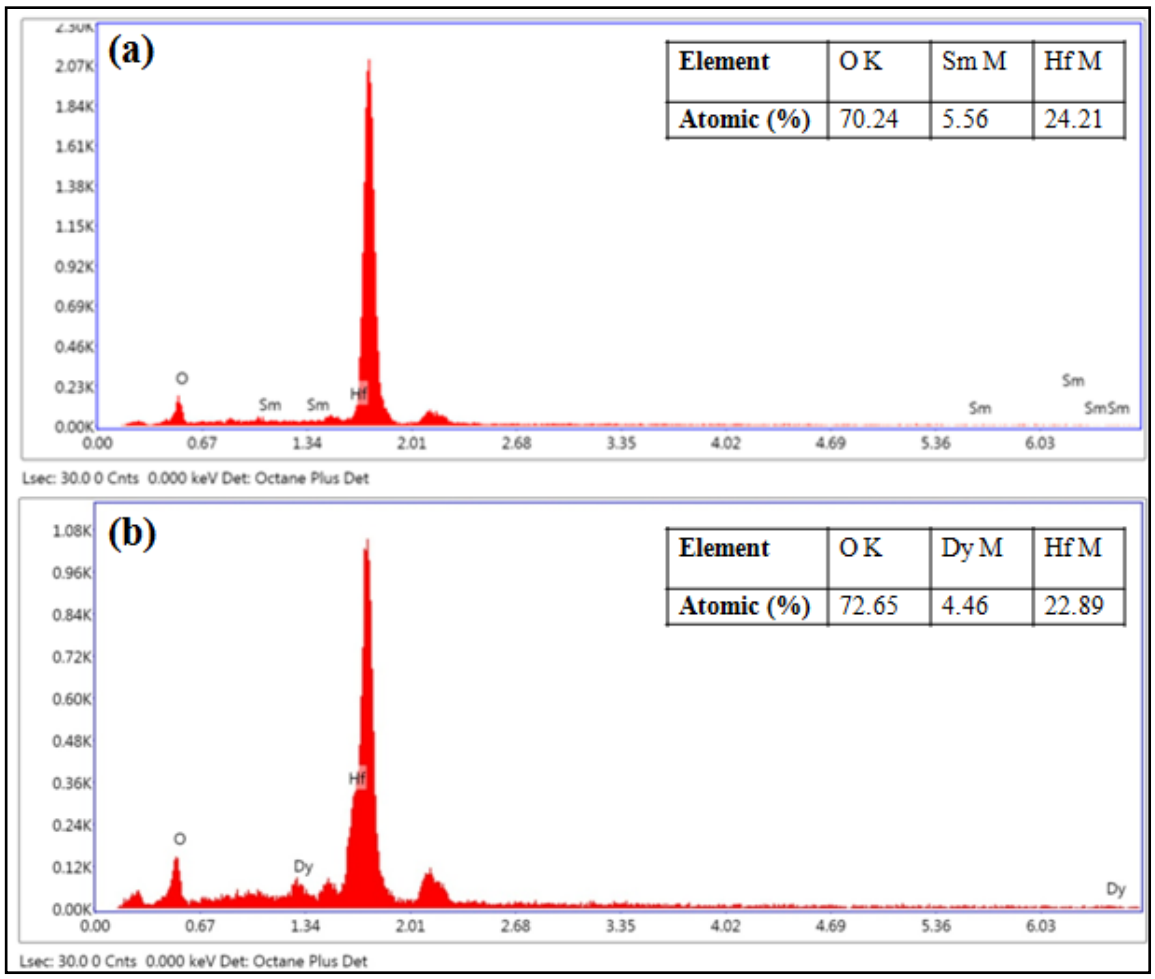


***Figure 6.2*** *EDS spectra for* ***(a)****Sm:$HfO_2$ and* ***(b)*** *Dy:$HfO_2$ films annealed at 550 $^0$C.*

space group, $Fm\bar{3}m$ (JCPDS card no. 53-0560). Absence of secondary phase indicates that $Dy^{3+}$ and $Sm^{3+}$ ions substitute at $Hf^{4+}$ site of $HfO_2$ lattice. Surprisingly, in Sm/Dy doped $HfO_2$ films, the high temperature cubic phase is stabilized at room temperature. Earlier, we have reported the stabilization of cubic phase at RT by incorporating 12 at% of Sm or 11 at% of Dy in $HfO_2$ nanoparticles. Here, the cubic phase is stabilized at most half concentration of these dopants in $HfO_2$ films compared to nanoparticles. In particular, the monoclinic to cubic phase transformation is explained considering the difference in ionic radii and oxidation states of $Dy^{3+}$, $Sm^{3+}$ and $Hf^{4+}$ ions resulting in formation of oxygen

vacancies.[189] It is well-known that the coordination numbers of $Hf^{4+}$ ion in the monoclinic and cubic phase are 7 and 8, respectively.[66] When $Sm^{3+}$ or $Dy^{3+}$ replace $Hf^{4+}$ ion, the oxygen vacancies are produced near dopant sites in $HfO_2$ lattice resulting in 8-fold oxygen coordination to dopant ions thereby stabilizing the cubic phase of $HfO_2$ at room temperature.

### 6.2.2 X-ray Photoelectron Spectroscopy

Therefore, we study the role of oxygen vacancy concentration in the stabilization of cubic phase of $HfO_2$ by means of XPS technique. **Figure 6.3 (a-c)** show XPS spectra of Hf 4*f* core levels for $HfO_2$, Dy:$HfO_2$ and Sm:$HfO_2$ films. The spectra are first corrected with respect to the C 1*s* peak located at ~284.6 eV. Hf 4*f* spectra have been deconvoluted into two peaks fitted with mixed Gaussian and Lorentzian functions using XPSPEAK version 4.1. The two peaks are found to be located at ~16.2 and ~17.9 eV associated to Hf $4f_{7/2}$ and Hf $4f_{5/2}$, respectively.[105] XPS spectra of O 1*s* are demonstrated in **figure 6.3 (a'-c')**. Due to asymmetric shape of the spectra, we have deconvoluted the spectra into two peaks named as Peak 1 and 2 found to be centered at ~530 and ~531 eV, respectively. In low binding energy (B.E) region, the peak at ~530 eV is ascribed to lattice oxygen atoms in Hf-O bonds whereas the high B.E peak at ~531 eV is attributed to oxygen deficient regions exhibiting oxygen vacancies and $O_2^-$ ions in Si-O bonds.[66, 190] The area ratio under peak 2 and 1 i.e. ($A_2/A_1$) is found to be 0.60, 0.87 and 0.93 in $HfO_2$, Sm:$HfO_2$ and Dy:$HfO_2$ films, respectively. Although the oxygen vacancies exist in monoclinic phase $HfO_2$film, the notable increase in $A_2/A_1$ for Sm and Dy doped $HfO_2$ films thereby induce more and more oxygen vacancies in $HfO_2$ lattice. Thus, it is confirmed that an appropriate concentration of

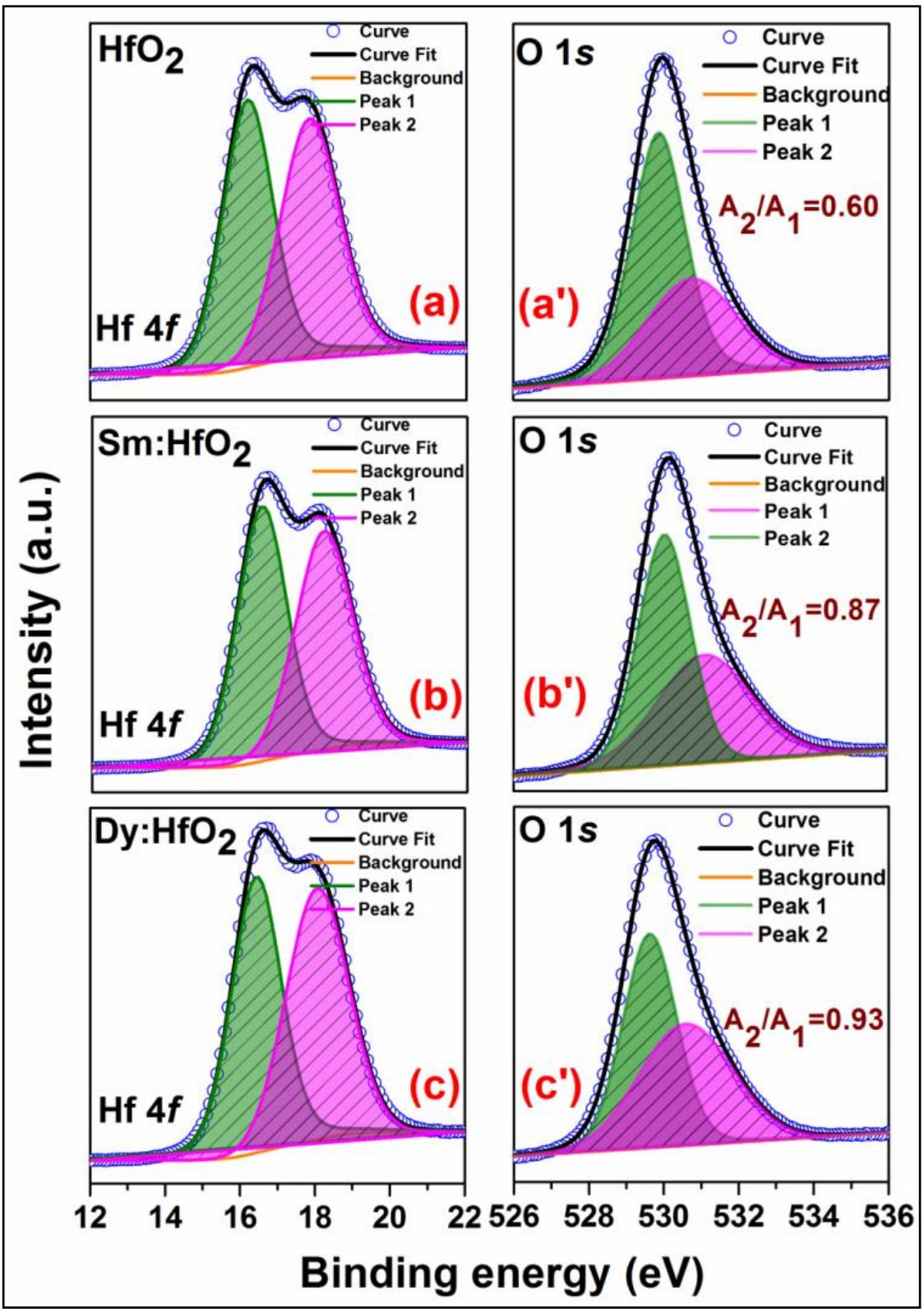


***Figure 6.3*** *The XPS spectra of Hf 4f and O1s core levels for* ***(a,a')*** *$HfO_2$,* ***(b,b')*** *Sm:$HfO_2$ and* ***(c,c')*** *Dy:$HfO_2$, respectively.*

oxygen vacancies are present in the host lattice which facilitate the stabilization of cubic phase in Sm and Dy doped $HfO_2$ film. Owing to abundance of oxygen vacancy, these films are explored for RRAM device application.

### 6.2.3 Current-Voltage (*I-V*) Characteristics

We investigate the resistive switching behavior of $HfO_2$ based RRAM using the semi-logarithmic current-voltage (*I-V*) characteristic curves for $HfO_2$, Sm:$HfO_2$ and Dy:$HfO_2$ thin film devices shown in **figure 6.4**. *I-V* measurements are performed after sweeping the applied DC bias voltage in a sequence of 0 V→ 4 V→ 0 V→ -5 V→ 0 V. During *I-V* measurements, the bottom electrode was grounded and the bias voltage applied to the top electrode. To avoid electrical breakdown of devices, the compliance current was fixed at 7 mA during switching measurements. At first stage (0→4 V), initially the value of current is very small indicating HRS or OFF-state and at a certain bias voltage known as SET voltage ($V_{SET}$), the current shows an abrupt enhancement indicating switching towards LRS or ON-state. Similarly, in negative bias voltage region (0→-5 V), the bias voltage at which the current decreases sharply is called as RESET voltage ($V_{RESET}$). The existence of positive $V_{SET}$ and negative $V_{RESET}$ confirms the distinct bipolar resistive switching behavior in our $HfO_2$ based RRAM devices. Interestingly, the resistive switching characteristic is of forming-free nature. $V_{SET}$ value is found to be ~3.7 V for monoclinic phase $HfO_2$ device whereas the cubic phase Sm:$HfO_2$ and Dy:$HfO_2$ RRAM exhibit ~3.2 and 2.8 V, respectively. Also, the separation between ON and OFF states estimated as approximately three is feasible for RRAM device.

To understand and obtain a detailed insight into SET and RESET mechanisms, we investigate different conduction models such as Schottky emission, Poole-Frenkel (P-F)

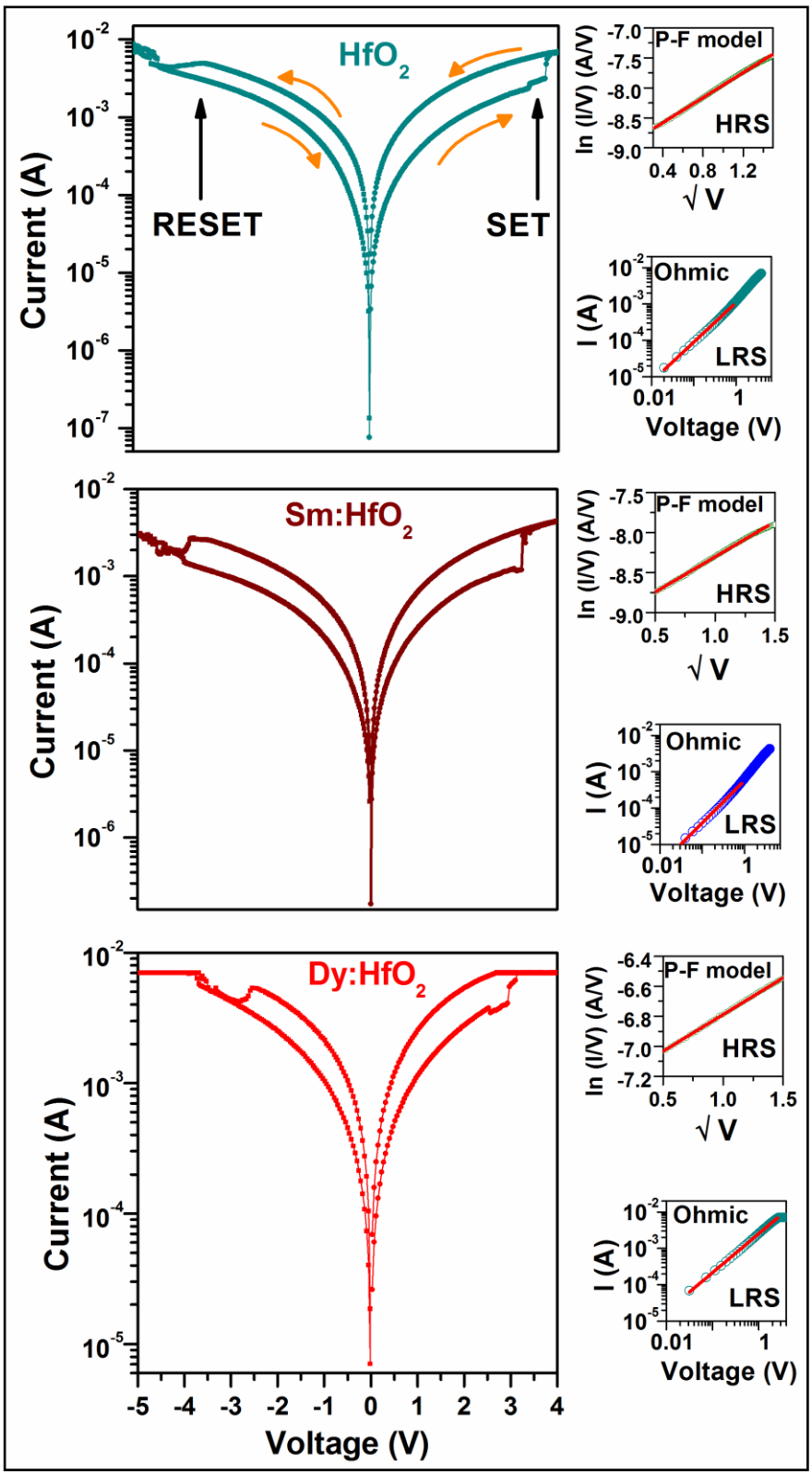


***Figure 6.4*** *Current-Voltage (I-V) characteristics in semi-logarithmic scale for $HfO_2$, Sm:$HfO_2$ and Dy:$HfO_2$.thin film devices. Insets show P-F and Ohmic model linear fits for HRS and LRS resistive states, respectively.*

emission, Ohmic conduction and Fowler-Nordheim (F-N) tunneling and space charge limited current (SCLC) in LRS and HRS states.[97] The current and voltage relationships for Ohmic conduction and P-F emission are given as $I= Ve^{-A/T}$ and $I=Ve^{\frac{q}{kT}(2a\sqrt{V-\phi_B})}$, respectively, where *A*is a constant, T is temperature, $a=\sqrt{q/4\pi\varepsilon_i d}$, $\varepsilon_i$ is electric field in dielectric, $d$ is the thickness of dielectric, $\phi_B$ is barrier height and $k$ is called as the Boltzmann constant.[191] The right panel of **figure 6.4**, for $HfO_2$ based RRAM, depicts fitting of *I-V* behavior in log-log scale confirming a linear relationship having slope of 1-1.2. This indicates that the Ohmic conduction is dominant in complete LRS state, however, the conduction behavior within low voltage regime for HRS state also follows only the Ohmic model. Ohmic conduction prevails when the thermally generated carrier density is sufficiently higher than that of the injected carrier density. Nevertheless, in case of high voltage regime of HRS, the conduction mechanism is somewhat different and does not follow a linear behavior. Such behavior can be perceived by applying the nonlinear conduction mechanism like P-F emission. The right panel of **figure 6.4** provides linear fits of *I-V* curves to P-F emission model in the high applied bias voltage region of HRS state. It is confirmed that P-F emission is the key conduction mechanism in high electric field range. P-F emission conduction occurs essentially due to the crystalline defects in $HfO_2$ films like single ($V_o^+$) or doubly ($V_o^{++}$) charged oxygen vacancies. This conduction mechanism is related to the trap assisted tunneling process inducing lowering of the voltage barrier which is a manifestation of the Coulomb attraction between the positively charged traps and negatively charged conduction electron into the conduction band.[192] Similar conduction mechanisms of Ohmic and P-F emission govern LRS and HRS in case of Sm and Dy:$HfO_2$ devices.

Further, the resistive switching behavior in RRAMs has been explained in terms of the formation of conductive filaments (CFs), migration of oxygen vacancies/ions, Schottky barrier and trapped charged carriers.[98] Among them, the resistive switching behavior in $HfO_2$ based RRAM is being widely studied considering the localized formation and rupture of CFs within the dielectric film. It is known that under small bias voltage, localized nanosize CFs are formed in oxide film which segregate to produce the stronger and more conductive CFs at higher applied bias voltage. These CFs are mainly comprised of charged oxygen vacancies generating conduction electrons.[98] In this context, Zhang *et al*. investigate that Gd doping in $HfO_2$ lattice enhances RRAM behavior by minimizing the randomized nature of CFs thereby reducing oxygen ion migration barrier.[104] Lee *et al*. demonstrate that while Gd and Dy doped $ZrO_2$ devices exhibit switching behavior due to sufficiently large concentration of dopant induced oxygen vacancies, Ce doped $ZrO_2$ based RRAM shows initial formation of CF which is ascribed to improved crystallization/densification.[193] On the other hand, in $Gd_2O_3$and $HfO_2$based RRAM, a similar role of abundant defects such as oxygen vacancies rendering forming-free switching behavior have been reported.[194, 195] In the present case, in pristine and Sm or Dy doped $HfO_2$ films, the presence of sufficiently high concentration of oxygen vacancies not only shows the monoclinic to cubic phase transformation at RT but also contribute towards resistive switching behavior which is of forming-free nature as reported by others.

A schematic illustration of possible resistive switching mechanism through formation of CFs for $HfO_2$ based RRAMs is depicted in **figure 6.5**. Without bias, the oxygen vacancies present in the film move with random motion. After applying the bias voltage, the current increases considerably indicating partial formation of CFs.

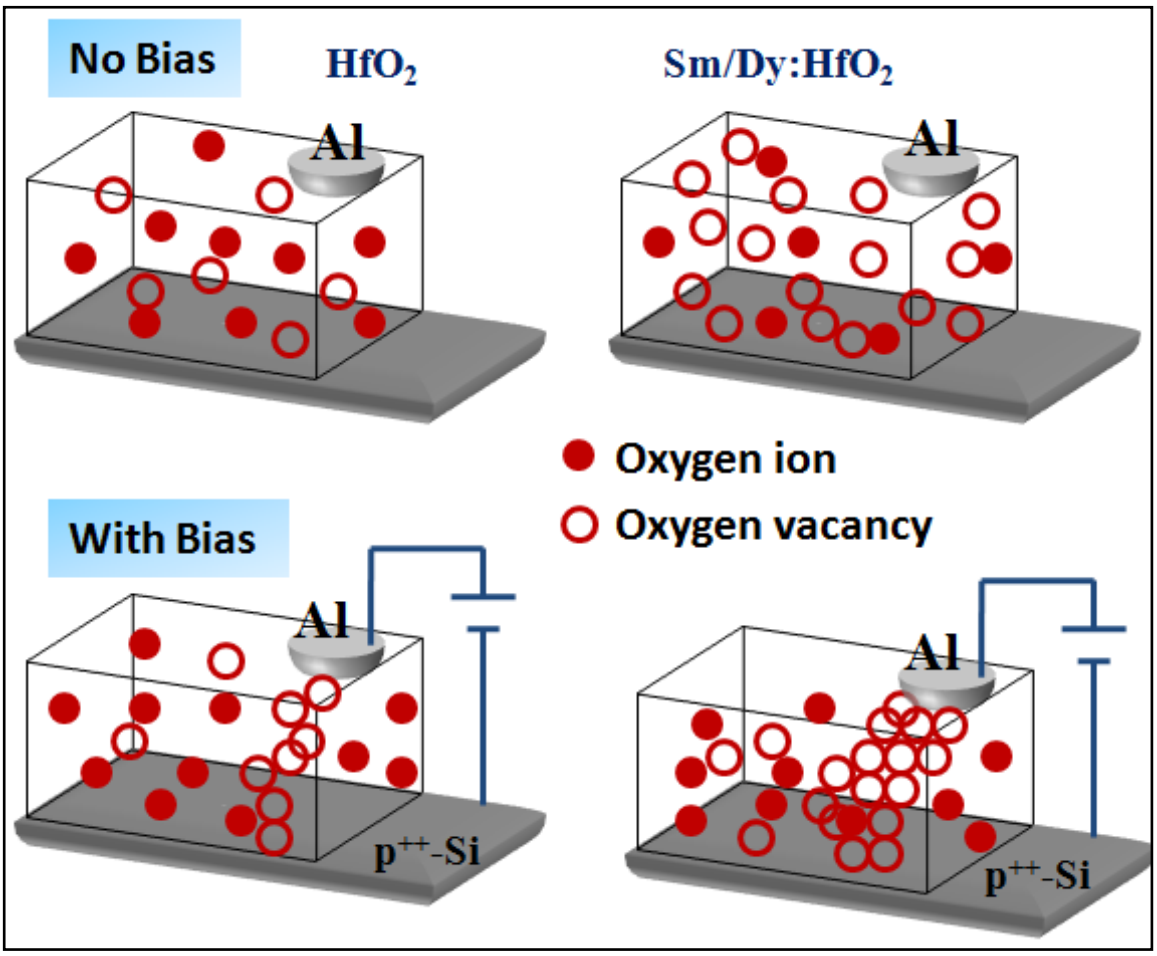


***Figure 6.5*** *The proposed schematic diagram illustrating resistive switching mechanism through CFs formation in pristine and Sm or Dy doped $HfO_2$ RRAM devices.*

At a certain $V_{SET}$ value, all the localized CFs redistribute and combine to form a highly conducting filament containing a more oriented segregation of $V_O$ leading to switching of HRS to LRS state. On the other hand, for negative applied DC voltage, these CFs dissolve and eventually rupture because of the Joule heating effect resulting in LRS to HRS switching at $V_{RESET}$ voltage.[101] In case of Sm or Dy doped $HfO_2$ devices, the concentration of $V_o$ is relatively higher due to substitution of $Dy^{3+}$ or $Sm^{3+}$ ion at$Hf^{4+}$ site generating more number of $V_O$ in the lattice evidenced from XPS analysis. The

incorporation of $Dy^{3+}$ or $Sm^{3+}$ ion in $HfO_2$ reduces the formation energy required to form $V_o$ by creating dipoles between $V_o$ and dopants. As a consequence, $V_o$ tends to reside near dopant site in $HfO_2$ lattice providing improved control of CFs formation.[104] This could allow a well controlled resistive switching from HRS to LRS at a lower $V_{SET}$ value in Sm or Dy doped $HfO_2$ based RRAM devices. These devices would be promising for application in next generation data storage.

## 6.3 Conclusions

To summarize, pristine and Sm, Dy doped $HfO_2$ films were deposited on $p^{++}$-Si (100) substrates having film thickness of ~60 nm with an appropriate film density of ~9.2-8.1 g/cm$^3$. We observed that while pristine film exhibited the monoclinic phase, the high temperature cubic phase was stabilized at RT in Sm or Dy doped $HfO_2$ film after doping at most half concentration of these dopants compared to nanoparticles. The monoclinic to cubic phase transformation was attributed to formation of oxygen vacancies understood from XPS analysis. Due to the presence of oxygen vacancies, we carried out the bipolar resistive switching behavior for RRAM device application. The ON/OFF separation was estimated to approximately three and the resistive switching characteristics was of forming-free nature feasible for RRAM device. After fitting appropriate conduction models, it was confirmed that the Ohmic and P-F emission conduction mechanisms dominated in LRS and HRS states, respectively. The switching behavior was ascribed to the formation and rupture of conducting filaments comprised of oxygen vacancies under positive and negative applied bias, respectively. Therefore, an abundance of oxygen vacancies forming 8-fold oxygen coordination to dopant ion played a crucial role in the stabilization of cubic phase

at RT and also governed the forming-free switching behavior in$HfO_2$ based RRAM devices.

# Chapter 7

This thesis provided a comprehensive investigation on the structure, magnetic, optical and electrical properties of multifunctional nanostructured pure, Dy and/or Sm doped $HfO_2$. The present work dealt with two different forms i.e. nanoparticles and thin films of $HfO_2$. The high temperature tetragonal and cubic phases of $HfO_2$ are promising from industrial point of view due to their appropriate high-*k* value which facilitate the fabrication of CMOS devices with improved performance. In this context, we particularly examined the stabilization of cubic phase at room temperature after incorporating Dy and/or Sm into $HfO_2$ lattice. In addition to intriguing structural transformation, the systematic studies on the effect of Dy and/or Sm dopants in modifying magnetic, optical and electrical properties produced captivating results which could be implemented for practical applications like LFPs imaging for the first time and as non-volatile data storage in RRAM devices. The key findings of the thesis are outlined below.

## 7.1 Stabilization of the High Temperature Cubic Phase at Room Temperature

$HfO_2$ nanoparticles synthesized via a Pechini type sol–gel technique crystallized with monoclinic phase, $P2_1/c$, at room temperature. By incorporating 11 at% of Dy into the $HfO_2$ lattice, the monoclinic phase transformed completely to the cubic phase, $Fm\bar{3}m$, followed by a mixed phase of monoclinic and cubic at intermediate concentrations (5–9 at%) of Dy. In case of Sm doped $HfO_2$, although the monoclinic structure was retained at 1 at% of Sm, the monoclinic to cubic phase transformation at room temperature was achieved by incorporating $Sm^{3+}$ ions upto 12 at% followed by the coexistence of

monoclinic and cubic phase at intermediate Sm concentration (5-11 at%). Selected area electron diffraction patterns established the monoclinic and the cubic phase as observed from XRD patterns. Not only the particle size obtained from TEM matched well with the size calculated from W-H plot, the lattice spacing estimated from high resolution TEM also confirmed the monoclinic phase in $HfO_2$ and cubic phase in $Hf_{0.89}Sm_{0.11}O_2$ and $Hf_{0.88}Sm_{0.12}O_2$ nanoparticles. A mechanism for stabilization of the high temperature cubic phase in Dy or Sm doped $HfO_2$ was analyzed based on the substitution of $Dy^{3+}$ or $Sm^{3+}$ for $Hf^{4+}$ ions and the formation of oxygen vacancies. The significant difference in ionic radii of $Dy^{3+}$, $Sm^{3+}$ and $Hf^{4+}$ ion induced considerably large strain in the lattice examined from W-H analysis. XPS investigation revealed that a lower valency of Dy or Sm accompanied with oxygen vacancies leading to 8-fold coordination with dopant ion and stabilized the high temperature cubic phase at room temperature. Further, we introduced the concept for stabilizing high temperature cubic phase of $HfO_2$ after codoping Dy and Sm. At low Dy and Sm concentration i.e. 0 to 2 at%, while the monoclinic phase was found to be preserved with crystallite size ranging from ~10-25 nm, Le-Bail profile refinement of XRD patterns revealed an exponential increase in lattice volume evidenced due to negative pressure effect. However, after codoping Dy and Sm upto the total concentration of 13 at%, we successfully demonstrated the stabilization of high temperature cubic phase of $HfO_2$ at room temperature. Therefore, the stabilization of cubic phase of $HfO_2$ at room temperature was accomplished with concentration of rare earth dopants attaining ~13 at% irrespective of the nature of dopant.

## 7.2 Room Temperature Ferromagnetism and its Origin

$HfO_2$ nanoparticles exhibited considerable hysteresis loop indicating the ferromagnetic ordering at room temperature. However, RTFM in $HfO_2$ nanoparticles was quenched after incorporating even 1 at% of Dy. Although the maximum magnetization enhanced linearly, the coercivity of ~25±5 Oe remained constant with increasing Dy concentration upto 11 at%. RTFM in $HfO_2$ was attributed to oxygen vacancies mediating long range ferromagnetic ordering via $F^+$ center exchange mechanism. The dramatic suppression of room temperature ferromagnetic ordering in Dy doped $HfO_2$ could be ascribed to the formation of unwanted defect complexes like $Dy^{3+}$–$V_o$–$Dy^{3+}$. Such defect complexes essentially produced $F^{++}$ centers which hindered the long range ferromagnetic ordering in $HfO_2$ lattice. The suppression of ferromagnetic ordering in Dy doped $HfO_2$ discouraged to perform magnetic study in either Sm doped $HfO_2$ or Dy and Sm codoped $HfO_2$ nanoparticles. RTFM observed in diamagnetic $HfO_2$ nanoparticles thus confirmed the crucial role of nanoparticles and optimum concentration of oxygen vacancies. Increasing oxygen vacancies with increasing dopant concentration quenched the ferromagnetic behavior in rare earth doped $HfO_2$ nanoparticles.

## 7.3 Excellent Luminescence Properties

After incorporating 1 at% of Dy, the systematic photoluminescence investigations demonstrated excellent emissions in blue and yellow region producing cool white light under the excitation with UV light of wavelength 352 nm. The intensity of blue and yellow emission peaks reduced with increasing Dy concentration upto 11 at% due to the concentration quenching effect. The characteristic emissions corresponding to $Dy^{3+}$ ion were induced by the non-radiative weak energy transfer occurring between charge transfer

band of the host and distinct energy levels of $Dy^{3+}$ activator ion. We proposed a tentative energy band diagram to show the energetic processes taking place in Dy doped $HfO_2$ nanoparticles. For Sm doped $HfO_2$, the strong emission peaks near green and red regions were revealed in $Hf_{0.99}Sm_{0.01}O_2$ nanoparticles which diminished substantially at higher Sm concentration. The proposed schematic energy band diagram illustrated that the emissions related to $Sm^{3+}$ active ion were partially accompanied by the charge transfer from optically active defect states present in $HfO_2$ to $Sm^{3+}$ energy levels having comparable energy. Further, exciting Dy and Sm codoped $HfO_2$ with 393 nm, the prominent emissions in blue, yellow and near red regions yielded purplish light emerging primarily due to the energy transfer from $Dy^{3+}$ (donor) to $Sm^{3+}$ (acceptor) ions through multipolar interaction suggested by time resolved decay spectra. Combining excitation and emission spectra, we proposed a schematic energy band diagram for rare earth doped and codoped $HfO_2$ nanoparticles.

## 7.4 Latent Fingerprint Imaging for Forensic Science

Considering the rich luminescence behavior, for the first time, Dy and Sm codoped $HfO_2$ nanophosphors were explored for their robustness in the development of LFPs useful for collecting physical evidences in forensic investigations. Herein, these $HfO_2$ based nanophosphors offered a rapid and cost-effective approach for LFPs imaging under irradiation of light having wavelength of 395 nm. Dy and Sm codoped $HfO_2$ could develop LFPs with good selectivity and resolution over multivariate surfaces like float glass, black colored glass, purplish, wine and red colored plastic sheets, stainless steel and aluminum foil etc. Owing to nanosized nature of particles, all the developed LFPs exhibited low background interference facilitating the extraction of crucial third-level details such as enclosure, double bifurcation and termination-bifurcation etc.

## 7.5 Stabilization of Cubic Phase at Room Temperature and RRAM Device Application

We systematically examined the structural evolution and resistive switching behavior of pristine and Sm or Dy doped $HfO_2$ films of ~60 nm deposited on $p^{++}$-Si (100) substrates through electron beam evaporation technique. Although we reported that 12 at% of Sm or 11 at% of Dy doped in $HfO_2$ nanoparticles stabilized the cubic phase at RT, here the stabilization of cubic phase was achieved after doping at most half of these dopant concentration. Further, these films demonstrated the bipolar switching behavior distinctive to RRAM device. The resistive switching characteristics were found to be of forming-free nature. The switching behavior was discussed after employing different conduction models such as the Ohmic and Poole-Frenkel emission. We concluded that the monoclinic to cubic phase transformation and resistive switching phenomenon was governed by the abundant formation of oxygen vacancies producing 8-fold oxygen coordination to $Sm^{3+}$ or $Dy^{3+}$ ion evidenced from XPS spectra. The resistive switching mechanism was illustrated through the formation of conducting filaments pictorially in $HfO_2$ based RRAM which could be further investigated to fabricate data storage devices.

## 7.6 Future Outlook

The thesis discussed the preparation and detailed material characterizations along with appropriate analysis of structure, magnetic, optical and electrical properties of nanostructured pristine, Dy and/or Sm doped $HfO_2$. In view of above findings and potential applications, we suggest a few possible research scopes that can be extended in near future.

- **Local probe analysis:** In the present work, we demonstrated oxygen vacancy induced stabilization of the high temperature cubic phase in Dy and/or Sm doped $HfO_2$ which can be further investigated through sophisticated technique like extended X-ray absorption fine structure (EXAFS) to obtain a more detailed insight.
- **Biological applications:** In addition to LFPs imaging using Dy and Sm codoped $HfO_2$ nanophosphors, one can also develop luminescent $HfO_2$ as efficient probes for potential bio-imaging .
- **Improvement of RRAM device:** Since $HfO_2$ based RRAM is one of the interesting next generation data storage device, we further intend to study thickness and composition dependent resistive switching behavior to fabricate RRAM device with better performance.

# *References*


[1] Chen K, Bell AT, Iglesia E. The relationship between the electronic and redox properties of dispersed metal oxides and their turnover rates in oxidative dehydrogenation reactions. Journal of Catalysis 2002;209:35-42.

[2] Gutowski M, Jaffe JE, Liu C-L, Stoker M, Hegde RI, Rai RS, et al. Thermodynamic stability of high-K dielectric metal oxides $ZrO_2$ and $HfO_2$ in contact with Si and $SiO_2$. Applied Physics Letters 2002;80:1897-9.

[3] Robertson J. High dielectric constant gate oxides for metal oxide Si transistors. Reports on progress in Physics 2005;69:327.

[4] Emeline A, Kataeva G, Panasuk A, Ryabchuk V, Sheremetyeva N, Serpone N. Effect of surface photoreactions on the photocoloration of a wide band gap metal oxide: Probing whether surface reactions are photocatalytic. The Journal of Physical Chemistry B 2005;109:5175-85.

[5] Verma R, Gangwar J, Srivastava AK. Multiphase $TiO_2$ nanostructures: a review of efficient synthesis, growth mechanism, probing capabilities, and applications in bio-safety and health. RSC Advances 2017;7:44199-224.

[6] Park J, An K, Hwang Y, Park J-G, Noh H-J, Kim J-Y, et al. Ultra-large-scale syntheses of monodisperse nanocrystals. Nature materials 2004;3:891.

[7] Kate RS, Khalate SA, Deokate RJ. Overview of nanostructured metal oxides and pure nickel oxide (NiO) electrodes for supercapacitors: a review. Journal of Alloys and Compounds 2018;734:89-111.

[8] Dou S. Review and prospect of layered lithium nickel manganese oxide as cathode materials for Li-ion batteries. Journal of Solid State Electrochemistry 2013;17:911-26.

[9] Özgür Ü, Alivov YI, Liu C, Teke A, Reshchikov M, Doğan S, et al. A comprehensive review of ZnO materials and devices. Journal of applied physics 2005;98:11.

[10] Rajagopal S, Nataraj D, Mangalaraj D, Djaoued Y, Robichaud J, Khyzhun OY. Controlled growth of $WO_3$ nanostructures with three different morphologies and their structural, optical, and photodecomposition studies. Nanoscale research letters 2009;4:1335.

[11] Redel E, Petrov S, Dag Ö, Moir J, Huai C, Mirtchev P, et al. Green nanochemistry: metal oxide nanoparticles and porous thin films from bare metal powders. Small 2012;8:68-72.

[12] Redel E, Huai C, Dag Ö, Petrov S, O'Brien PG, Helander MG, et al. From bare metal powders to colloidally stable TCO dispersions and transparent nanoporous conducting metal oxide thin films. small 2012;8:3806-9.

[13] Kroll E, Winnik FM, Ziolo RF. In situ preparation of nanocrystalline γ-$Fe_2O_3$ in iron (II) cross-linked alginate gels. Chemistry of materials 1996;8:1594-6.

[14] Moreno E, Zayat M, Morales M, Serna C, Roig A, Levy D. Preparation of narrow size distribution superparamagnetic γ-$Fe_2O_3$ nanoparticles in a sol− gel transparent $SiO_2$ matrix. Langmuir 2002;18:4972-8.

[15] Salazar-Alvarez G, Muhammed M, Zagorodni AA. Novel flow injection synthesis of iron oxide nanoparticles with narrow size distribution. Chemical engineering science 2006;61:4625-33.

[16] Devan RS, Patil RA, Lin JH, Ma YR. One-dimensional metal-oxide nanostructures: recent developments in synthesis, characterization, and applications. Advanced Functional Materials 2012;22:3326-70.

[17] Zhang J, Liu X, Neri G, Pinna N. Nanostructured materials for room-temperature gas sensors. Advanced materials 2016;28:795-831.

[18] Kment S, Riboni F, Pausova S, Wang L, Wang L, Han H, et al. Photoanodes based on $TiO_2$ and α-$Fe_2O_3$ for solar water splitting–superior role of 1D nanoarchitectures and of combined heterostructures. Chemical Society Reviews 2017;46:3716-69.

[19] Li F-t, Ran J, Jaroniec M, Qiao SZ. Solution combustion synthesis of metal oxide nanomaterials for energy storage and conversion. Nanoscale 2015;7:17590-610.

[20] Zheng JY, Haider Z, Van TK, Pawar AU, Kang MJ, Kim CW, et al. Tuning of the crystal engineering and photoelectrochemical properties of crystalline tungsten oxide for optoelectronic device applications. CrystEngComm 2015;17:6070-93.

[21] Gnanasekaran L, Hemamalini R, Saravanan R, Ravichandran K, Gracia F, Agarwal S, et al. Synthesis and characterization of metal oxides ($CeO_2$, CuO, NiO, $Mn_3O_4$, $SnO_2$ and ZnO) nanoparticles as photo catalysts for degradation of textile dyes. Journal of Photochemistry and Photobiology B: Biology 2017;173:43-9.

[22] Choi SJ, Kim SJ, Cho HJ, Jang JS, Lin YM, Tuller HL, et al. $WO_3$ Nanofiber-Based Biomarker Detectors Enabled by Protein-Encapsulated Catalyst Self-Assembled on Polystyrene Colloid Templates. Small 2016;12:911-20.

[23] Gao P, Liu R, Huang H, Jia X, Pan H. MOF-templated controllable synthesis of α-$Fe_2O_3$ porous nanorods and their gas sensing properties. Rsc Advances 2016;6:94699-705.

[24] Rathnasamy R, Thangasamy P, Thangamuthu R, Sampath S, Alagan V. Green synthesis of ZnO nanoparticles using Carica papaya leaf extracts for photocatalytic and

photovoltaic applications. Journal of Materials Science: Materials in Electronics 2017;28:10374-81.

[25] Edison TNJI, Atchudan R, Lee YR. Binder-free electro-synthesis of highly ordered nickel oxide nanoparticles and its electrochemical performance. Electrochimica Acta 2018;283:1609-17.

[26] Scarano D, Cesano F, Bertarione S, Zecchina A. Zinc Oxide Nanostructures: From Chestnut Husk-Like Structures to Hollow Nanocages, Synthesis and Structure. Crystals 2018;8:153.

[27] Banfield J. Thermodynamic analysis of phase stability of nanocrystalline titania. Journal of Materials Chemistry 1998;8:2073-6.

[28] Zhang Z, Zhong X, Liu S, Li D, Han M. Aminolysis route to monodisperse titania nanorods with tunable aspect ratio. Angewandte Chemie International Edition 2005;44:3466-70.

[29] Zhu K-R, Zhang M-S, Hong J-M, Yin Z. Size effect on phase transition sequence of $TiO_2$ nanocrystal. Materials Science and Engineering: A 2005;403:87-93.

[30] Malekshahi Byranvand M, Nemati Kharat A, Fatholahi L, Malekshahi Beiranvand Z. A review on synthesis of nano-$TiO_2$ via different methods. Journal of nanostructures 2013;3:1-9.

[31] Schulz M. The end of the road for silicon? Nature 1999;399:729.

[32] Bohr MT, Chau RS, Ghani T, Mistry K. The high-*k* solution. IEEE spectrum 2007;44:29-35.

[33] Wilk GD, Wallace RM, Anthony J. High-κ gate dielectrics: Current status and materials properties considerations. Journal of applied physics 2001;89:5243-75.

[34] Lee BH, Kang L, Qi W-J, Nieh R, Jeon Y, Onishi K, et al. Ultrathin hafnium oxide with low leakage and excellent reliability for alternative gate dielectric application. International Electron Devices Meeting 1999 Technical Digest (Cat No 99CH36318): IEEE; 1999. p. 133-6.

[35] Venkateshan A, Singh R, Poole K, Harriss J, Senter H, Teague R, et al. High-κ gate dielectrics with ultra-low leakage current for sub-45 nm CMOS. Electronics Letters 2007;43:1130-2.

[36] Khoshman J, Khan A, Kordesch M. Amorphous hafnium oxide thin films for antireflection optical coatings. Surface and Coatings Technology 2008;202:2500-2.

[37] Zhao J, Zhang Y, Gong H, Zhang Y, Wang X, Guo X, et al. Fabrication of high-performance $Y_2O_3$ stabilized hafnium dioxide refractories. Ceramics International 2015;41:5232-8.

[38] Vargas M, Murphy N, Ramana C. Tailoring the index of refraction of nanocrystalline hafnium oxide thin films. Applied Physics Letters 2014;104:101907.

[39] Hadacek N, Nosov A, Ranno L, Strobel P, Galéra R-M. Magnetic properties of $HfO_2$ thin films. Journal of Physics: Condensed Matter 2007;19:486206.

[40] Lee HY, Chen PS, Wu TY, Chen YS, Wang CC, Tzeng PJ, et al. Low power and high speed bipolar switching with a thin reactive Ti buffer layer in robust $HfO_2$ based RRAM. 2008 IEEE International Electron Devices Meeting2008. p. 1-4.

[41] Park MH, Lee YH, Kim HJ, Kim YJ, Moon T, Kim KD, et al. Ferroelectricity and Antiferroelectricity of Doped Thin $HfO_2$-Based Films. Advanced Materials 2015;27:1811-31.

[42] Wang C, Zinkevich M, Aldinger F. The Zirconia–Hafnia System: DTA Measurements and Thermodynamic Calculations. Journal of the American Ceramic Society 2006;89:3751-8.

[43] RUH R, PATEL VA. Proposed Phase Relations in the $HfO_2$-Rich Portion of the System Hf-HfO2. Journal of the American Ceramic Society 1973;56:606-7.

[44] El-Shanshoury I, Rudenko V, Ibrahim I. Polymorphic behavior of thin evaporated films of zirconium and hafnium oxides. Journal of the American Ceramic Society 1970;53:264-8.

[45] Kisi EH, Howard C. Crystal structures of zirconia phases and their inter-relation. Key Engineering Materials: Trans Tech Publ; 1998. p. 1-36.

[46] Ohtaka O, Fukui H, Kunisada T, Fujisawa T, Funakoshi K, Utsumi W, et al. Phase relations and volume changes of hafnia under high pressure and high temperature. Journal of the American Ceramic Society 2001;84:1369-73.

[47] Ohtaka O, Yamanaka T, Kume S, Hara N, Asano H, Izumi F. Structural analysis of orthorhombic hafnia by neutron powder diffraction. Journal of the American Ceramic Society 1995;78:233-7.

[48] Liu L-G. New high pressure phases of $ZrO_2$ and $HfO_2$. Journal of Physics and Chemistry of Solids 1980;41:331-4.

[49] Fischer D, Kersch A. Stabilization of the high-k tetragonal phase in $HfO_2$: The influence of dopants and temperature from ab initio simulations. Journal of Applied Physics 2008;104:084104.

[50] Sharath S, Kurian J, Komissinskiy P, Hildebrandt E, Bertaud T, Walczyk C, et al. Thickness independent reduced forming voltage in oxygen engineered $HfO_2$ based resistive switching memories. Applied Physics Letters 2014;105:073505.

[51] Rauwel E, Galeckas A, Rauwel P. Photoluminescent cubic and monoclinic $HfO_2$ nanoparticles: effects of temperature and ambient. Materials Research Express 2014;1:015035.

[52] Foster AS, Gejo FL, Shluger A, Nieminen RM. Vacancy and interstitial defects in hafnia. Physical Review B 2002;65:174117.

[53] Lee C-K, Cho E, Lee H-S, Hwang CS, Han S. First-principles study on doping and phase stability of $HfO_2$. Physical Review B 2008;78:012102.

[54] Lauria A, Villa I, Fasoli M, Niederberger M, Vedda A. Multifunctional role of rare earth doping in optical materials: Nonaqueous sol–gel synthesis of stabilized cubic $HfO_2$ luminescent nanoparticles. Acs Nano 2013;7:7041-52.

[55] Gálvez-Barboza S, González L, Puente-Urbina B, Saucedo-Salazar E, García-Cerda L. Preparation and characterization of Ce-doped $HfO_2$ nanoparticles. Journal of Alloys and Compounds 2015;643:S62-S6.

[56] Böscke T, Müller J, Bräuhaus D, Schröder U, Böttger U. Ferroelectricity in hafnium oxide thin films. Applied Physics Letters 2011;99:102903.

[57] Kisi EH. Influence of Hydrostatic Pressure on the t→ o Transformation in Mg-PSZ Studied by In Situ Neutron Diffraction. Journal of the American Ceramic Society 1998;81:741-5.

[58] Starschich S, Boettger U. An extensive study of the influence of dopants on the ferroelectric properties of $HfO_2$. Journal of Materials Chemistry C 2017;5:333-8.

[59] Materlik R, Künneth C, Kersch A. The origin of ferroelectricity in $Hf_{1-x}Zr_xO_2$: A computational investigation and a surface energy model. Journal of Applied Physics 2015;117:134109.

[60] Venkatesan M, Fitzgerald C, Coey J. Thin films: unexpected magnetism in a dielectric oxide. Nature 2004;430:630.

[61] Sharma P, Gupta A, Rao K, Owens FJ, Sharma R, Ahuja R, et al. Ferromagnetism above room temperature in bulk and transparent thin films of Mn-doped ZnO. Nature materials 2003;2:673.

[62] Bi H, Li S, Zhang Y, Du Y. Ferromagnetic-like behavior of ultrafine NiO nanocrystallites. Journal of magnetism and magnetic materials 2004;277:363-7.

[63] Rumaiz AK, Ali B, Ceylan A, Boggs M, Beebe T, Shah SI. Experimental studies on vacancy induced ferromagnetism in undoped $TiO_2$. Solid State Communications 2007;144:334-8.

[64] Coey J, Douvalis A, Fitzgerald C, Venkatesan M. Ferromagnetism in Fe-doped $SnO_2$ thin films. Applied Physics Letters 2004;84:1332-4.

[65] Ning S, Zhan P, Xie Q, Li Z, Zhang Z. Room-temperature ferromagnetism in un-doped ZrO2 thin films. Journal of Physics D: Applied Physics 2013;46:445004.

[66] Dohčević-Mitrović Z, Paunović N, Matović B, Osiceanu P, Scurtu R, Aškrabić S, et al. Structural dependent room-temperature ferromagnetism in yttrium doped $HfO_2$ nanoparticles. Ceramics International 2015;41:6970-7.

[67] Liu X, Chen Y, Wang L, Peng D-L. Transition from paramagnetism to ferromagnetism in $HfO_2$ nanorods. AIP; 2013.

[68] Zheng J, Ceder G, Maxisch T, Chim W, Choi W. First-principles study of native point defects in hafnia and zirconia. Physical Review B 2007;75:104112.

[69] Broqvist P, Pasquarello A. Oxygen vacancy in monoclinic $HfO_2$: A consistent interpretation of trap assisted conduction, direct electron injection, and optical absorption experiments. Applied physics letters 2006;89:262904.

[70] Conesa J. Computer modeling of surfaces and defects on cerium dioxide. Surface Science 1995;339:337-52.

[71] Ramo DM, Gavartin J, Shluger A, Bersuker G. Spectroscopic properties of oxygen vacancies in monoclinic $HfO_2$ calculated with periodic and embedded cluster density functional theory. Physical Review B 2007;75:205336.

[72] Coey J, Venkatesan M, Fitzgerald C. Donor impurity band exchange in dilute ferromagnetic oxides. Nature materials 2005;4:173.

[73] Shah LR, Ali B, Zhu H, Wang W, Song Y, Zhang H, et al. Detailed study on the role of oxygen vacancies in structural, magnetic and transport behavior of magnetic insulator: Co–$CeO_2$. Journal of Physics: Condensed Matter 2009;21:486004.

[74] Pemmaraju CD, Sanvito S. Ferromagnetism driven by intrinsic point defects in $HfO_2$. Physical review letters 2005;94:217205.

[75] Lin K-Q, Wang L-S, Wang Z-W, Wen R-T, Chen Y, Peng D-L. Gas-phase synthesis and magnetism of $HfO_2$ nanoclusters. The European Physical Journal D 2013;67:42.

[76] Abraham DW, Frank MM, Guha S. Absence of magnetism in hafnium oxide films. Applied Physics Letters 2005;87:252502.

[77] Coey J. d0 ferromagnetism. Solid State Sciences 2005;7:660-7.

[78] Kumar Sharma M, Kumar Mishra D, Ghosh S, Kanjilal D, Srivastava P, Chatterjee R. Oxygen vacancy mediated large magnetization in chemically synthesized Ni-doped $HfO_2$ nanoparticle powder samples. Journal of Applied Physics 2011;110:063902.

[79] Chang Y, Soo Y, Lee W, Huang M, Lee Y, Weng S, et al. Observation of room temperature ferromagnetic behavior in cluster-free, Co doped $HfO_2$ films. Applied Physics Letters 2007;91:082504.

[80] Hong NH, Poirot N, Sakai J. Evidence for magnetism due to oxygen vacancies in Fe-doped $HfO_2$ thin films. Applied physics letters 2006;89:042503.

[81] Wang W, Hong Y, Yu M, Rout B, Glass GA, Tang J. Structure and magnetic properties of pure and Gd-doped $HfO_2$ thin films. Journal of applied physics 2006;99:08M117.

[82] Lozanov VV, Baklanova NI, Shayapov VR, Berezin AS. Crystal growth and photoluminescence properties of reactive CVD-derived monoclinic hafnium dioxide. Crystal Growth & Design 2016;16:5283-93.

[83] Villa I, Vedda A, Fasoli M, Lorenzi R , Kränzlin N , Rechberger F, et al. Size-dependent luminescence in $HfO_2$ nanocrystals: Toward white emission from intrinsic surface defects. Chemistry of Materials 2016;28:3245-53.

[84] Carvalho JM, Rodrigues LC, Felinto MC, Nunes LA, Hölsä J, Brito HF. Structure–property relationship of luminescent zirconia nanomaterials obtained by sol–gel method. Journal of materials science 2015;50:873-81.

[85] Fiaczyk K, Wojtowicz AJ, Zych E. Photoluminescent Properties of Monoclinic $HfO_2$: Ti Sintered Ceramics in 16–300 K. The Journal of Physical Chemistry C 2015;119:5026-32.

[86] Rauwel P, Rauwel E, Persson C, Sunding M, Galeckas A. One step synthesis of pure cubic and monoclinic $HfO_2$ nanoparticles: Correlating the structure to the electronic properties of the two polymorphs. Journal of Applied Physics 2012;112:104107.

[87] Jestin Y, Armellini C, Chiappini A, Chiasera A, Ferrari M, Goyes C, et al. Erbium activated $HfO_2$ based glass–ceramics waveguides for photonics. Journal of Non-Crystalline Solids 2007;353:494-7.

[88] LeLuyer C, Villanueva-Ibañez M, Pillonnet A, Dujardin C. $HfO_2$:X (X = $Eu^{3+}$, $Ce^{3+}$, $Y^{3+}$) Sol Gel Powders for Ultradense Scintillating Materials. The Journal of Physical Chemistry A 2008;112:10152-5.

[89] Chen S, Liu Z, Feng L, Zhao X. Photoluminescent properties of undoped and Ce-doped $HfO_2$ thin films prepared by magnetron sputtering. Journal of Luminescence 2014;153:148-51.

[90] Eyring L, Gschneidner KA, Lander GH. Handbook on the physics and chemistry of rare earths: Elsevier; 2002.

[91] Wiatrowska A, Zych E. Modeling Luminescent Properties of $HfO_2$:Eu Powders with Li, Ta, Nb, and V Codopants. The Journal of Physical Chemistry C 2012;116:6409-19.

[92] Aguilar-Castillo A, Aguilar-Hernández JR, García-Hipólito M, López-Romero S, Swarnkar RK, Báez-Rodríguez A, et al. White light generation from $HfO_2$ films co-doped with $Eu^{3+}$ and $Tb3^{3+}$ ions synthesized by pulsed laser ablation technique. Ceramics International 2017;43:355-62.

[93] Murphy CB, Zhang Y, Troxler T, Ferry V, Martin JJ, Jones WE. Probing Förster and Dexter Energy-Transfer Mechanisms in Fluorescent Conjugated Polymer Chemosensors. The Journal of Physical Chemistry B 2004;108:1537-43.

[94] Malta OL. Mechanisms of non-radiative energy transfer involving lanthanide ions revisited. Journal of Non-Crystalline Solids 2008;354:4770-6.

[95] Villa I, Villa C, Monguzzi A, Babin V, Tervoort E, Nikl M, et al. Demonstration of cellular imaging by using luminescent and anti-cytotoxic europium-doped hafnia nanocrystals. Nanoscale 2018;10:7933-40.

[96] Furasova AD, Fakhardo AF, Milichko VA, Tervoort E, Niederberger M, Vinogradov VV. Synthesis of a rare-earth doped hafnia hydrosol: Towards injectable luminescent nanocolloids. Colloids and Surfaces B: Biointerfaces 2017;154:21-6.

[97] Pan F, Gao S, Chen C, Song C, Zeng F. Recent progress in resistive random access memories: materials, switching mechanisms, and performance. Materials Science and Engineering: R: Reports 2014;83:1-59.

[98] Wong H-SP, Lee H-Y, Yu S, Chen Y-S, Wu Y, Chen P-S, et al. Metal–oxide RRAM. Proceedings of the IEEE 2012;100:1951-70.

[99] Akinaga H, Shima H. Resistive random access memory (ReRAM) based on metal oxides. Proceedings of the IEEE 2010;98:2237-51.

[100] Ye C, Wu J, He G, Zhang J, Deng T, He P, et al. Physical mechanism and performance factors of metal oxide based resistive switching memory: a review. Journal of Materials Science & Technology 2016;32:1-11.

[101] Lin K-L, Hou T-H, Shieh J, Lin J-H, Chou C-T, Lee Y-J. Electrode dependence of filament formation in $HfO_2$ resistive-switching memory. Journal of Applied Physics 2011;109:084104.

[102] Chen Y, Chen B, Gao B, Liu L, Liu X, Kang J. Well controlled multiple resistive switching states in the Al local doped $HfO_2$ resistive random access memory device. Journal of Applied Physics 2013;113:164507.

[103] Akbari M, Lee J-S. Control of resistive switching behaviors of solution-processed $HfO_x$-based resistive switching memory devices by n-type doping. RSC Advances 2016;6:21917-21.

[104] Zhang H, Liu L, Gao B, Qiu Y, Liu X, Lu J, et al. Gd-doping effect on performance of $HfO_2$ based resistive switching memory devices using implantation approach. Applied Physics Letters 2011;98:042105.

[105] Xiong Y, Tu H, Du J, Zhang X, Chen D, Wang W. Effects of rapid thermal annealing on structure and electrical properties of Gd-doped $HfO_2$ high k film. Applied Physics Letters 2011;98:082906.

[106] Laigo J, Christien F, Le Gall R, Tancret F, Furtado J. SEM, EDS, EPMA-WDS and EBSD characterization of carbides in HP type heat resistant alloys. Materials characterization 2008;59:1580-6.

[107] Lloyd GE. Atomic number and crystallographic contrast images with the SEM: a review of backscattered electron techniques. Mineralogical Magazine 1987;51:3-19.

[108] Williamson G, Hall W. X-ray line broadening from filed aluminium and wolfram. Acta metallurgica 1953;1:22-31.

[109] Gao L, Zhou L, Feng J, Bai L, Li C, Liu Z, et al. Stabilization of cubic structure in Mn-doped hafnia. Ceramics International 2012;38:2305-11.

[110] Mendoza-Mendoza E, Quintero-García J, Puente-Urbina B, Rodríguez-Fernández O, García-Cerda L. Synthesis and characterization of Ce-doped $HfO_2$ nanoparticles in molten chlorides. Journal of Alloys and Compounds 2017;692:448-53.

[111] Matović B, Bučevac D, Prekajski M, Maksimović V, Gautam D, Yoshida K, et al. Synthesis and characterization of nanometric yttrium-doped hafnia solid solutions. Journal of the European Ceramic Society 2012;32:1971-6.

[112] Li P, Chen IW, Penner-Hahn JE. Effect of dopants on zirconia stabilization—an X-ray absorption study: I, trivalent dopants. Journal of the American Ceramic Society 1994;77:118-28.

[113] Osorio-Guillén J, Lany S, Barabash SV, Zunger A. Nonstoichiometry as a source of magnetism in otherwise nonmagnetic oxides: Magnetically interacting cation vacancies and their percolation. Physical Review B 2007;75:184421.

[114] Baik HS, Kim M, Park G-S, Song SA, Varela M, Franceschetti A, et al. Interface structure and non-stoichiometry in $HfO_2$ dielectrics. Applied physics letters 2004;85:672-4.

[115] Zhang H, Gao B, Yu S, Lai L, Zeng L, Sun B, et al. Effects of ionic doping on the behaviors of oxygen vacancies in $HfO_2$ and $ZrO_2$: A first principles study. 2009 International Conference on Simulation of Semiconductor Processes and Devices: IEEE; 2009. p. 1-4.

[116] Singh V, Rai S, Mishra H, Rath C. Stabilization of high temperature hexagonal phase of $SrAl_2O_4$ at room temperature: role of ZnO. Dalton Transactions 2014;43:5309-16.

[117] Coey JMD, Venkatesan M, Stamenov P, Fitzgerald C, Dorneles L. Magnetism in hafnium dioxide. Physical Review B 2005;72:024450.

[118] Tirosh E, Markovich G. Control of defects and magnetic properties in colloidal $HfO_2$ nanorods. Advanced Materials 2007;19:2608-12.

[119] Liu Y, Lockman Z, Aziz A, MacManus-Driscoll J. Size dependent ferromagnetism in cerium oxide (CeO2) nanostructures independent of oxygen vacancies. Journal of Physics: Condensed Matter 2008;20:165201.

[120] Gao D, Li J, Li Z, Zhang Z, Zhang J, Shi H, et al. Defect-mediated magnetism in pure CaO nanopowders. The Journal of Physical Chemistry C 2010;114:11703-7.

[121] Mohanty P, Kabiraj D, Mandal R, Kulriya P, Sinha A, Rath C. Evidence of room temperature ferromagnetism in argon/oxygen annealed $TiO_2$ thin films deposited by electron beam evaporation technique. Journal of Magnetism and Magnetic Materials 2014;355:240-5.

[122] Glinchuk MD, Eliseev EA, Khist VV, Morozovska AN. Ferromagnetism induced by magnetic vacancies as a size effect in thin films of nonmagnetic oxides. Thin Solid Films 2013;534:685-92.

[123] Hong NH, Sakai J, Poirot N, Brizé V. Room-temperature ferromagnetism observed in undoped semiconducting and insulating oxide thin films. Physical Review B 2006;73:132404.

[124] Singh R. Unexpected magnetism in nanomaterials. Journal of Magnetism and Magnetic Materials 2013;346:58-73.

[125] Ran J, Yan Z. Observation of ferromagnetism in highly oxygen-deficient $HfO_2$ films. Journal of Semiconductors 2009;30:102002.

[126] Zhang Q, Chen G, Yunoki S. Surface ferromagnetism in $HfO_2$ induced by excess oxygen. Solid State Communications 2017;252:33-9.

[127] Sundaresan A, Bhargavi R, Rangarajan N, Siddesh U, Rao C. Ferromagnetism as a universal feature of nanoparticles of the otherwise nonmagnetic oxides. Physical Review B 2006;74:161306.

[128] Mishra D, Mandal BP, Mukherjee R, Naik R, Lawes G, Nadgorny B. Oxygen vacancy enhanced room temperature magnetism in Al-doped MgO nanoparticles. Applied Physics Letters 2013;102:182404.

[129] Wang X, Dai Z, Zeng Z. Search for ferromagnetism in $SnO_2$ doped with transition metals (V, Mn, Fe, and Co). Journal of Physics: Condensed Matter 2008;20:045214.

[130] Yang G, Gao D, Zhang J, Zhang J, Shi Z, Xue D. Evidence of vacancy-induced room temperature ferromagnetism in amorphous and crystalline $Al_2O_3$ nanoparticles. The Journal of Physical Chemistry C 2011;115:16814-8.

[131] Ge M, Wang H, Liu E, Liu J, Jiang J, Li Y, et al. On the origin of ferromagnetism in $CeO_2$ nanocubes. Applied Physics Letters 2008;93:062505.

[132] Paunović N, Dohčević-Mitrović Z, Scurtu R, Aškrabić S, Prekajski M, Matović B, et al. Suppression of inherent ferromagnetism in Pr-doped $CeO_2$ nanocrystals. Nanoscale 2012;4:5469-76.

[133] Chen G, Hou Z, Gong X, Li Q. Effects of Y doping on the structural stability and defect properties of cubic $HfO_2$. Journal of Applied Physics 2008;104:074101.

[134] Dominiak-Dzik G, Ryba-Romanowski W, Palatnikov M, Sidorov N, Kalinnikov V. Dysprosium-doped $LiNbO_3$ crystal. Optical properties and effect of temperature on fluorescence dynamics. Journal of molecular structure 2004;704:139-44.

[135] Liu X, Xiang W, Chen F, Hu Z, Zhang W. Synthesis and photoluminescence characteristics of $Dy^{3+}$ doped $NaY(WO_4)_2$ phosphors. Materials Research Bulletin 2013;48:281-5.

[136] Diaz-Torres L, De la Rosa E, Salas P, Romero V, Angeles-Chavez C. Efficient photoluminescence of $Dy^{3+}$ at low concentrations in nanocrystalline $ZrO_2$. Journal of Solid State Chemistry 2008;181:75-80.

[137] Gu F, Wang SF, Lü MK, Zhou GJ, Liu SW, Xu D, et al. Effect of $Dy^{3+}$ doping and calcination on the luminescence of $ZrO_2$ nanoparticles. Chemical physics letters 2003;380:185-9.

[138] Shang M, Geng D, Kang X, Yang D, Zhang Y, Lin J. Hydrothermal derived LaOF: $Ln^{3+}$ (Ln= Eu, Tb, Sm, Dy, Tm, and/or Ho) nanocrystals with multicolor-tunable emission properties. Inorganic chemistry 2012;51:11106-16.

[139] De la Rosa-Cruz E, Diaz-Torres L, Salas P, Castano V, Hernandez J. Evidence of non-radiative energy transfer from the host to the active ions in monoclinic $ZrO_2$: $Sm^{3+}$. Journal of Physics D: Applied Physics 2001;34:L83.

[140] De la Rosa-Cruz E, Diaz-Torres L, Salas P, Rodrıguez R, Kumar G, Meneses M, et al. Luminescent properties and energy transfer in $ZrO_2$:$Sm^{3+}$ nanocrystals. Journal of applied physics 2003;94:3509-15.

[141] Williamson GK, Hall WH. X-ray line broadening from filed aluminium and wolfram. Acta Metallurgica 1953;1:22-31.

[142] Chandana R, Mallick P, Dhananjai P, Sa D, Banerjee A, Mishra NC. Anomalous x-ray diffraction peak broadening and lattice strains in $Zn_{1-x}Co_xO$ dilute magnetic semiconductors. Journal of Physics: Condensed Matter 2009;21:075801.

[143] Gálvez-Barboza S, González LA, Puente-Urbina BA, Saucedo-Salazar EM, García-Cerda LA. Preparation and characterization of Ce-doped $HfO_2$ nanoparticles. Journal of Alloys and Compounds 2015;643:S62-S6.

[144] Kumar S, Rai SB, Rath C. Multifunctional role of dysprosium in $HfO_2$: stabilization of the high temperature cubic phase, and magnetic and photoluminescence properties. Physical Chemistry Chemical Physics 2017;19:18957-67.

[145] Mendoza-Mendoza E, Quintero-García JS, Puente-Urbina BA, Rodríguez-Fernández OS, García-Cerda LA. Synthesis and characterization of Ce-doped $HfO_2$ nanoparticles in molten chlorides. Journal of Alloys and Compounds 2017;692:448-53.

[146] Lee C-K, Cho E, Lee H-S, Hwang CS, Han S. First-principles study on doping and phase stability of $HfO_2$. Physical Review B 2008;78:012102.

[147] Foster AS, Lopez Gejo F, Shluger AL, Nieminen RM. Vacancy and interstitial defects in hafnia. Physical Review B 2002;65:174117.

[148] Sergienko T, Gustavsson B, Brändström U, Axelsson K. Modelling of optical emissions enhanced by the HF pumping of the ionospheric F-region. Ann Geophys 2012;30:885-95.

[149] Ni J, Zhou Q, Li Z, Zhang Z. Oxygen defect induced photoluminescence of $HfO_2$ thin films. Applied Physics Letters 2008;93:011905.

[150] Gritsenko VA, Islamov DR, Perevalov TV, Aliev VS, Yelisseyev AP, Lomonova EE, et al. Oxygen Vacancy in Hafnia as a Blue Luminescence Center and a Trap of Charge Carriers. The Journal of Physical Chemistry C 2016;120:19980-6.

[151] Ito T, Maeda M, Nakamura K, Kato H, Ohki Y. Similarities in photoluminescence in hafnia and zirconia induced by ultraviolet photons. Journal of Applied Physics 2005;97:054104.

[152] Annapurna K, Dwivedi RN, Kundu P, Buddhudu S. Fluorescence properties of $Sm^{3+}$: $ZnCl_2$:$BaCl_2$:LiCl glass. Materials Research Bulletin 2003;38:429-36.

[153] Rosa-Cruz EDl, Diaz-Torres LA, Salas P, Rodríguez RA, Kumar GA, Meneses MA, et al. Luminescent properties and energy transfer in $ZrO_2$:$Sm^{3+}$ nanocrystals. Journal of Applied Physics 2003;94:3509-15.

[154] May PS, Metcalf DH, Richardson FS, Carter RC, Miller CE, Palmer RA. Measurement and analysis of excited-state decay kinetics and chiroptical activity in the $^6H_J \leftarrow {}^4G_{5/2}$ transitions of $Sm^{3+}$ in trigonal $Na_3[Sm(C_4H_4O_5)_3].2NaClO_4.6H_2O$. Journal of Luminescence 1992;51:249-68.

[155] Devlin K, o'Kelly B, Tang ZR, McDonagh C, McGilp JF. A structural study of the sol-gel process by optical fluorescence and decay time spectroscopy. Journal of non-crystalline solids 1991;135:8-14.

[156] Zych E, Wójtowicz M, Dobrowolska A, Kępiński L. Radioluminescence and photoluminescence of hafnia-based Eu-doped phosphors. Optical Materials 2009;31:1764-7.

[157] Assefa Z, Haire RG, Raison PE. Photoluminescence and Raman studies of $Sm^{3+}$ and $Nd^{3+}$ ions in zirconia matrices: example of energy transfer and host–guest interactions. Spectrochimica Acta Part A: Molecular and Biomolecular Spectroscopy 2004;60:89-95.

[158] Jamalaiah BC, Suresh Kumar J, Mohan Babu A, Suhasini T, Rama Moorthy L. Photoluminescence properties of $Sm^{3+}$ in LBTAF glasses. Journal of Luminescence 2009;129:363-9.

[159] Nayab Rasool S, Rama Moorthy L, Jayasankar CK. Spectroscopic Investigation of $Sm^{3+}$ doped phosphate based glasses for reddish-orange emission. Optics Communications 2013;311:156-62.

[160] Wang SF, Gu F, Lü MK, Yang ZS, Zhou GJ, Zhang HP, et al. Structure evolution and photoluminescence properties of $ZrO_2$:$Eu^{3+}$ nanocrystals. Optical Materials 2006;28:1222-6.

[161] Rosa-Cruz EDl, Díaz-Torres LA, Salas P, Castaño VM, Hernández JM. Evidence of non-radiative energy transfer from the host to the active ions in monoclinic $ZrO_2$:$Sm^{3+}$. Journal of Physics D: Applied Physics 2001;34:L83.

[162] Cullity BD. Elements of x-ray diffraction. Reading, MA: Addison-Wesley Publishing Company, Inc.; 1978.

[163] Yang L, Li L, Zhao M, Li G. Size-induced variations in bulk/surface structures and their impact on photoluminescence properties of $GdVO_4$:$Eu^{3+}$ nanoparticles. Physical Chemistry Chemical Physics 2012;14:9956-65.

[164] Perebeinos V, Chan S-W, Zhang F. 'Madelung model'prediction for dependence of lattice parameter on nanocrystal size. Solid state communications 2002;123:295-7.

[165] Diehm PM, Ágoston P, Albe K. Size-Dependent Lattice Expansion in Nanoparticles: Reality or Anomaly? ChemPhysChem 2012;13:2443-54.

[166] Dominiak-Dzik G, Ryba-Romanowski W, Palatnikov MN, Sidorov NV, Kalinnikov VT. Dysprosium-doped $LiNbO_3$ crystal. Optical properties and effect of temperature on fluorescence dynamics. Journal of molecular structure 2004;704:139-44.

[167] Kumar S, Rai SB, Rath C. Multifunctional role of dysprosium in $HfO_2$: stabilization of the high temperature cubic phase, and magnetic and photoluminescence properties. Physical Chemistry Chemical Physics 2017;19:18957-67.

[168] Diaz-Torres LA, De la Rosa E, Salas P, Romero VH, Angeles-Chavez C. Efficient photoluminescence of $Dy^{3+}$ at low concentrations in nanocrystalline $ZrO_2$. Journal of Solid State Chemistry 2008;181:75-80.

[169] Kumar S, Rai SB, Rath C. Monoclinic to cubic phase transformation and photoluminescence properties in $Hf_{1-x}Sm_xO_2$ (x= 0–0.12) nanoparticles. Journal of Applied Physics 2018;123:055108.

[170] Annapurna K, Dwivedi RN, Kundu P, Buddhudu S. Fluorescence properties of $Sm^{3+}$: $ZnCl_2$: $BaCl_2$: LiCl glass. Materials research bulletin 2003;38:429-36.

[171] Foster AS, Gejo FL, Shluger AL, Nieminen RM. Vacancy and interstitial defects in hafnia. Physical Review B 2002;65:174117.

[172] Villabona-Leal EG, Diaz-Torres LA, Desirena H, Rodríguez-López JL, Pérez E, Meza O. Luminescence and energy transfer properties of $Eu^{3+}$ and $Gd^{3+}$ in $ZrO_2$. Journal of Luminescence 2014;146:398-403.

[173] May PS, Metcalf DH, Richardson FS, Carter RC, Miller CE, Palmer RA. Measurement and analysis of excited-state decay kinetics and chiroptical activity in the $^6H_J \leftarrow {}^4G_{5/2}$ transitions of $Sm^{3+}$ in trigonal $Na_3[Sm(C_4H_4O_5)_3].2NaClO_4.6H_2O$. Journal of luminescence 1992;51:249-68.

[174] De la Rosa-Cruz E, Diaz-Torres LA, Salas P, Rodrıguez RA, Kumar GA, Meneses MA, et al. Luminescent properties and energy transfer in $ZrO_2$:$Sm_{3+}$ nanocrystals. Journal of applied physics 2003;94:3509-15.

[175] Jia G, Song Y, Yang M, Huang Y, Zhang L, You H. Uniform $YVO_4$: $Ln^{3+}$ (Ln= Eu, Dy, and Sm) nanocrystals: solvothermal synthesis and luminescence properties. Optical materials 2009;31:1032-7.

[176] Phaomei G, Singh WR, Ningthoujam RS. Solvent effect in monoclinic to hexagonal phase transformation in $LaPO_4$: RE (RE= $Dy^{3+}$, $Sm^{3+}$) nanoparticles: photoluminescence study. Journal of Luminescence 2011;131:1164-71.

[177] Báez-Rodríguez A, Albarrán-Arreguín D, García-Velasco AC, Álvarez-Fregoso O, García-Hipólito M, Álvarez-Pérez MA, et al. White and yellow light emission from $ZrO_2$: Dy 3+ nanocrystals synthesized by a facile chemical technique. Journal of Materials Science: Materials in Electronics 2018;29:15502-11.

[178] Martínez-Martínez R, Lira AC, Speghini A, Falcony C, Caldiño U. Blue-yellow photoluminescence from $Ce^{3+} \rightarrow Dy^{3+}$ energy transfer in $HfO_2$:$Ce^{3+}$: $Dy^{3+}$ films deposited by ultrasonic spray pyrolysis. Journal of Alloys and Compounds 2011;509:3160-5.

[179] Zhou H, Wang Q, Jin Y. Temperature dependence of energy transfer in tunable white light-emitting phosphor $BaY_2Si_3O_{10}$: $Bi^{3+}$, $Eu^{3+}$ for near UV LEDs. Journal of Materials Chemistry C 2015;3:11151-62.

[180] Blasse G. Energy transfer in oxidic phosphors. Physics Letters A 1968;28:444-5.

[181] Thomas GL. The physics of fingerprints and their detection. Journal of Physics E: Scientific Instruments 1978;11:722.

[182] Saif M, Shebl M, Nabeel AI, Shokry R, Hafez H, Mbarek A, et al. Novel non-toxic and red luminescent sensor based on $Eu^{3+}$: $Y_2Ti_2O_7/SiO_2$ nano-powder for latent fingerprint detection. Sensors and Actuators B: Chemical 2015;220:162-70.

[183] Seah LK, Dinish US, Phang WF, Chao ZX, Murukeshan VM. Fluorescence optimisation and lifetime studies of fingerprints treated with magnetic powders. Forensic science international 2005;152:249-57.

[184] Li Z, Wang Q, Wang Y, Ma Q, Wang J, Li Z, et al. Background-free latent fingerprint imaging based on nanocrystals with long-lived luminescence and pH-guided recognition. Nano Research 2018;11:6167-76.

[185] Wilshire B. Advances in fingerprint detection. Endeavour 1996;20:12-5.

[186] Sodhi GS, Kaur J. Powder method for detecting latent fingerprints: a review. Forensic science international 2001;120:172-6.

[187] Zhang D, Liu F, Zhao Q, Lu G, Luo N. Selecting a reference high resolution for fingerprint recognition using minutiae and pores. IEEE Transactions on Instrumentation and Measurement 2011;60:863-71.

[188] Li Y, Xu C, Shu C, Hou X, Wu P. Simultaneous extraction of level 2 and level 3 characteristics from latent fingerprints imaged with quantum dots for improved fingerprint analysis. Chinese Chemical Letters 2017;28:1961-4.

[189] Kumar S, Rai S, Rath C. Monoclinic to cubic phase transformation and photoluminescence properties in $Hf_{1-x}Sm_xO_2$ (x= 0–0.12) nanoparticles. Journal of Applied Physics 2018;123:055108.

[190] Kumar S, Rai S, Rath C. Multifunctional role of dysprosium in $HfO_2$: stabilization of the high temperature cubic phase, and magnetic and photoluminescence properties. Physical Chemistry Chemical Physics 2017;19:18957-67.

[191] Long B, Li Y, Mandal S, Jha R, Leedy K. Switching dynamics and charge transport studies of resistive random access memory devices. Applied Physics Letters 2012;101:113503.

[192] Yu S, Guan X, Wong H-SP. Conduction mechanism of $TiN/HfO_x/Pt$ resistive switching memory: A trap-assisted-tunneling model. Applied Physics Letters 2011;99:063507.

[193] Soo Lee M, Choi S, An C-H, Kim H. Resistive switching characteristics of solution-deposited Gd, Dy, and Ce-doped $ZrO_2$ films. Applied Physics Letters 2012;100:143504.

[194] Cao X, Li X, Gao X, Yu W, Liu X, Zhang Y, et al. Forming-free colossal resistive switching effect in rare-earth-oxide $Gd_2O_3$ films for memristor applications. Journal of Applied Physics 2009;106:073723.

[195] Hua P, Ning D. A Forming-Free Bipolar Resistive Switching in $HfO_x$-Based Memory with a Thin Ti Cap. Chinese Physics Letters 2014;31:107303.

# *List of Publications*

1) **Sandeep Kumar**, S. B. Rai, and C. Rath, Multifunctional role of dysprosium in $HfO_2$: stabilization of the high temperature cubic phase, and magnetic and photoluminescence properties., ***Physical Chemistry Chemical Physics***, *19*(29), **2017**, 18957-18967.

2) **Sandeep Kumar**, S. B. Rai, and C. Rath, Monoclinic to cubic phase transformation and photoluminescence properties in $Hf_{1-x}Sm_xO_2$ (x=0–0.12) nanoparticles., ***Journal of Applied Physics,*** *123(5)*, **2018**, 055108.

3) **Sandeep Kumar**, S. B. Rai, and C. Rath, Latent Fingerprint Imaging Using Dy and Sm Codoped $HfO_2$ Nanophosphors: Structure and Luminescence Properties., ***Particle & Particle Systems Characterization***, **2019**, 1900048.

4) **Sandeep Kumar** and C. Rath, Oxygen vacancy mediated stabilization of cubic phase at room temperature and resistive switching effect in Sm and Dy doped $HfO_2$ thin film, **(Under Review), 2019.**

5) **Sandeep Kumar** and C. Rath., Structural and Photoluminescence Properties of Sm and Dy Codoped $HfO_2$ Nanoparticles, **(Under Review), 2019.**

6) Priyanka Tiwari, **Sandeep Kumar** and C. Rath, Structural and magnetic phase transitions along with optical properties in $GdMn_{1-x}Fe_xO_3$ Perovskite, ***Journal of Applied Physics,*** *126(4)*, **2019,** 045102**,.**